Characterization and hydrocarbon potential of the Lower Permian Wolfcamp Formation, northwestern Mitchell County, Midland Basin, Texas

by

Zachary Andrew Calhoun

A thesis submitted to the Graduate Faculty of
Auburn University
in partial fulfillment of the
requirements for the degree of
Master of Science

Auburn, Alabama
December 15, 2018

Keywords: gravity flow lithofacies, hydrocarbon potential, Wolfcamp Formation, Midland Basin

Approved by

Ashraf Uddin, Chair, Professor of Geology
Charles Savrda, Professor of Geology
Herbert Martin, Devon Energy

Abstract

Lithologic, petrologic, and geochemical analyses were performed on the Wolfcamp Formation (operational benches A and B), with a focus on a 400-ft-thick core recovered from wildcat well Strain 2V (API 42-335-53586) in northwestern Mitchell County, Texas. The core along with thin sections, mineralogical, and petrophysical data was made available by Devon Energy. Observations were supplemented with structural contour and isopach maps of the Wolfcamp A and B tops. The goals of the study were to (1) characterize the lithofacies in the Wolfcamp Formation, (2) interpret the environments and depositional conditions and processes that influenced deposition of the Wolfcamp Formation, and (3) assess the hydrocarbon-source rock potential and unconventional hydrocarbon-reservoir rock potential of Wolfcamp Formation lithofacies.

Seven lithofacies are recognized in the Lower Permian section of the Strain core based on primarily on sedimentary features and mineralogy determined by x-ray diffraction. The facies are complexly interbedded and include (1) sandstones, (2) siltstones, (3) siliceous mudstones (4) calcareous siltstones, (5) calcareous mudstones, (6) calcarenites, and (7) bioclast-lithoclast wackestone-floatstones. These lithofacies were deposited by a combination of sediment gravity flow and pelagic processes. Sediment gravity flows recorded in the Strain core are turbidity currents, hyperpycnal flows, debris flows, and transitional flows. The transitional flows, while thin-bedded and limited to the uppermost core intervals, record transitions of gravity flows from

carbonate-dominated turbulent flows to mud-rich cohesive laminar flows. The vertical distribution of lithofacies was used to divide the Strain core into seven distinct lithofacies associations, each representing a distinct depositional environment and sea-level condition. The lithofacies associations, in ascending order, are: 1) interbedded sandstone and siltstone lithofacies association (LA-A), 2) mudstone with calcarenite, and bioclast-lithoclast wackestone-floatstone lithofacies association (LA-B), 3) calcarenites, bioclast-lithoclast wackestones-floatstone, and mudstone lithofacies association (LA-C), 4) calcarenite and calcareous siltstone with interbedded calcareous mudstone lithofacies association (LA-D), 5) siliceous mudstone lithofacies association (LA-E), 6) massive calcarenite and rare mudstone lithofacies association (LA-F), and 7) mudstone, thin calcarenite and bioclast-lithoclast wackestones-floatstone lithofacies association (LA-G).

Organic geochemical data from Rock-eval analyses indicate that the Wolfcamp Formation contains sufficient quantities of mature, mixed Type II and Type III organic matter to serve as a good to excellent hydrocarbon-source rock in the Mitchell County area. Industry-provided petrophysical and XRD data suggests clay-rich and siliceous facies are the highest quality hydrocarbon-source rocks and unconventional hydrocarbon-reservoir rocks, with carbonate facies being negatively associated with organic richness and reservoir quality.

Geochemical analyses of the Wolfcamp Formation lithofacies were performed using 14 geochemical proxies for sedimentation, redox state, and paleo-productivity. Results suggest the development of anoxic conditions during sea-level transgressions and highstands.

Acknowledgments

First, I want to thank my wonderful Fiancée, Alexandra, for all of her love and support during this process. She was with me every step of the way and I could not have imagined finishing this research without her. I would also like to thank my advisor and friend, Dr. Ashraf Uddin. He pushed me in ways I never knew I could be pushed and the result is that I have produced something I never knew I could. I also thank Herbert and Marynm Martin for all of their hospitality and wisdom. I cannot thank them and their family enough for their support throughout this journey. Thanks go to Devon Energy for providing access to their cores and core facility. To Erik Kvale, thank you for your time, patience, and incredible insight into this area of research. My only wish is that we could have met more often. Thank you to the amazing staff of the department (Mrs. Sheila, Ms. Delaine, Mrs. Audrey, and Tony) for helping this mere graduate student navigate his way through academia. I definitely could not have done this without their help and patience. I also give a great deal of thanks to all of those involved in the funding of this research.

Table of Contents

List of Tables

List of Figures

List of Abbreviations

Al	Aluminum
API	American Petroleum Institute
BCFG	Billion cubic feet of associated gas
C	Carbon
CBP	Central Basin Platform
Co	Cobalt
Cr	Chromium
Cu	Copper
EF	Enrichment factor
Fe	Iron
GR	Gamma Ray
H_2S	Hydrogen Sulfide
HCL	Hydrochloric acid
Kg	Kilogram
LPIA	Late Paleozoic Ice Age
MMBNGL	Million barrels of natural gas liquids
MMBO	Million barrels of oil
Mn	Manganese
Mo	Molybdenum

MoO^{2-}_4	Molybdate Oxyanion
NASC	North Amercian Stratigraphic Code
nd	Nanodarcy
ISC	International Stratigraphic Code
Ni	Nickel
OM	Organic matter
OPIC	Oklahoma Petroleum Information Center
P	Phosphorus
RSTE	Redox-sensitive trace element
S	Sulfur
SGF	Sediment gravity flow
Si	Silicon
Ta	Bouma “A” division of a turbidite sequence
Tb	Bouma “B” disivion of a turbidite sequence
Th	Thorium
Ti	Titanium
Tmax	Temperature of maximum rate of hydrocarbon generation
TOC	Total organic carbon
U	Uranium
U_{total}	Total Uranium
USGS	United States Geological Survey

V	Vanadium
XRD	X-ray diffraction
XRF	X-ray fluorescence
Zn	Zinc
µmol	Micromol

CHAPTER 1: INTRODUCTION

Since the early 1960s, when Arnold H. Bouma published his papers on the now famous turbidite sequence, many studies have sought to characterize and understand deep water sediment gravity flow processes (SGFs). As vectors for transporting large volumes of coarse-grained material into low-energy marine settings, the significance of SGFs in geologic settings across the globe have become increasingly appreciated in modern sedimentological studies. Along with information regarding depositional environments and regional tectonics, SGFs are also being extensively studied to evaluate their hydrocarbon-resource potential (Bouma et al., 1962, Haughton et al., 2009; Kvale et al., 2017). In the Permian Basin of the southwestern United States, one of the most significant petroleum-producing regions in the world, deep marine deposits and environments are being studied at the facies-scale to better understand the relationship between SGFs, depositional environment, paleoceanographic conditions, and hydrocarbon-resource potential. Of particular interest is the late Paleozoic Wolfcamp Formation of the Midland Basin, the eastern sub-basin of the Permian Basin.

The Wolfcamp Formation is an Upper Pennsylvanian-Lower Permian sedimentary unit composed of interlayered siliciclastics and carbonates interpreted to have been deposited in deep marine and shelf settings. The Wolfcamp Formation is an important hydrocarbon resource within the Permian Basin. The U.S. Geological Survey recently assessed the Wolfcamp Formation of the Midland Basin to determine undiscovered, technically recoverable petroleum resources in the highly productive Permian Basin. This evaluation determined that mean resources for the Wolfcamp Formation total 20 billion barrels of oil, with an F95–F5 range from 11.4 to 31.5 billion barrels; 16 trillion cubic feet of associated gas, with an F95–F5 range from 7.9 to 27 trillion cubic feet; and nearly 1.6 billion barrels of natural gas liquids with an F95– F5 range

from .7 to 2.9 billion barrels (Gaswirth et al., 2016). These quantities of hydrocarbons make the Wolfcamp the largest continuous oil play in the United States, nearly three times larger than that reported in the 2013 USGS Bakken-Three Forks resource assessment, and an enticing target for petroleum companies in the Permian Basin.

Conventional hydrocarbon resource plays are defined as reservoirs that have a well-defined areal extent and can produce resources at economic flow rates without extensive stimulation procedures or special recovery methods (Vidas and Hughman, 2008; Cortez III, 2012). These hydrocarbon reservoirs can typically be exploited with simple vertical drilling strategies and contain permeable rocks. Along with permeable reservoir rock, a conventional reservoir will contain a source rock, hydrocarbon trap, and an impermeable caprock (Selley and Sonnenberg, 2015). For well over a century, conventional reservoirs have been the primary sources of petroleum production globally.

Newly-exploited continuous reservoirs, termed unconventional reservoirs, are much more challenging to define. The United States government defines unconventional reservoirs as systems with a permeability to gas flow of less than 0.1 millidarcy (Cortez III, 2012). However, based on integrations of Darcy's Law in the petroleum industry, a more appropriate definition for unconventional reservoirs are diverse systems that can only be produced economically after large-stimulation operations and enhanced recovery methods are performed (Vidas and Hughman, 2008; Cortez III, 2012). Common unconventional systems include gas shale, tight-gas sand, coal-bed methane, and heavy oil. Some of the processes used to stimulate production from unconventional reservoirs include hydraulic fracturing, flooding, and steam injection. These stimulation procedures allow for impermeable seal and source rocks to be targeted and produced

as primary reservoirs. Unconventional reservoirs in the Permian Basin represent a significant contribution of U.S. oil production (Cortez III, 2012; Selley and Sonnenberg, 2015).

The first commercial well in the Permian Basin was the Santa Rita No. 1, which was located in Mitchell County, Texas and completed in the early 1920s. The well continued to produce until 1990 when it was finally capped. Since then, hydrocarbon research, exploration, and production within the Permian Basin has increased substantially, and there has been an exponential increase in horizontal wells drilled in the Midland Basin since 2010 (Sutton, 2015). Much of this increase is due to the development of new unconventional resource plays in basinal deposits throughout the basin. Thousands of feet of potentially productive mudrock has stimulated significant interest due to the potential for multiple drilling targets and stacked horizontal wells within a single drill-site. Over the past few years, favorable economic conditions and improved technology has stimulated interest in evaluating the reservoir potential of resedimented carbonates and mudstones of ancient submarine shelf and fan systems in the Permian Basin.

The observation of the depositional elements of submarine shelf and fan systems and their lateral and vertical relationships allows for an understanding of these terminal depositional systems. Traditionally, this understanding has revolved around studies of deep-water turbidite complexes and models of their deposition. However, Posamentier and Walker (2006) asserted that no single facies model is capable of incorporating the complexity of large-scale submarine depositional systems. Following decades of study, it is now understood that deposition on the shelf, slope, and basin floor is primarily controlled by the interplay of tectonism, relative sea level, and the characteristics of the shelf-edge and upper slope. These shelf and slope characteristics include grain-size distribution, and frequency and magnitude of flow events

(Posamentier and Walker, 2006). Additionally, recent studies of subaqueous fan and shelf settings have recognized sediment gravity flow processes as mechanisms for depositing terrigenous material, such as plant debris, in deep marine settings. These observations indicate that a significant contribution of organic matter in deep marine hydrocarbon reserves may have been contributed from terrigenous sources by fluvially-influenced gravity flow processes (Plink-Björklund and Steele, 2004).

To date, there has been an extensive body of literature developed regarding the deposition of the Wolfcamp Formation in the center of the Midland Basin. However, there has been little attention given to the Wolfcamp Formation proximal to the basin margins. The primary objectives of this study are to study a single drill core recovered from northwestern Mitchell County, Texas in order to (1) characterize, in detail, the lithofacies of the Wolfcamp Formation in the eastern Midland Basin, (2) interpret the environmental conditions and processes that influenced deposition, and (3) assess the hydrocarbon potential of these mixed carbonate-siliciclastic lithofacies.

CHAPTER 2: GEOLOGIC SETTING

2.1 The Permian Basin

Located in western Texas and southeast New Mexico, the Permian Basin is a foreland basin rimmed by carbonate platforms and bisected by an intervening high known as the Central Basin Platform (CBP). The Permian Basin is bounded by the Diablo Platform and Pedernal Uplift to the west, the Matador Arch to the north, the Marathon-Ouachita Thrust Belt to the south, and the Eastern Shelf to the east (Fig. 1) (Ball, 1995). The Permian Basin is made up of many smaller sub-basins and uplifts that are related to tectonic activity associated with the assembly of the Pangean supercontinent (Hills, 1985). During much of the Paleozoic, the region was a passive margin characterized by a stable carbonate platform. Later internal subsidence resulted in the formation of a continental sag known as the Tobosa Basin (Frenzel et al., 1988). By the Late Mississippian to Early Pennsylvanian, movement along the Marathon-Ouachita Orogenic Belt led to the regional transition from a passive margin to an active margin characterized by a foreland basin. This movement also resulted in a series of block rotations and uplifts. The rotation of two blocks during the late Pennsylvanian and the Early Permian resulted in the uplift of the CBP.

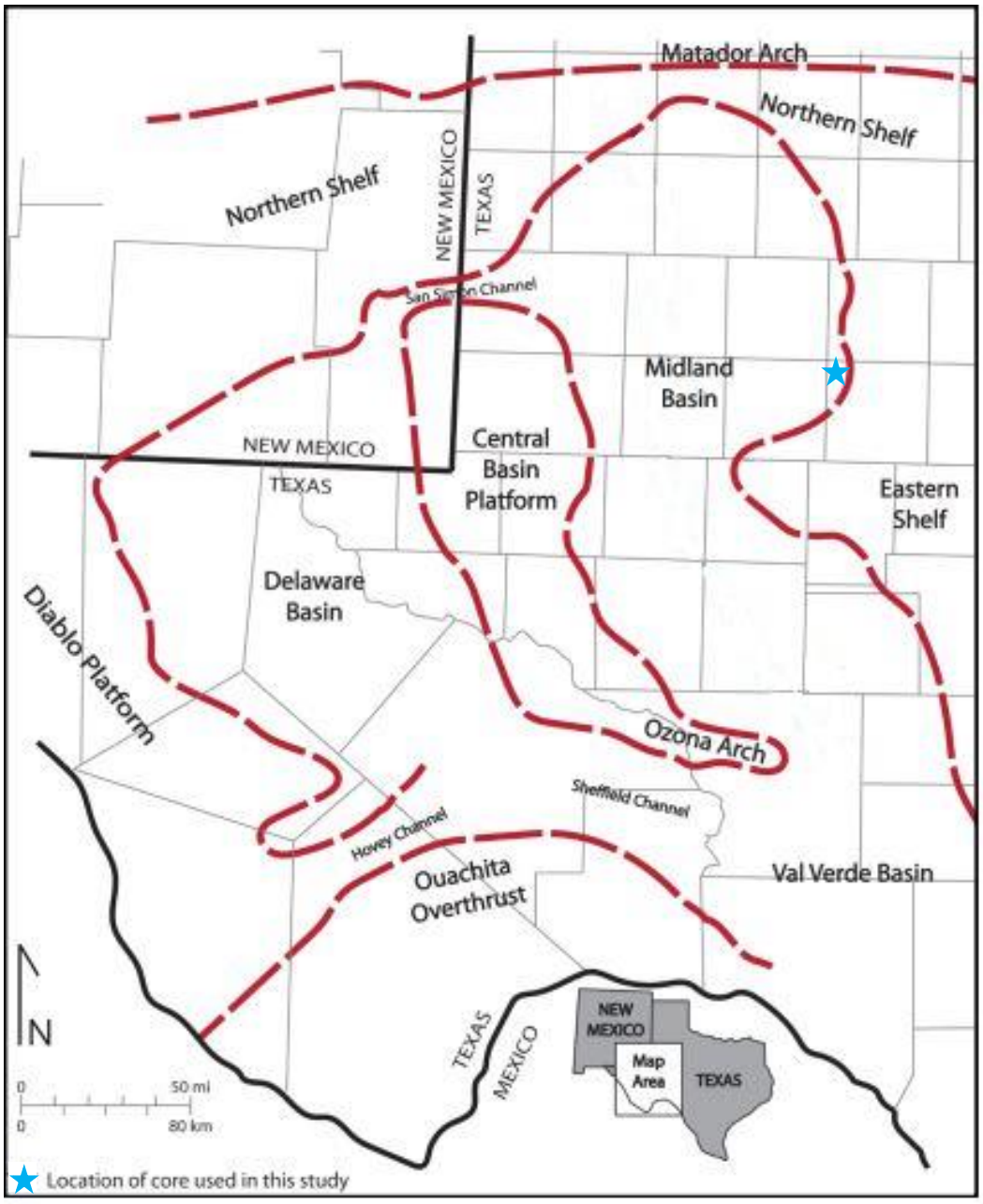

Figure 1: Map of the Permian Basin and associated structural features. The blue star indicates the location of the studied core, Strain 2V (modified from Silver and Todd, 1969).

The uplift of the CBP resulted in the formation of the two largest sub-basins that make up the greater Permian Basin; the Delaware Basin to the west of the CBP and the Midland Basin to the east (Yang and Dorobek, 1995). These sub-basins are different in that the Midland Basin is notably shallower than the Delaware Basin (Fig. 2C). These sub-basins contain formations of interbedded clastics and carbonates that were deposited during the late Paleozoic. From the Pennsylvanian (Strawn, Canyon, and Cisco) into the Early Permian (Wolfcampian and Leonardian), carbonates were deposited on the Northwestern and Eastern Shelves of the Midland Basin, as well as on the Central Basin Platform, whereas fine-grained siliciclastics were deposited in the center of the basin (Miall, 2008; Hamlin and Baumgardner, 2012). Deposition during this time was not likely influenced by movement along the Marathon-Ouachita Orogenic Belt but rather by the deformation and rapid subsidence that continued to influence the sub-basins through the Wolfcampian stage of the Early Permian (Bostwick, 1962). By the later Permian, deposition in the basins transitioned to redbed sandstones and evaporites (Ward et al., 1986). During the Triassic, the region became a closed continental basin in which a relatively thin layer of fluvial and lacustrine sediments was deposited over the thick (~3000 m) Paleozoic sequences.

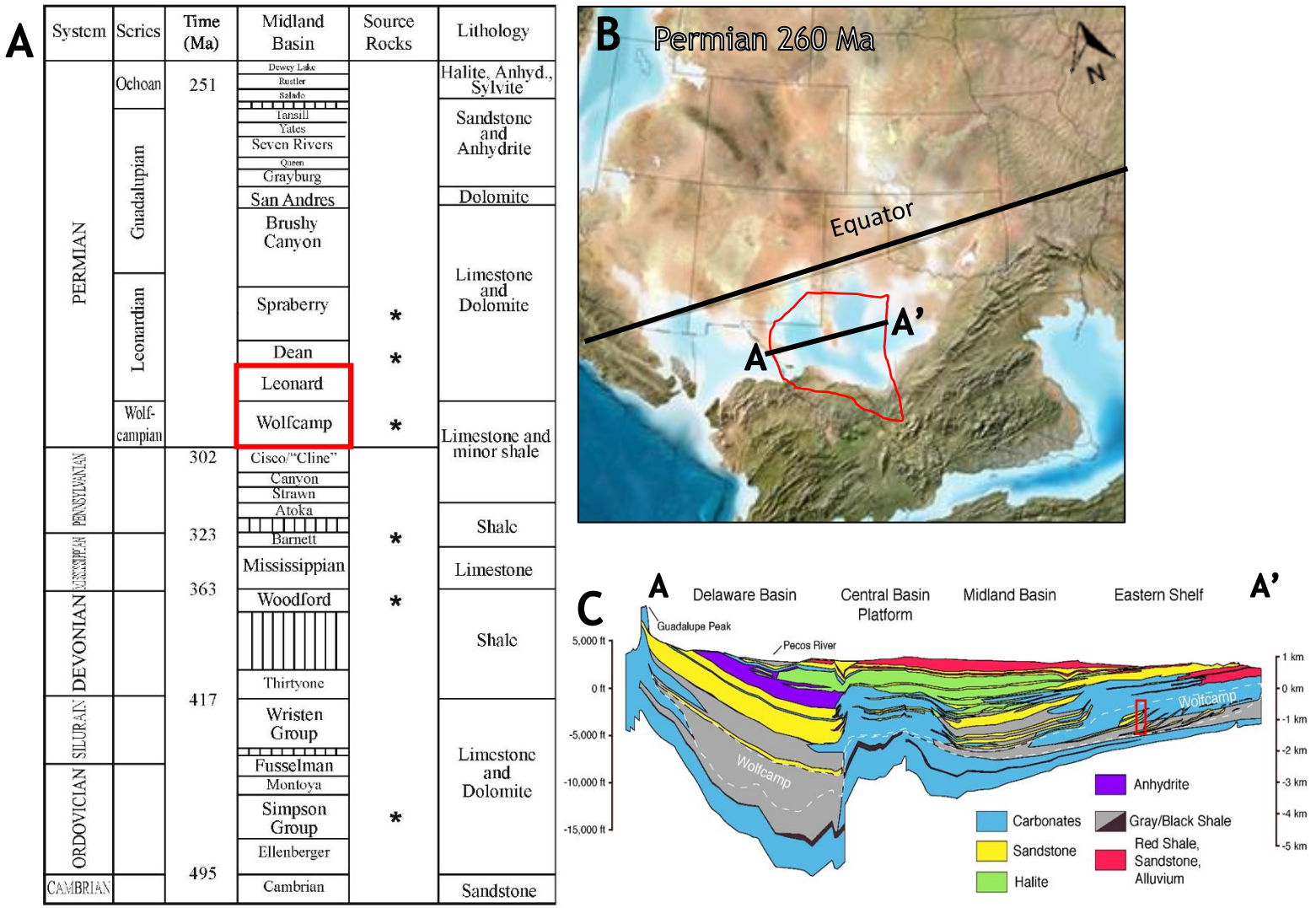

Figure 2: (A) Stratigraphic column of the Midland sub-basin (modified from Engle, 2016). The stratigraphic interval analyzed in this study is indicated by the red box. (B) Paleogeographic map of the Midland Basin, Texas (from Blakey, 2011). (C) Generalized cross section of the Permian Basin along A-A' of 2B (from Engle, 2016).

The northern Midland Basin is dominated by the Horseshoe Atoll, an arcuate subsurface Pennsylvanian limestone accumulation composed of phylloidal algae, crinoids, and other non-framework communities. The eastern boundary of the Permian Basin is the Eastern Shelf, which has been characterized as a mixed carbonate and siliciclastic system. Along the Eastern Shelf are the limestones of the Clear Fork and Wichita platform (also known as the Wolfcamp platform). This platform has been identified as the source of the carbonate SGFs deposited within the deep marine settings of the Midland Basin. Prograding out towards the center is the Glasscock Nose, a limestone accumulation developed by the westward progradation of reef build-ups from the Eastern Shelf out into the Midland Basin (Fig. 1; Flamm, 2008). Notably, reefs during the Permian developed as reef mounds due to the lack of reef-building framework organisms such as corals and stromatoporoids. Instead the biota of the Lower Permian included tubiphytes, phylloidal aglae, encrusting foraminifera, bryozoans, and calcisponges that built their structures within the sub-wavebase of the upper slope. The positive relief of these communities and mound build-ups allowed the accumulation of packstone and grainstone shoals landward (Wahlman and Tasker, 2013).

The climate of the Lower Permian has been characterized as an icehouse period due to the expansion and contraction of widespread continental glaciers in southern Gondwana (Baumgardner et al., 2016). This icehouse climate was a product of the Late Paleozoic Ice Age (LPIA) (Gastaldo et al., 1996; Fielding et al., 2008). The extent of continental ice sheets are inferred to have been at maxima during the Pennsylvanian-Permian transition (early Wolfcampian). The waxing and waning of ice sheets greatly influenced sea-levels, causing high-frequency and high-amplitude fluctuations in eustasy. Within the Midland Basin, sea-level is estimated to have fallen by 1000-2000 ft (330-660 m) in order to generate the regional

"Wolfcamp Shale Marker" unconformity (Mazzullo and Reid, 1989; Flamm, 2008; Baumgardner et al., 2016). Sea-level lowstand conditions prevailed throughout the early Wolfcampian before shifting to the progressively higher highstand conditions characteristic of the later Wolfcampian and early Leonardian (Fig. 3; Baumgardner et al., 2016).

Additionally, western Pangea became increasingly arid as icehouse conditions waned during the late Paleozoic. The climate of the region was characterized as subhumid in the latest Pennsylvanian, later transitioning to a semiarid climate during the Wolfcampian and a fully arid climate in the Leonardian (Baumgardner et al., 2016). Other influences on the late Paleozoic climate include tectonic drift and a long-term drying trend that began during the Middle Pennsylvanian (Baumgardner et al., 2016).

2.2 Wolfcamp Formation

The Wolfcamp Formation was first defined by Udden et al. (1916) based on a 700-ft-thick section in the Glass Mountains that is dominated by shale and limestone but also includes subordinate sandstone and conglomerate. The formation was named after Wolf Camp at the type locality of the formation located 12 miles north of Marathon, Texas. The Wolfcamp Formation has since been accepted as the lowermost Permian formation of the Glass Mountains and the surrounding area.

For the Lower Permian of the Midland Basin, the North American Stratigraphic Code (NASC) uses the terms "Wolfcamp" and "Leonard" and "Wolfcampian" and "Leonardian" for the formation and stage names, respectively. The International Stratigraphic Code (ISC) nomenclature for lower Permian rocks includes, in ascending order, the Asselian, Sakmarian, Artinskian, and Kungurian. Upper Pennsylvanian rock nomenclature based on the ISC includes,

in ascending order, the Kasimovian and Gzhelian. For this study NASC terminology will be used in order to correlate findings to previous studies and for consistency.

As shown in figure 4, the Wolfcamp Formation is commonly divided into several benchs (Wolfcamp A, B, C, and D) by the oil and gas industry. Wolfcamp A is known as the Leonard. Wolfcamp B and C are known as the Wolfcamp. Wolfcamp D is known as the Cline Shale.

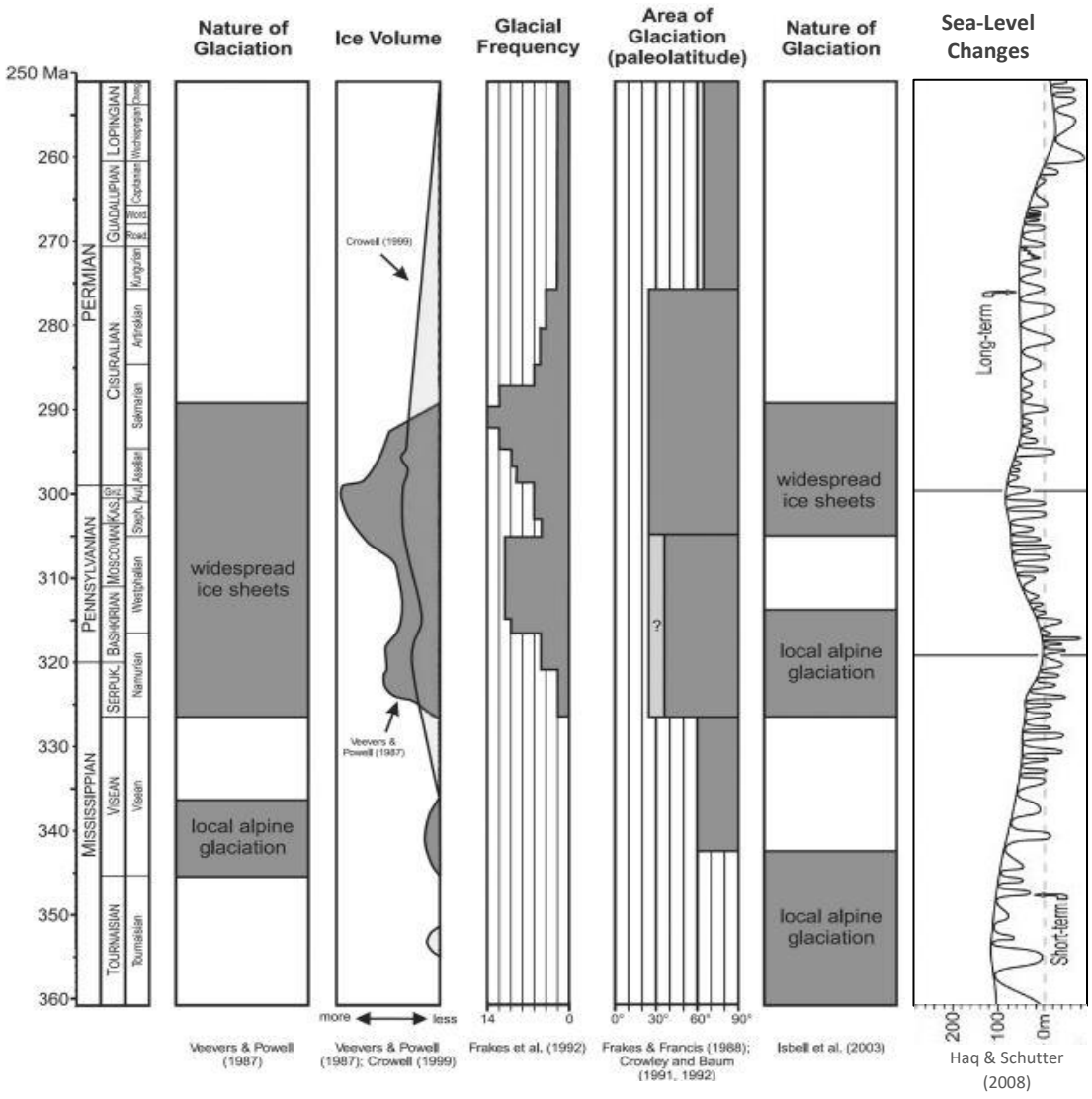

Figure 3: Stratigraphic column depicting the Late Paleozoic Ice Age glaciation and sea-level fluctuations from Haq and Schutter (2008) throughout the Carboniferous and Permian (modified from Fielding et al., 2008).

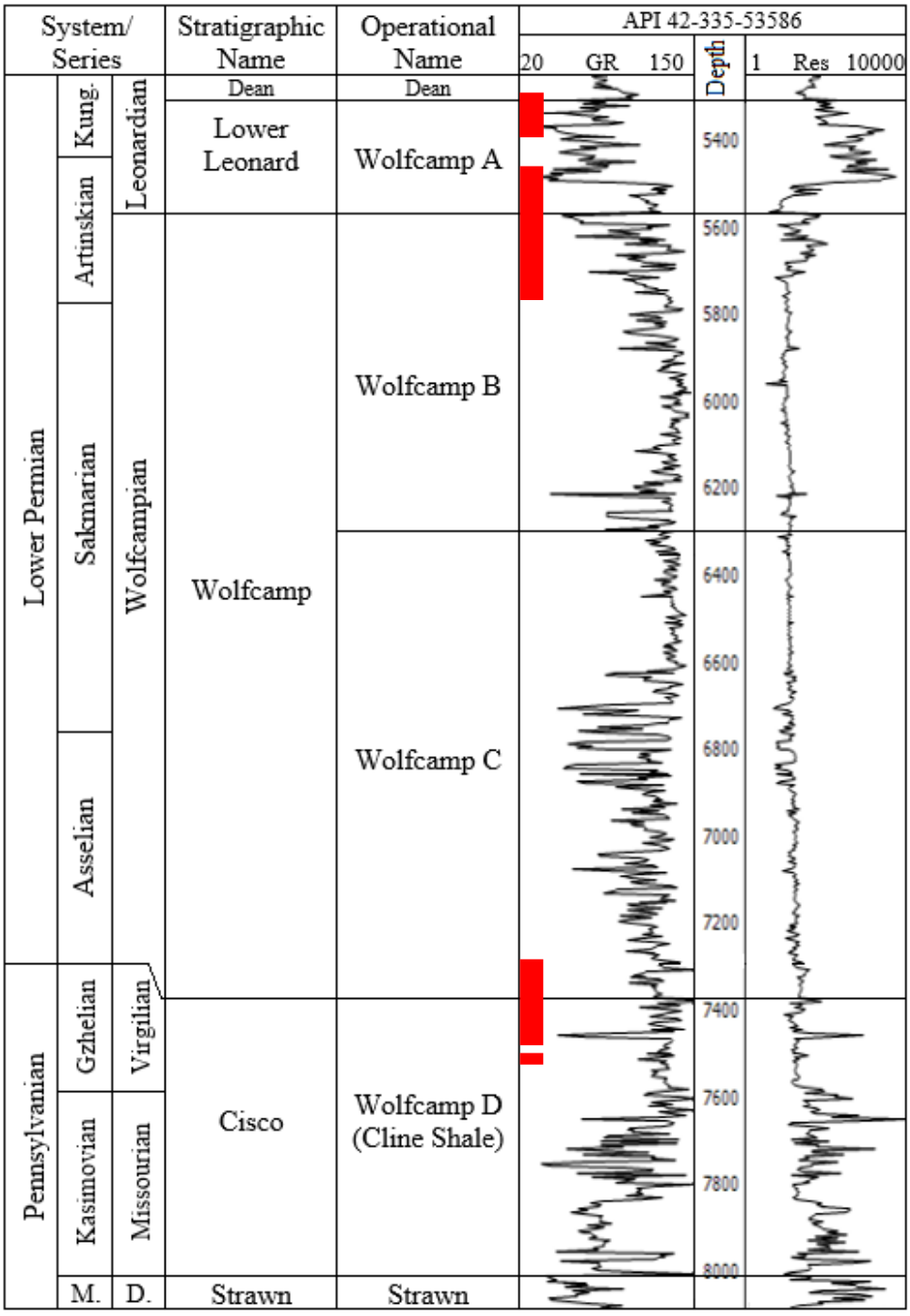

Figure 4: Stratigraphic column for the late Paleozoic of the Midland Basin with formation tops correlated to the Strain 2V well log**.** Stratigraphy from Baumgardner et al. (2016). The red rectangles indicate intervals where drill core was recovered. Only the Wolfcamp A and B sections were analyzed in this study. M. = Moscovian. D. = Desmoinesian

CHAPTER 3: STUDY LOCATION AND METHODS

3.1 Strain 2V Core Location and Stratigraphy

The drill core used in this study was recovered from a wildcat well in northwestern Mitchell County (Fig. 5). The name of the well the core was recovered from is Strain 2V and, therefore, the core section will be referred to as the Strain core throughout this study. The Strain core is a 3”-diameter core that was slabbed and polished by Weatherford Laboratories and made available for viewing by Devon Energy. The core is currently housed in the Oklahoma Petroleum Information Center, in Norman, Oklahoma. The total length of the core is ~750 ft. However, the core is discontinuous, being comprised of four distinct segments. The stratigraphic intervals contained in the core segments are, in ascending order, the upper part of Wolfcamp D (7589 to 7599 ft and 7312 to 7529 ft), the upper part of Wolfcamp B (5501 to 5766.5 ft) to the lower part of the Wolfcamp A (5465 to 5501 ft), and the upper part of the Wolfcamp A (5312 to 5400 ft) to the lower part of the Dean Sandstone (5280 to 5312 ft). Only data for the Wolfcamp A and B sections of the core (a ~ 400 ft interval in total) are discussed in this study (see Fig. 4).

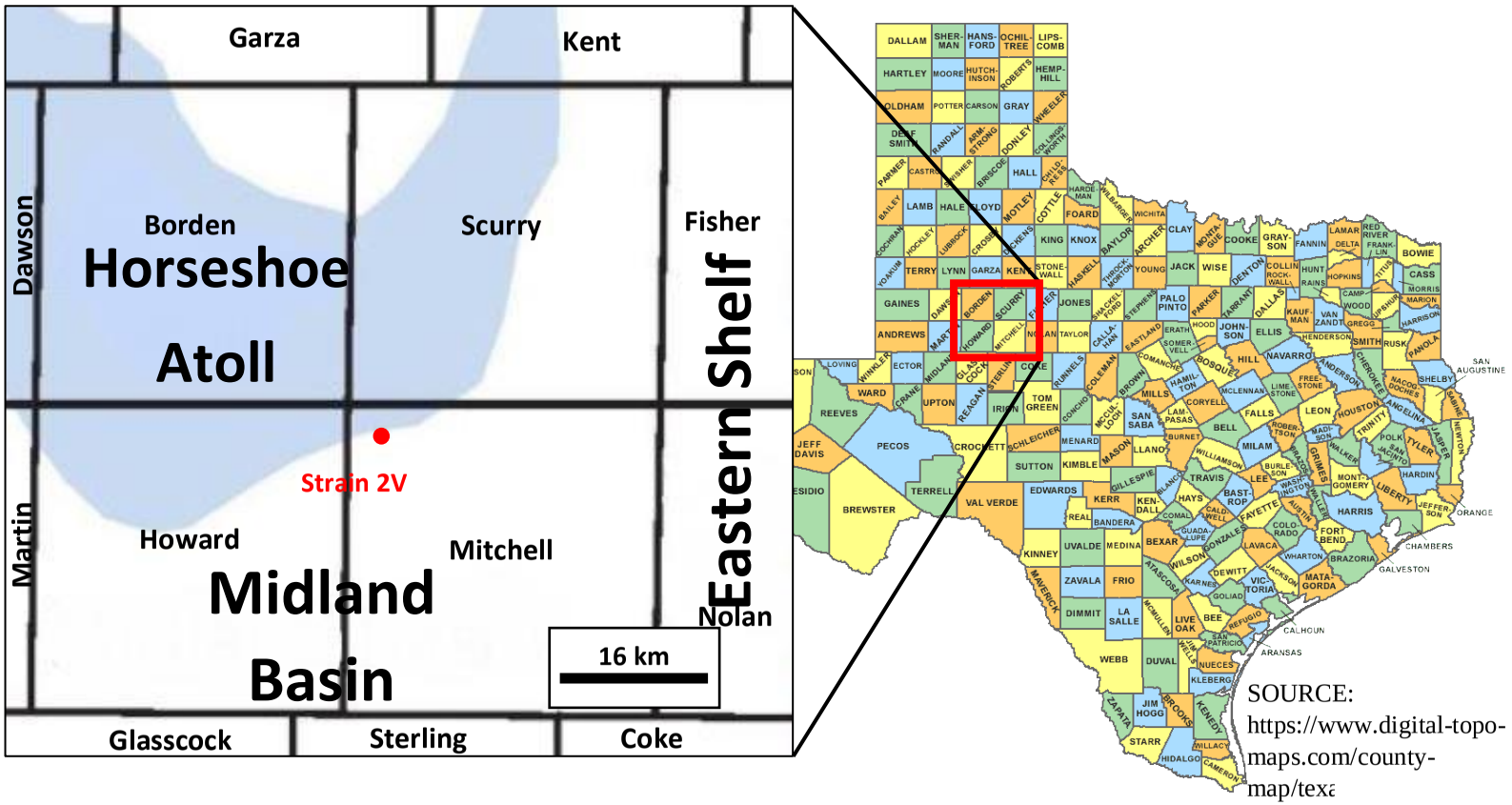

Figure 5: Geographic location of the Strain 2V well (red dot) in the Midland Basin. The Horse Atoll is colored blue (modified from Roush, 2015).

3.2 Analytical and Sampling Methods

The Strain 2V core boxes were laid out in ascending order in the OPIC facility. The core was then photographed and examined using the naked eye, handlens, and binocular microscope. Descriptions and photographic records were made of lithology, sedimentary structures, bedding, and textures based on the observation of polished slabbed core faces. Attention also was paid to bedding-parallel parting surfaces.

Following core description, the Strain 2V was systematically sampled for rock-eval and geochemical analyses (Fig. 6). Eighty-four (84) chunk/chip samples were taken at roughly 5-ft intervals through the total length of core in order to perform geochemical (total organic carbon and rock-eval pyrolysis) and elemental analyses (Fig. 6; x-ray fluorescence; XRF).

3.3 Thin Section Petrography

A total of forty-three (43) thin sections, produced commercially by Weatherford Labs from intervals in the Wolfcamp B section of the Strain core (Fig. 6) were provided by Devon Energy. Thin sections were analyzed under a petrographic microscope at various magnifications in order to characterize lithology and sedimentary structures. Digital photomicrographs were taken to record various features that aided in the characterization of lithofacies.

3.4 Inorganic Geochemistry

Of the eighty-four (84) samples collected from the Strain core, thirty-six (36) sufficiently voluminous samples were analyzed by XRF by Weatherford Laboratories in Houston, Texas (Fig. 6).

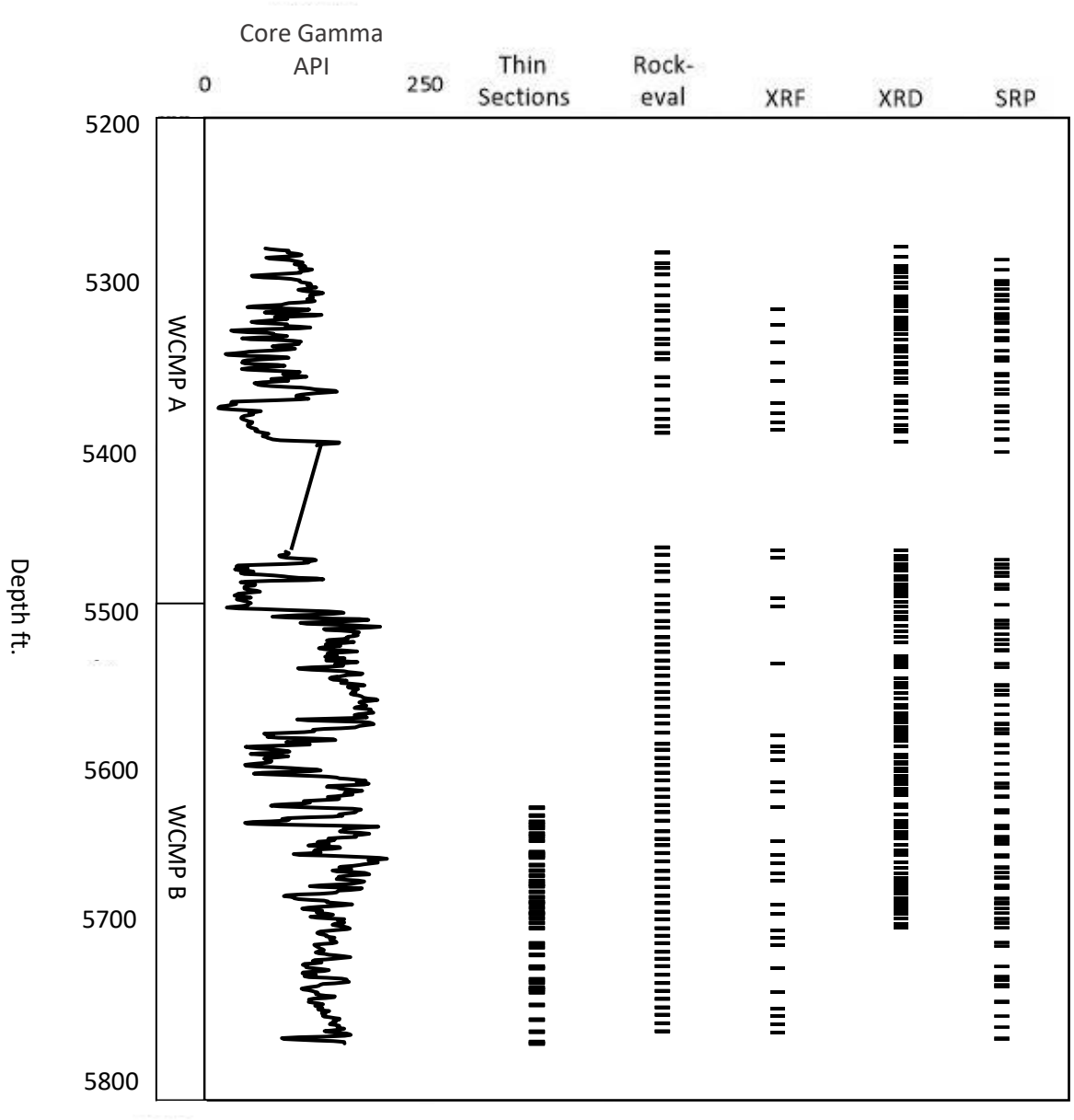

Figure 6: Diagram of the Strain core gamma with locations of samples used for thin sections, Rock-eval pyrolysis, XRF, XRD, and SRP indicated by black dashes.

3.5 Rock-Eval Pyrolysis

Eighty-one (81) of the eighty-four (84) collected samples had sufficient material to be analyzed by commercial source-rock analyses. These analyses included LECO carbon analysis and Rock-eval pyrolysis by Weatherford Laboratories in Houston, Texas (Fig. 6).

3.6 Rock Properties Dataset

Samples for x-ray diffraction (XRD) and shale rock properties (SRP, porosity and permeability) were collected at 1-to-9 ft sample intervals within the Wolfcamp A and B (Fig. 6). The analyses of the samples were conducted by Weatherford Laboratories and provided by Devon Energy for this study. Mineralogy determined by XRD was used to characterize lithofacies and their vertical distribution throughout the core.

CHAPTER 4: LITHOFACIES ANALYSIS

Observations of the Strain 2V core and thin section petrography have identified seven lithofacies (Figs 7). Along with core and thin section observations, mineralogy determined by XRD, TOC determined by Rock-eval, and permeability and porosity data were also used to characterize each lithofacies (Table 2). Interpretations of depositional processes are also discussed in this chapter. The identified facies are: 1) sandstone, 2) siltstone, 3) siliceous mudstone, 4) calcareous siltstone, 5) calcareous mudstone, 6) calcarenite, and 7) bioclast-lithoclast wackestone-floatstone.

The Strain core lithofacies reflect a variety of depositional processes typical of a slope-basin setting. These depositional processes have been identified and discussed in numerous studies (Montgomery, 1996; Mazzullo, 1997; Beall et al., 1998; Mazzullo, 1998; Stoudt; 1998). These primarily include episodic gravity flow processes, which are recorded in calciclastic and siliciclastic deposits (calcarenites, bioclast-lithoclast wackestones-floatstones, calcareous, and non-calcareous siltstones) as well as hemipelagic processes, indicated by the presence of clay-rich, calcareous and non-calcareous mudstone lithofacies (Fig. 7).

Gravity-driven subaqueous sediment flows are major marine sedimentary processes that transport sediments from shallow depths to deep marine environments. These processes can be initated by seismic activity or the accumulation of small scale slope failures. Common gravity-flow processes include debris flows, grain flows, turbidity currents, and transitional flows (Haughton et al., 2009; Talling et al., 2012). The sediment gravity flows within the Strain core were likely sourced from the adjacent carbonate platforms along the Eastern Shelf.

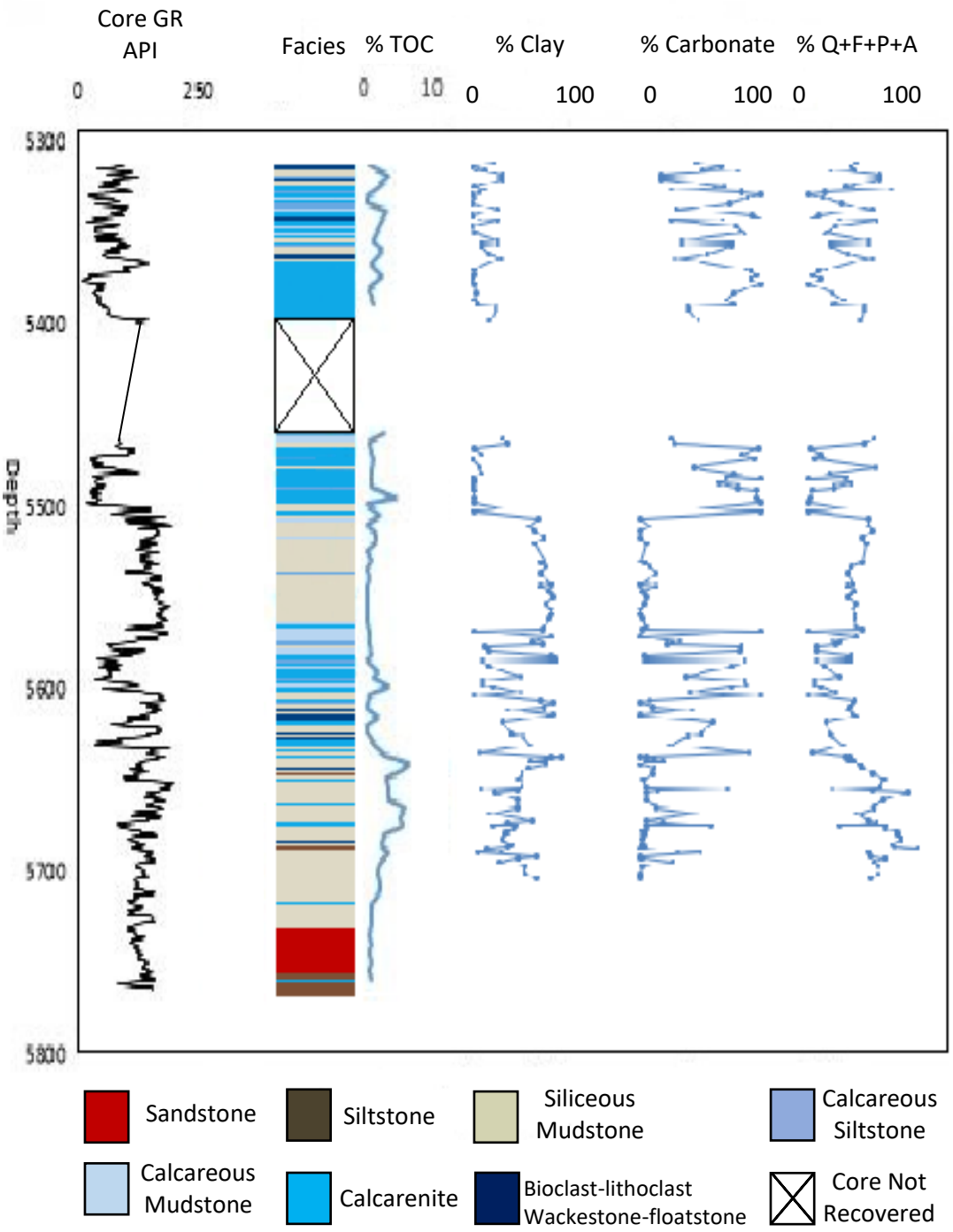

Figure 7: Core gamma, facies log, TOC, and XRD mineralogy of the Strain core.

Table 1: Summary of the identified lithofacies, mineralogy, and hydrocarbon resource potential.

Lithofacies	Sedimentary Features	Clay % Range (mean)	Carbonate % Range (Mean)	Q+F+P+A % Range (Mean)	Permeability nd Range (Mean)	Porosity % Range (Mean)	TOC % Range (Mean)
Sandstone	Horizontal laminations; burrows; distorted bedding	20.0 (NA)	28.0 (NA)	52.0 (NA)	726.0 (NA)	4.3 (NA)	0.8 (0.7-0.95)
Siltstone	Massive to laminated	35.9 (22.0-50.0)	5.2 (0-13.0)	58.9 (48.0-74.0)	681.7 (163.0-1020.0)	7.4 (4.4-10.0)	1.6 (0.4-3.5)
Siliceous Mudstone	Massive to weakly laminated; gradational to sharp upper and basal contacts; current ripple lamination	57.8 (45.0-68.0)	2.9 (0-13.0)	39.2 (31.0-48.0)	937.5 (701.0-1130.0)	9.7 (7.0-11.4)	2.1 (0.2-6.3)
Calcareous Siltstone	Massive to horizontally laminated; normal-inverse grading	21.5 (7.0-33.0)	28.1 (17.0-45.0)	50.4 (40.0-62.0)	543.8 (61.9-1110.0)	5.4 (2.0-7.6)	2.6 (1.4-4.6)
Calcareous Mudstone	Massive to weakly laminated	39.75 (38.0-42.0)	38.75 (31.0-49.0)	21.5 (19.0-24.0)	913.8 (791.0-1090.0)	6.0 (3.8-7.7)	1.5 (0.5-2.4)
Calcarenite	Massive with some laminated bedding	4.3 (1.0-16.0)	81.9 (54.0-95.0)	13.7 (3.0-36.0)	222.4 (6.6-1010.0)	2.5 (0.6-8.1)	0.04 (0.2-3.2)
Bioclast-lithoclast Wackestone-floatstone	Massive, distorted, with very poor sorting; carbonate and mudstone lithoclasts; matrix comprised of dark gray siliceous or calcareous mudstones	8.25 (1.0-13.0)	65.5 (51.0-74.0)	26.25 (14.0-38.0)	432.9 (43.6-1030.0)	3.6 (1.9-5.2)	2.2 (0.5-3.4)

4.1 Sandstone

The sandstone facies is characterized by medium to pale grey sandstones (Fig. 8). Sandstone bed thicknesses ranges from 2 cm to 6 cm. The average mineralogical composition for the sandstone facies is 20% clay minerals, 28% carbonate, and 52% quartz, feldspar, pyrite, and apatite (Q+F+P+A). Organic contents are low in this facies, averaging 0.8% (range = 0.7-0.95%). Sandstones are laminated to planar bedded with some bioturbation indicated (Fig. 8B). The lower contacts of this facies are generally gradational to sharp. Upper contacts are typically sharp.

The facies is composed of moderately sorted, fine to medium, subrounded to subangular quartz sand and detrital silt in a clayey matrix (Fig. 9). Pyrite occurs as fine grains or as larger masses dispersed in the sand (Fig. 9A-C). Siderite occurs locally as bands or as isolated nodules (Figs 8A and 9C). Permeability and porosity are 726 nd and 4.3%, respectively (Table 1).

Interpretation

The sandstone lithofacies, which only occurs in a single interval in the Wolfcamp B, is interpreted to represent deposition by fluvio-deltaic processes. The origin of sand in deep water deposits of the Delaware and Midland Basin has been explored in a number of studies (Fischer and Samthein, 1988; Kocurek and Kirkland, 1998; Hamlin and Baumgardner, 2012). These studies determined that coarse silt and sand were likely derived from contemporaneous eolian systems in the northeast and southeast (Hamlin and Baumgardner, 2012). While eolian processes likely transported siliciclastics into the Midland Basin during the deposition of the Wolfcamp Formation, the presence of a clay matrix precludes direct deposition by eolian processes.

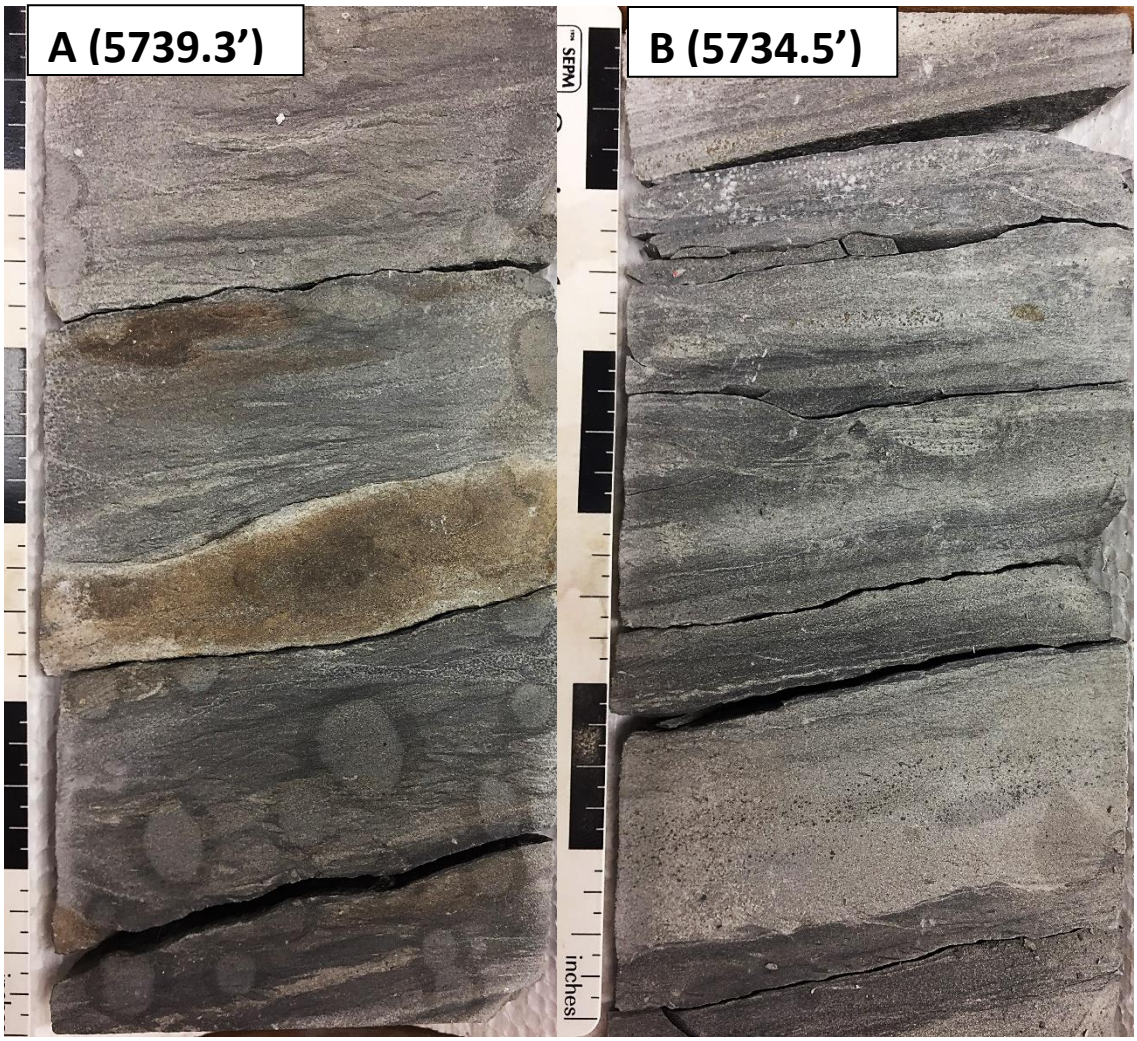

Figure 8: Core photographs of the sandstone lithofacies. Scales are in inches. (A) Dark grey sandstone with siderite banding (5739.3’). (B) Sandstone with planar bedding and bioturbation (5734.5’).

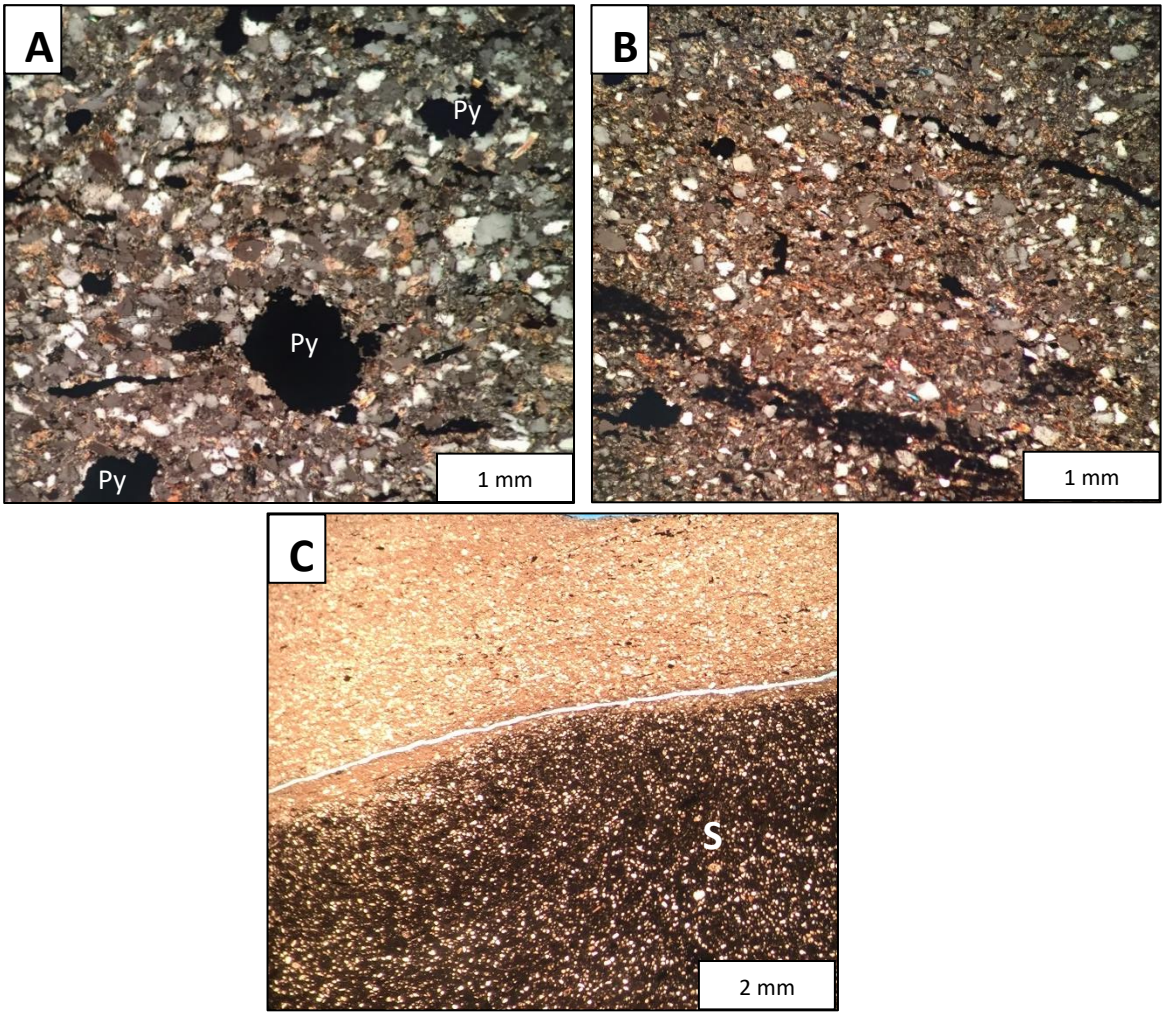

Figure 9: Thin section photomicrographs of the sandstone lithofacies. (A) Pyrite (Py) masses and detrital quartz grains in a clay matrix. (B) Detrital quartz and pyrite dispersed in a clay matrix. (C) A siderite cemented band (S) overlain by sandstone.

4.2 Siltstone

The rocks assigned to the siltstone lithofacies are light brown to medium gray siltstones (Fig. 10). Siltstone beds range in thickness from 1 cm to 3 dm. The average mineralogy of the siltstone lithofacies is 35.9% clay minerals (range = 22.0-50.0%), 5.2% carbonate (range = 0-13.0%), and 58.9% Q+F+P+A (range = 48.0-74.0%). Organic contents of the siltstones average 1.6% (range = 0.4-3.5%). Siltstones are generally laminated to massive (Fig. 10). Basal contacts are typically sharp to gradational, whereas upper contacts are generally sharp.

This facies is composed of detrital silt, sponge spicules, radiolaria, and calcispheres. (Fig. 11A, C). Carbonate silt, clay, and dispersed fine-grained pyrite masses are also observed (Fig. 11). Permeability and porosity average 681.7 nd (range = 163.0-1020.0 nd) and 7.4% (range = 4.4-10.0%), respectively, in this facies.

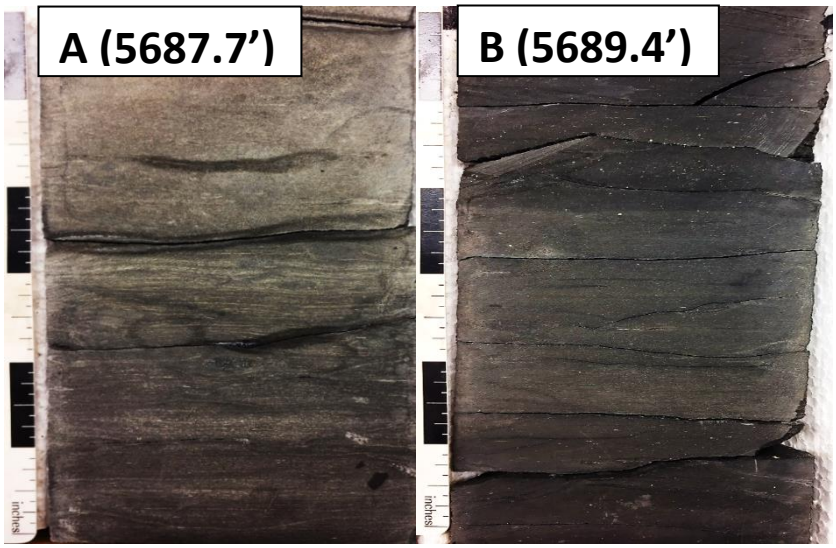

Figure 10: Core photographs of siltstone lithofacies. Scales are in inches. (A) Siltstone grading from siltstone with wavy and disrupted lamination into a massive tan colored siltstone (5687.7'). (B) Massive light brown siltstone overlain and underlain by siliceous mudstones. White specks are unidentified skeletal fragments (5689.4').

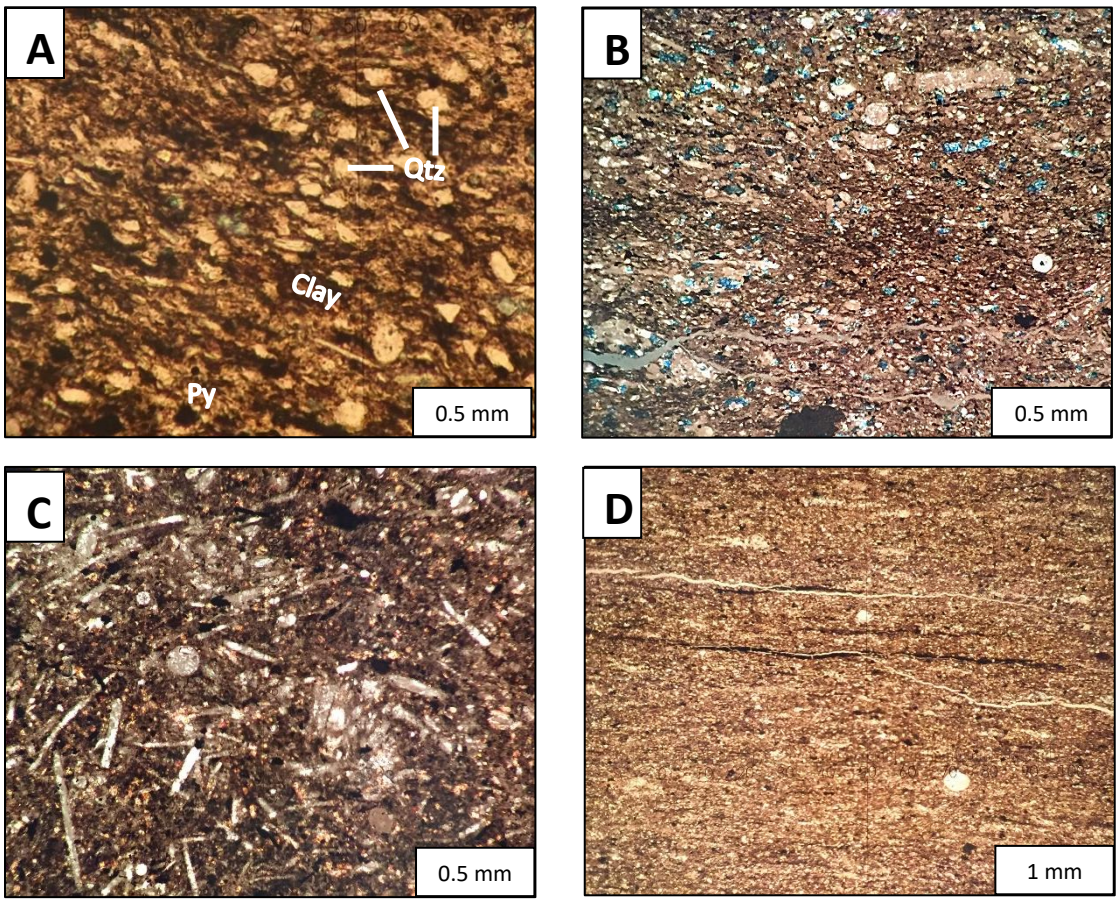

Figure 11: Thin section photomicrographs of the siltstone lithofacies. (A) Detrital quartz silt (Qtz) and pyrite (Py) in a clay matrix. (B) Laminated siltstone with dispersed carbonate grains and irregular silt stringers. (C) Siltstone composed of sponge spicules, radiolaria, detrital quartz, and pyrite in a clay matrix. (D) Laminated siltstone with parallel aligned silt stringers and algal cysts.

Interpretation

The Siltstone lithofacies is interpreted to have been deposited by a combination hemipelagic and pelagic processes. The parallel alignment of grains in the siltstone facies suggests deposition by bottom currents or low-density turbidity currents. Lack of sedimentary structures in the siltstones can be attributed to bioturbation or deformation by post-depositional gravity-driven processes (e.g. slumps, bottom currents; Fig. 12).

Figure 12: Photograph of core interval 5651'-5661' displaying a slump deposit comprised of contorted siltstone beds.

4.3 Siliceous Mudstone

Siliceous mudstones are characterized by light grey to black mudstones (Fig. 13). Siliceous mudstone intervals range from 1 cm to 4.5 m in thickness. The average mineralogy of rocks assigned to this facies are 57.8% clay (range = 45.0-68.0%), 2.9% carbonate (range = 0-13.0%), and 39.2% Q+F+P+A (range = 31.0-48.0%). TOC contents of the siliceous mudstones vary considerably, ranging from 0.2-6.3% (average 2.1%). Siliceous mudstones are generally laminated with silt or very fine sand forming mm-thick laminae. However, some siliceous mudstone intervals are homogenous likely due to sediment reworking by organisms. Lower and upper contacts of this facies are sharp to gradational. This facies is composed of silt and rare calcispheres in a clay matrix (Fig. 14). Fern-like plant fossils are commonly observed along the bedding planes of this facies. Phosphatic nodules and fine-grained pyrite masses are also observed. (Fig. 14). Permeability and porosity average 937.5 nd (range = 701.0-1130.0 nd) and 9.7% (range = 7.0-11.4%), respectively.

Interpretation

Siliceous mudstones were likely deposited by a variety of processes. Irregular silt stringers suggest deposition by density-flow processes (e.g. bottom currents, low-density turbidity currents) under anoxic conditions, as suggested by the presence of phosphatic nodules and lack of burrows. The presence of detrital quartz silt suggests contribution from the pelagic settling out of wind-blown silt derived from eolian systems to the north and northeast of the Midland Basin.

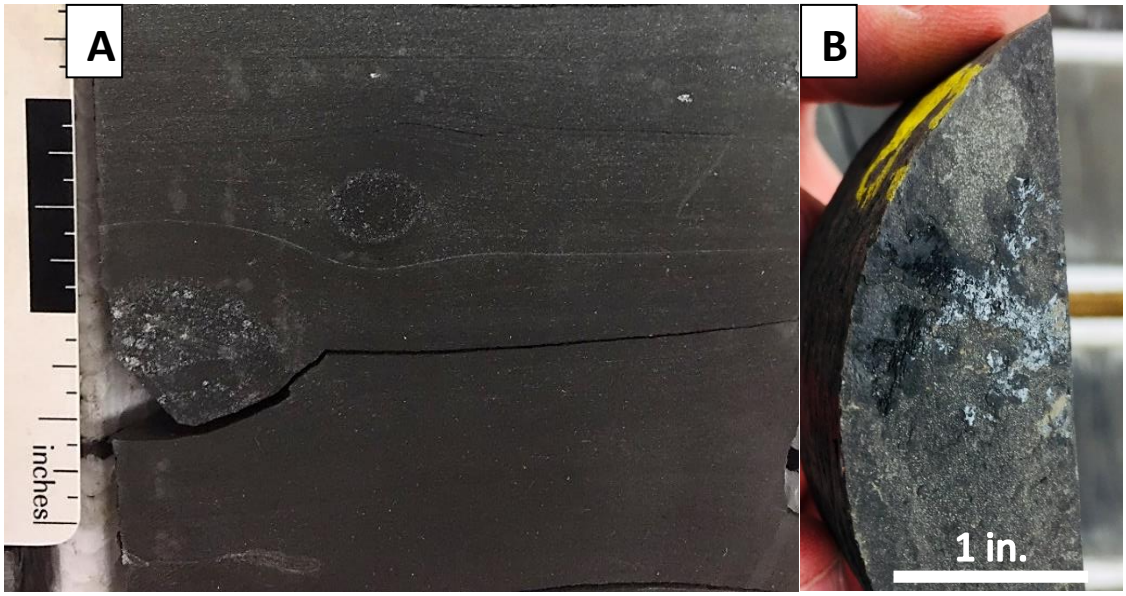

Figure 13: Core photograph of the siliceous mudstone lithofacies. Scales are in inches. Dark brown mudstone with two phosphatic nodules in the center and center-left of the photo (5511.9'). (B) Photograph of fern-like plant along the bedding plane of the siliceous mudstone lithofacies. From 5683.8'.

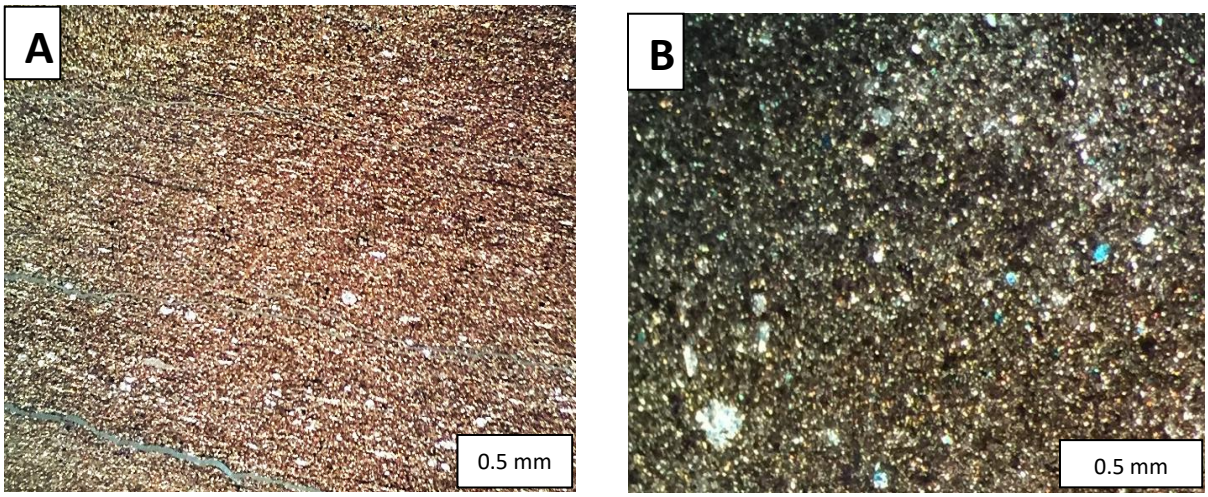

Figure 14: Thin section photomicrographs of the siliceous mudstone lithofacies. (A) Siliceous mudstone with a stringer of elongate detrital silt grains. (B) Homogenous mudstone with detrital silt and dispersed pyrite and carbonate silt.

The presence of well-preserved macroscopic plant fossils along the bedding planes of siliceous mudstones of the Wolfcamp has become the subject of recent studies (Baumgardner et al., 2016; Kvale et al., 2017). Baumgardner et al. (2016) studied drill cores from 14 wells to study relatively intact fossils of an early Permian peltasperm, which is a Paleozoic seed plant characterized by the presence of a specialized shield-like reproductive organ (pelta) (Baumgardner et al., 2016). Due to the abundance of these fossil plants in the siliceous mudstones between gravity-flow deposits it was interpreted that the plant debris was carried out to sea by surface currents before sinking to the basin floor and being subsequently buried by hemipelagic suspension fallout (Baumgardner et al., 2016).

4.4 Calcareous Siltstone

This facies is characterized by pale to medium grey calcareous siltstones (Fig. 15A-B). Calcareous siltstone beds range from 2 to 15 cm thick. Average mineral contents for calcareous siltstones are 21.5% clays (range = 7.0-33.0%), 28.1% carbonate (range = 17.0-45.0%), and 50.4% Q+F+P+A (range = 40.0-62.0%). TOC contents for calcareous siltstones average 1.5% (range = 0.5-2.4%). Calcareous siltstone beds are generally weakly laminated to massive. Some beds also exhibit both normal and inverse grading. Basal contacts with underlying facies are generally gradational to sharp. Upper contacts are typically sharp to gradational.

Calcareous siltstones are composed of moderately sorted subangular to subrounded detrital quartz silt, radiolaria, spherical carbonate-filled bodies (calcispheres?), and silt-sized carbonate and skeletal fragments (Fig. 16). Well-preserved fern-like plant fossils are observed along beddings planes (Fig. 15C). Average values for permeability and porosity are 543.8 nd (range =791.0-1090.0 nd) and 5.4% (range = 2.0-7.6%), respectively (Table 1).

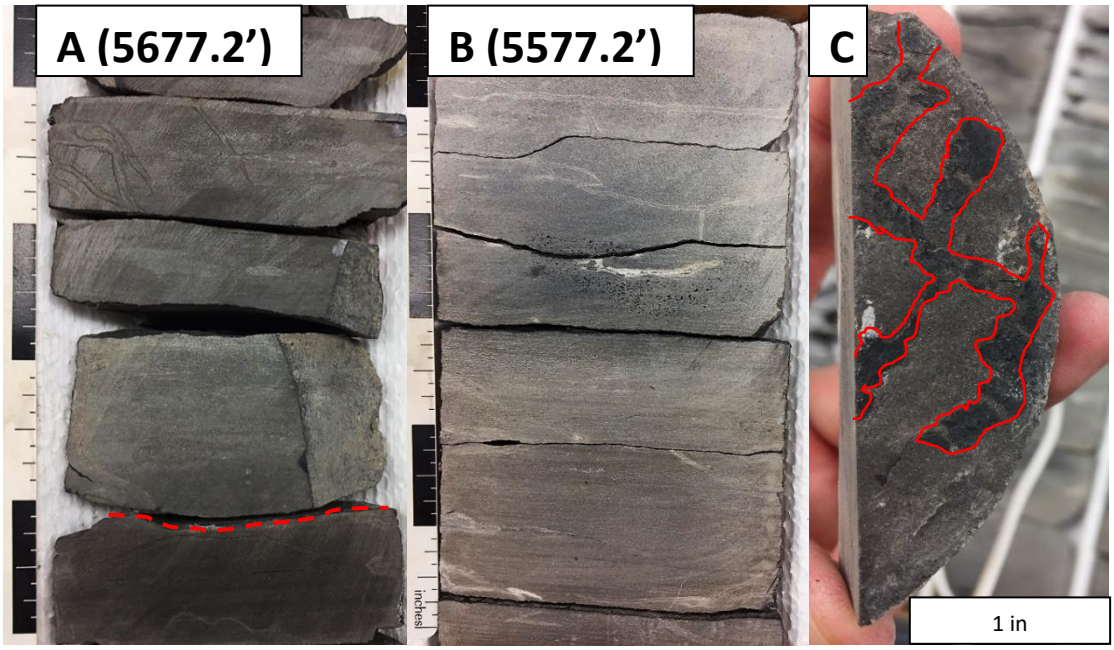

Figure 15: Core photographs of calcareous siltstone lithofacies. Scales are in inches. (A) Calcareous siltstone overlying a faintly laminated calcareous mudstone (5677.2’). The upper contact of the mudstone is marked by the red dashed line. (B) Weakly laminated calcareous siltstone (5577.2’). (C) Fossil of fern-like plant (outlined in red) along the bedding plane of a calcareous mudstone (5778.1’).

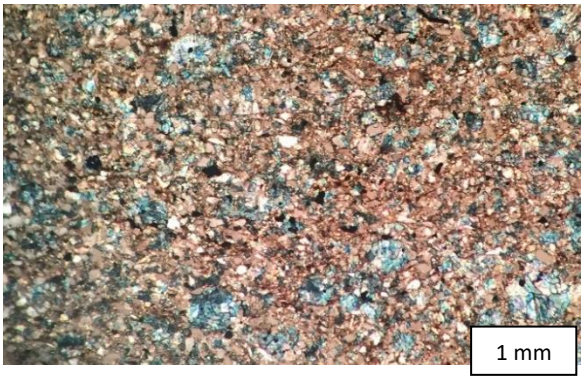

Figure 16: Thin section photomicrograph of the calcareous siltstone lithofacies. Spherical structures filled with ferroan dolomite and quartz silt in a clay matrix.

Interpretation

The presence of coarsening-to-fining upward cycles are indicative of waxing and waning flow regimes which are typical of deposits emplaced by hyperpycnal flows. Hyperpycnal flows are turbidity currents generated when rivers with high-suspended load concentrations enter the ocean and the differences in the densities of the riverine water and the ambient sea water generate a plunging flow into the deep basin. Hyperpycnites in the geologic record deviate from the standard turbidite model in that hyperpycnites have a basal coarsening upwards portion generated during the waxing period of fluvial discharge followed by an upper fining-upward unit deposited during the waning flow regime (Fig. 17; Mulder and Alexander, 2001). The intact macroscopic peltasperms along the bedding planes of calcareous silt beds indicate deposition proximal to terrestrial or marginal marine environments. Fluvially-driven hyperpycnal flows have been proposed to have transported intact plant debris into deep-water settings in Spitsbergen, Norway (Plink-Björklund and Steele, 2004).

Calcareous siltstones are also interpreted to have been deposited by a transitional flow distal to the marine margin, likely representing a lower H3 division of a calcareous hybrid event bed (Fig. 18; Kvale et al., 2017).

Recent studies have recognized the significance of flow evolution (e.g., non-cohesive turbidity currents to cohesive flows debris flows) over distances. Beds that preserve examples of transitional flow character are known as hybrid event beds (HEBS; Haughton et al., 2009). An ideal siliciclastic HEB deposit contains five internal divisions (Fig. 19). The base of the HEB will be a stratified or massive high-density turbidite (H1) overlain by a transitional banded unit (H2) that represents the flow transition from turbulent to laminar flow or vice versa. Overlying the transitional unit is a clay-rich, mud clast-bearing debrite (H3) that represents a quasi-laminar

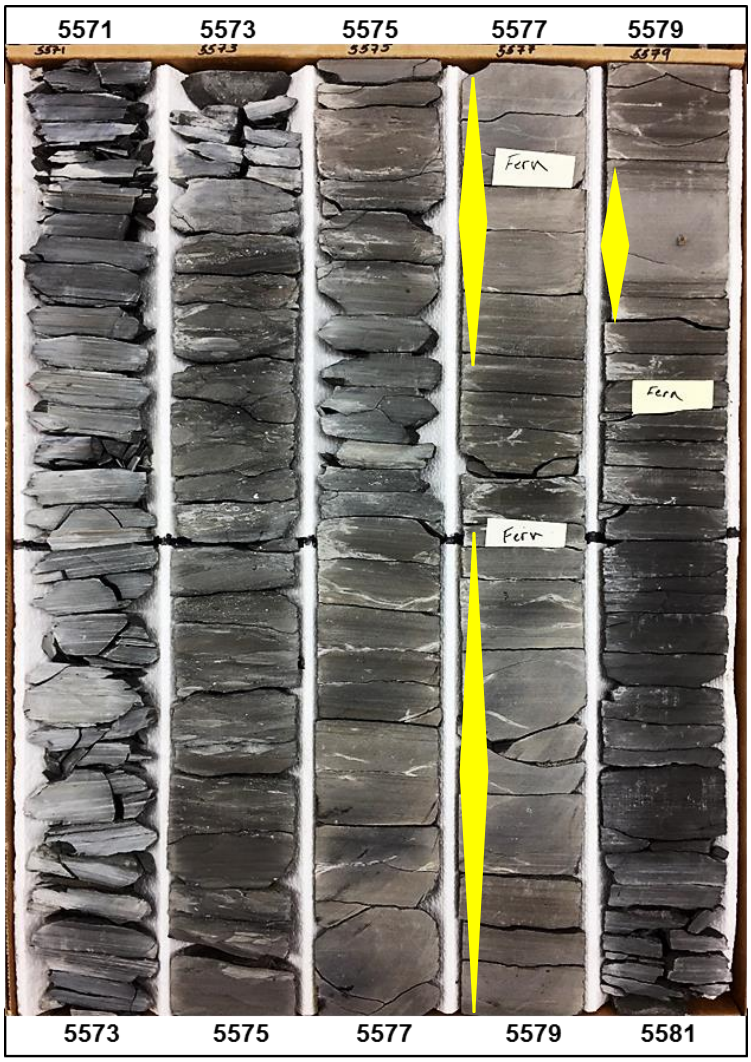

Figure 17: Corebox 5571'-5581' containing three coarsening-fining upward sequences (yellow diamonds) indicative of hyperpycnal deposits. Locations of plant fossils are indicated by pale yellow "Fern" cards.

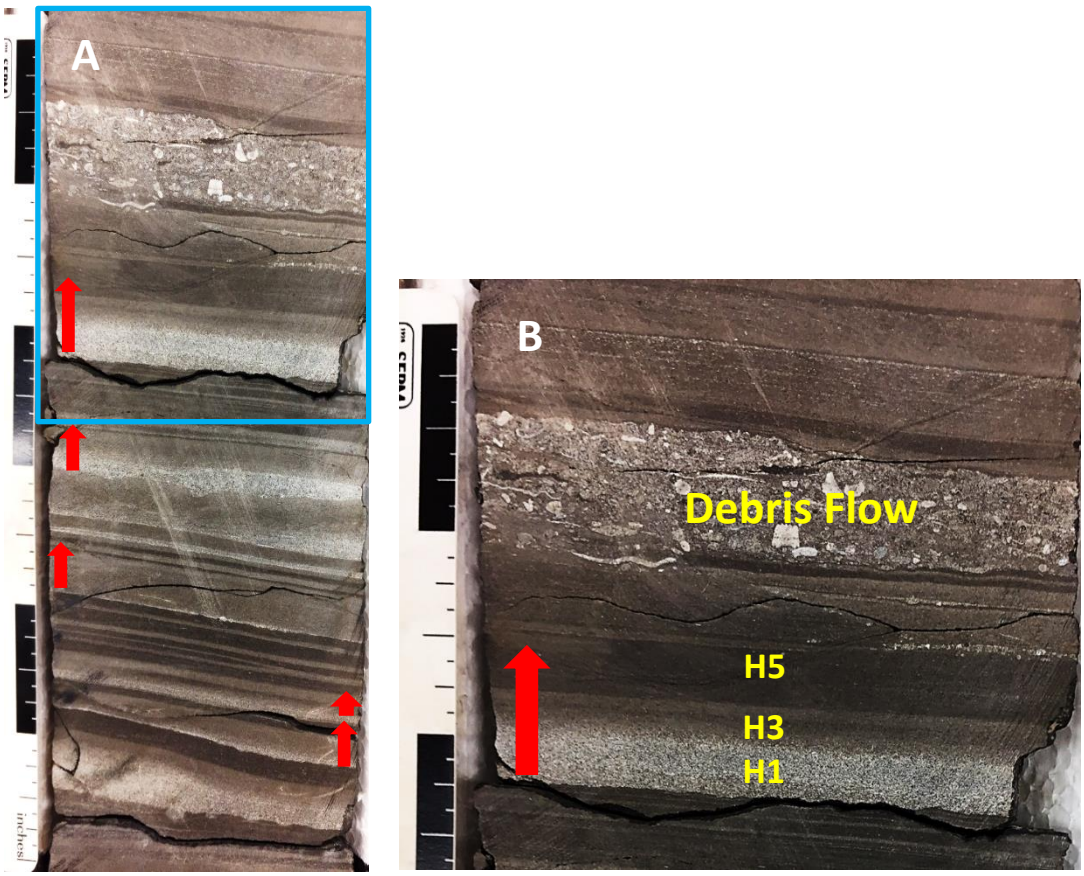

Figure 18: (A) Slabbed core photo of thin HEBs with interbedded calcareous siltstones and siliceous mudstones (Interval 5332.5'-5333'). The blue box indicates the location of B. (B) Close-up photograph of a calcareous HEB in the Strain core. Red arrows indicate single flow events. Scales are in inches.

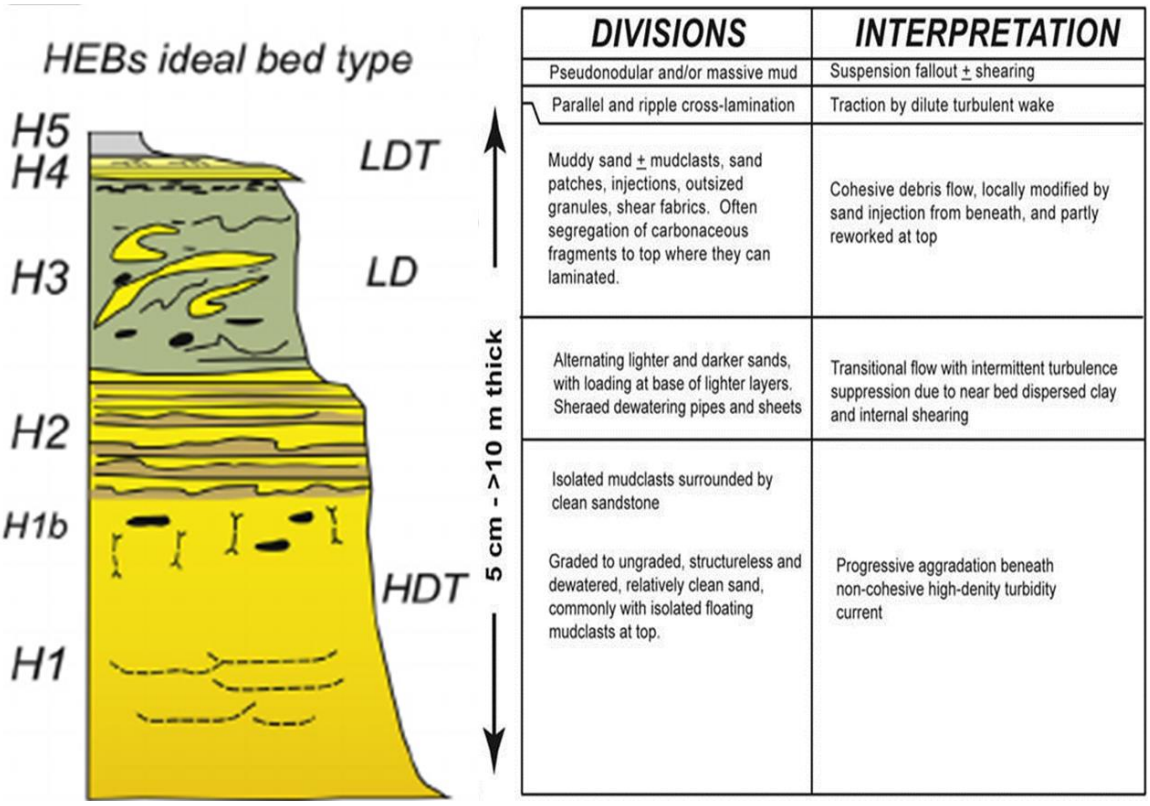

Figure 19: Schematic log of an ideal siliciclastic HEB deposit (from Haughton et al., 2009). HDT, LD, LDT stand for high-density turbidite, "linked debrite", low-density turbidite, respectively.

to laminar flow. The HEB is then capped by a sand-mud couplet consisting of a trailing turbulent flow (H4) overlain by suspension settling muds (H5).

The carbonate variants of HEBs described by Kvale et al. (2017) are characterized by a basal turbidite (H1) overlain by a laminated or banded calcareous siltstone (H2). This H2 division represents the transition of the gravity flow from a fluid turbidity current to a cohesive laminar debris flow. Overlying the H1 and H2 facies are calcareous-argillaceous siltstones (H3 lower) and calcareous mudstones (H3 upper). These facies represent the cohesive, mud-rich rear of the flow. Finally, the flow is capped by a massive mudstone (H5) deposited by suspension fallout (Kvale et al., 2017).

4.5 Calcareous Mudstone

The calcareous mudstone lithofacies is characterized by medium grey to dark grey calcareous mudstones (Fig. 20). Calcareous mudstone intervals range in thickness from < 1 cm to 1 dm. The average mineral contents of the calcareous mudstone facies is 39.75% clay (range = 38.0-42.0), 38.75% carbonate (range = 31.0-49.0%), and 21.5% Q+F+P+A (range = 19.0-24.0%). TOC contents within the facies range from 0.5 to 2.4% (average = 1.5%). Calcareous mudstones are generally weakly laminated with silt-sized carbonate grains, although massive textures are observed. The basal contacts of this facies are sharp to gradational. Upper contacts are generally sharp.

This facies is composed of silt-sized detrital quartz and unidentifiable carbonate silt grains in a mudstone matrix (Fig. 21). Pyrite is found in the facies as spherical masses (Fig. 21B, D). Permeability and porosity average 913.8 nd (range = 791.0-1090.0 nd) and 6.0% (range = 3.8-7.7%), respectively (Table 1).

Figure 20: Core photograph of the calcareous mudstone lithofacies. Scale is in inches. Laminated calcareous mudstone (5511.7').

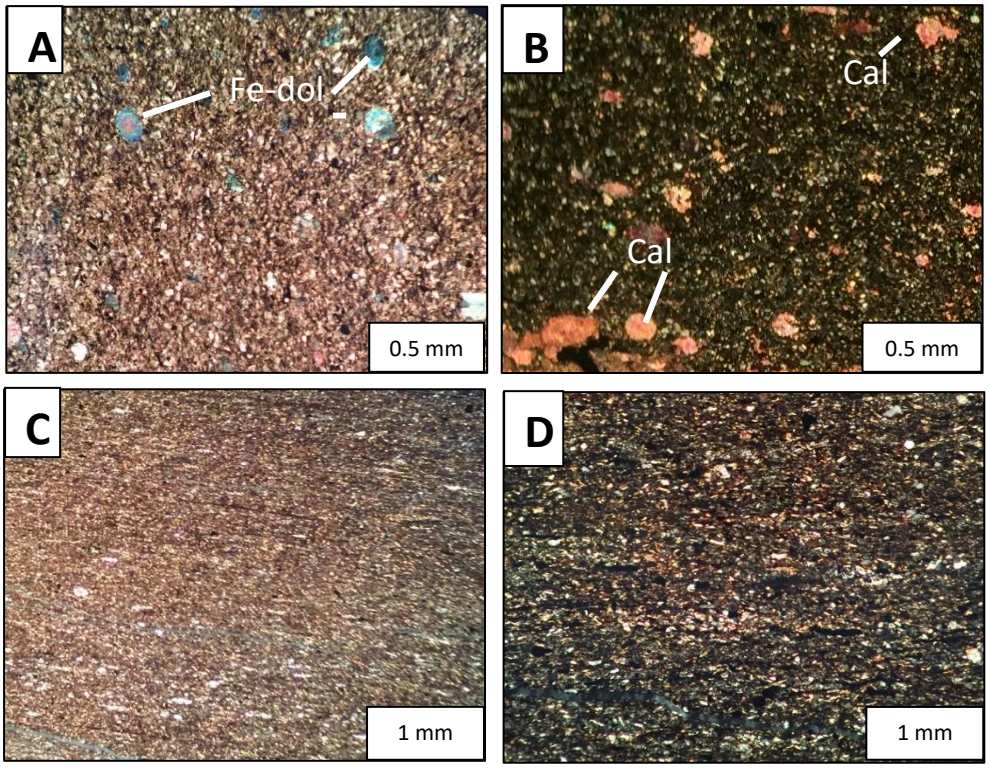

Figure 21: Thin section photomicrographs of the calcareous mudstone lithofacies. (A) Calcareous mudstone composed of mud, detrital silt, and spherical calcite and ferroan dolomite. (B) Calcareous mudstone composed of dispersed spherical calcite and pyrite. (C) Weakly laminated calcareous siltstone. (D) Dispersed carbonate, quartz silt, and fine-grained pyrite.

Interpretation

The calcareous mudstones of the Strain core are interpreted to have been deposited by a combination of density flows, pelagic rain, and hemipelagic processes. The abundance of quartz silt in this lithofacies indicate a likely contribution of sediment by eolian transport. The carbonate detritus within this lithofacies was likely derived from the adjacent carbonate platforms and deposited by hemipelagic processes. Calcareous mudstones may represent Te divisions of turbidites. Calcareous mudstones also may represent the cohesive H3 division of an HEB (Fig. 18B).

4.6 Calcarenite

Core intervals assigned to the calcarenite lithofacies comprise pale grey to brown fossiliferous wackestones, packstones, and grainstones (Fig. 22). Bed thicknesses range from < 1 cm to 3 dm. The average mineralogy of this facies is 4.3% clay minerals (range = 1.0-16.0%), 81.9% carbonate (range = 54.0-95.0%), and 13.7% Q+F+P+A (range = 3.0-36.0%). The TOC content of this facies ranges between 0.2-3.2% (average = 0.8%). Calcarenite beds are generally massive although some lamination and planar to wavy cross stratification do occur in the upper portions of calcarenite beds. Basal contacts of these beds are erosional, whereas upper contacts are typically gradational to sharp.

This lithofacies is composed of well to poorly sorted, fine to very coarse sand-sized carbonate debris, carbonate lithoclasts, and silty mudstone clasts. The identifiable skeletal components of this facies include fusulinids, crinoid ossicles, brachiopods, bivalves, and agglutinated foraminifera in a micrite matrix. Many of the fine-grained skeletal components of the calcarenites are indistinguishable (Fig. 23A-D). Calcarenites are also locally cut by calcite-healed fractures which vary from vertical to subhorizontal and are generally between < 1 mm to 1 cm wide. Permeability and porosity are typically low in this facies, averaging 222.4 nd (range = 6.6-1010.0 nd) and 2.5% (range = 0.6-8.1%), respectively (Table 1).

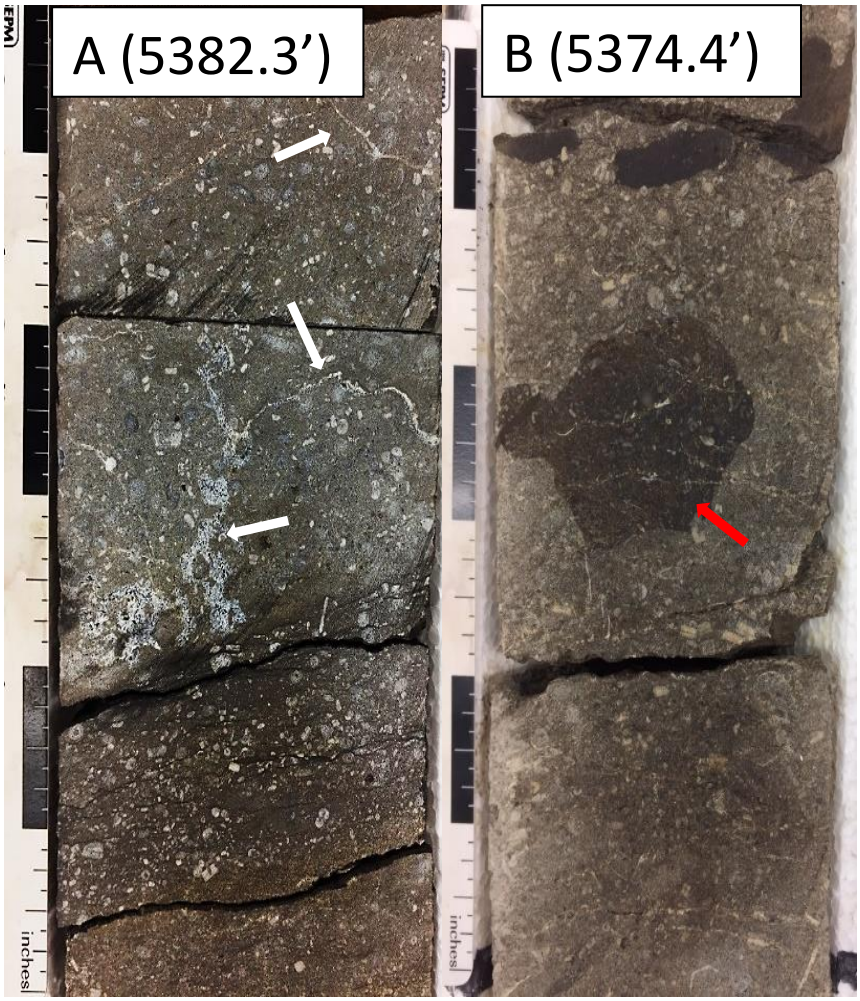

Figure 22: Core photographs of the calcarenite lithofacies. Scales are in inches. (A) Poorly sorted wackestone-packstone calcarenite with partially-filled, randomly oriented, calcite-healed fractures (white arrow) (5382.3’). (B) Poorly sorted grainstone-packstone with hydrocarbon-staining (red arrow) (5374.7’).

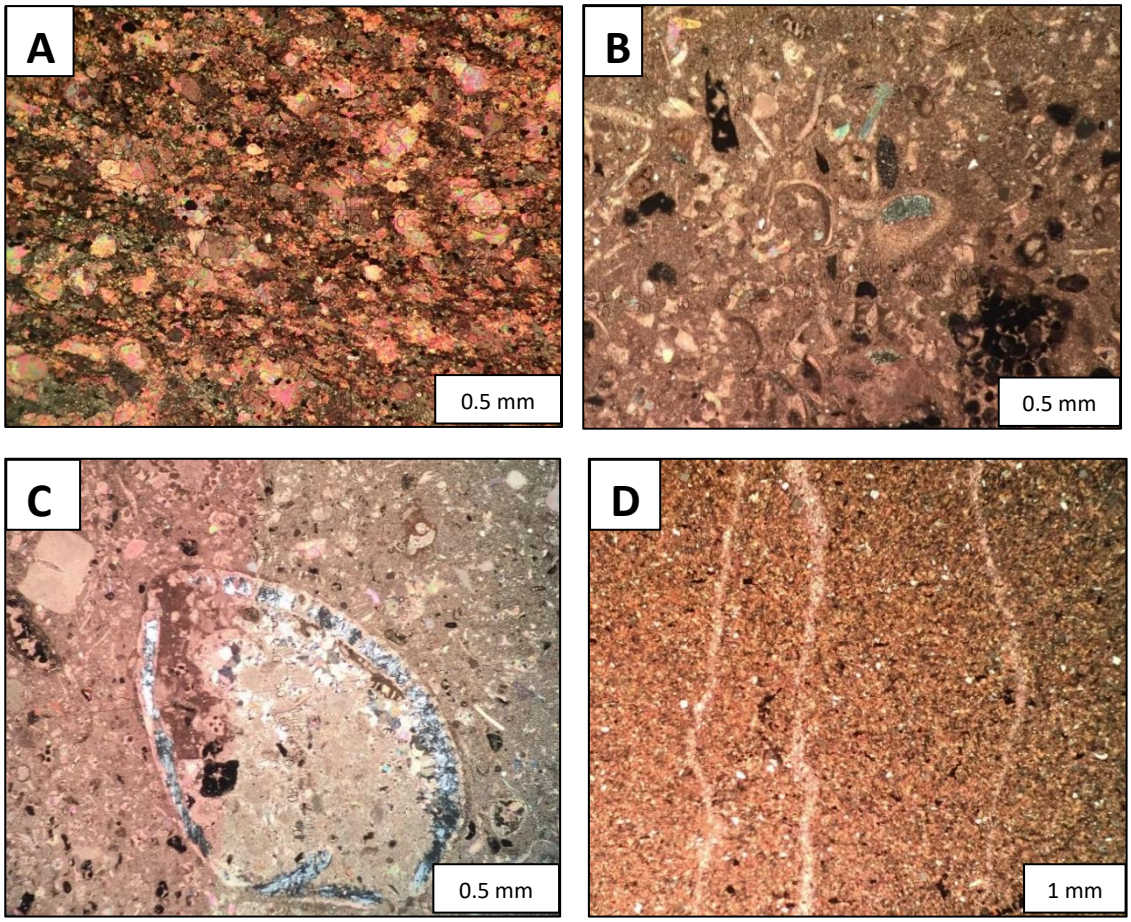

Figure 23: Thin section photomicrographs of calcarenite lithofacies. (A) Fusulinid packstone with micrite cement. (B) Poorly sorted allochems in a fossiliferous packstone. (C) Very coarse allochems and fine allochems in a fossiliferous wackestone-packstone. (D) Calcite-healed fractures in a packstone.

Interpretation

The calcarenite lithofacies is interpreted to have been deposited by turbidity currents which are common in carbonate slope settings. Thicker, massive calcarenites with erosional bases record high-energy depositional events and are likely proximal high-density turbidites (Fig. 22). These turbidites are characterized by the dominance of rapidly deposited beds typically assigned to the Ta division of the Bouma sequence. While Ta divisions are commonly recorded in the Strain core, more complete turbidite sequences are observed in thick-bedded calcarenites

(Fig. 24). In contrast, thinner, finer-grained calcarenites are interpreted to be more distal turbidites. Calcarenites deposited by turbidity currents also likely represent the basal H1 division of a calcareous HEB (Fig. 18B)

Turbidity currents are non-cohesive sediment flows that support sediment through fluid turbulence. These flows move downslope due to the contrast in density between the turbidity current and the surrounding water (Bouma et al., 1962; Middleton and Hampton, 1973; Mutti and Ricci Lucci, 1975; Stow and Shanmugam, 1980; Lowe, 1982; Stow and Mayall, 2000). Turbidity currents in the Wolfcamp were likely initiated by storms or by other mass-movement processes common in slope settings (e.g. slides, slumps, debris flows).

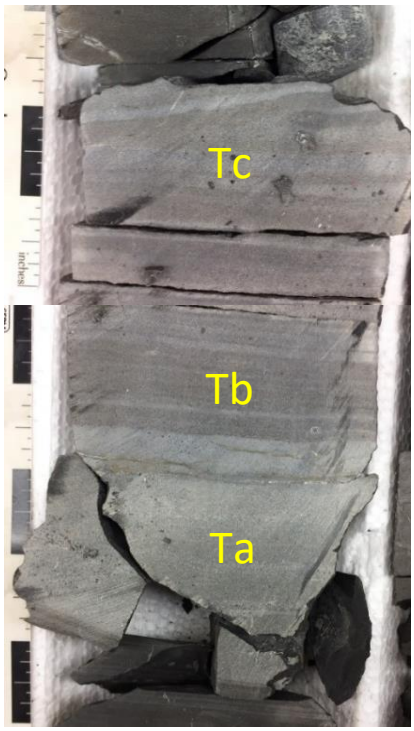

Figure 24: A calcarenite exhibiting massive Ta, cross laminated Tb, and ripple cross-laminated Tc divisions of the Bouma turbidite sequence (5667.7').

4.7 Bioclast-Lithoclast Wackestone-Floatstone

The bioclast-lithoclast wackestone-floatstone lithofacies is characterized by pale grey skeletal fragments and pale to dark grey lithoclasts encased in a dark grey silty, slightly calcareous mudstone or micritic matrix (Fig. 25). Bed thicknesses for this facies range from < 1 cm to 1 m. The average mineralogy of the lithofacies is 8.3% clay minerals (range = 1.0-13.0%), 65.6% carbonate (range = 51.0-74.0%), and 26.3% Q+F+P+A (range = 14.0-38.0%). TOC contents are variable in this facies, ranging between 0.5-3.4% (average = 2.2%). Core intervals assigned to this lithofacies are poorly sorted and massive (Fig. 25A). The contact with underlying facies are generally sharp to erosional. The upper contacts are also sharp to gradational.

Identifiable skeletal allochems include echinoderms, brachiopods, bivalves, and trilobite fragments. Lithoclasts within this facies are packstones and silty mudstone rip-up clasts (Fig. 26B-C). The long axes of lithoclasts often exceed the width of the core (8 cm). Permeability and porosity average 432.9 nd (range = 43.6-1030.0 nd) and 3.6% (range = 1.9-5.2%), respectively.

Interpretation

The bioclast-lithoclast lithofacies is interpreted to reflect deposition by debris flows, which are a major sedimentary process in submarine slope settings (Middleton and Hampton, 1973). In these flows, lithoclasts and skeletal fragments are supported and transported by a cohesive mixture of clay and interstitial water. The presence of clay matrices gives these flows a cohesive flow rheology, which is important for sustained movement and allows the flows to hold together during deposition (Bagnold, 1954; Lowe, 1982; Mulder and Alexander, 2001; Talling et al., 2012).

Debris flows can be initiated by failure of overloaded slope sediments caused by a catastrophic event or by the accumulation of many small failures. Debris flows can also form at the downslope ends of slumps and slides (Middleton and Hampton, 1973). These unstable slope settings may be a result of changes in base level, overproduction of carbonate on the platform, or tectonic subsidence.

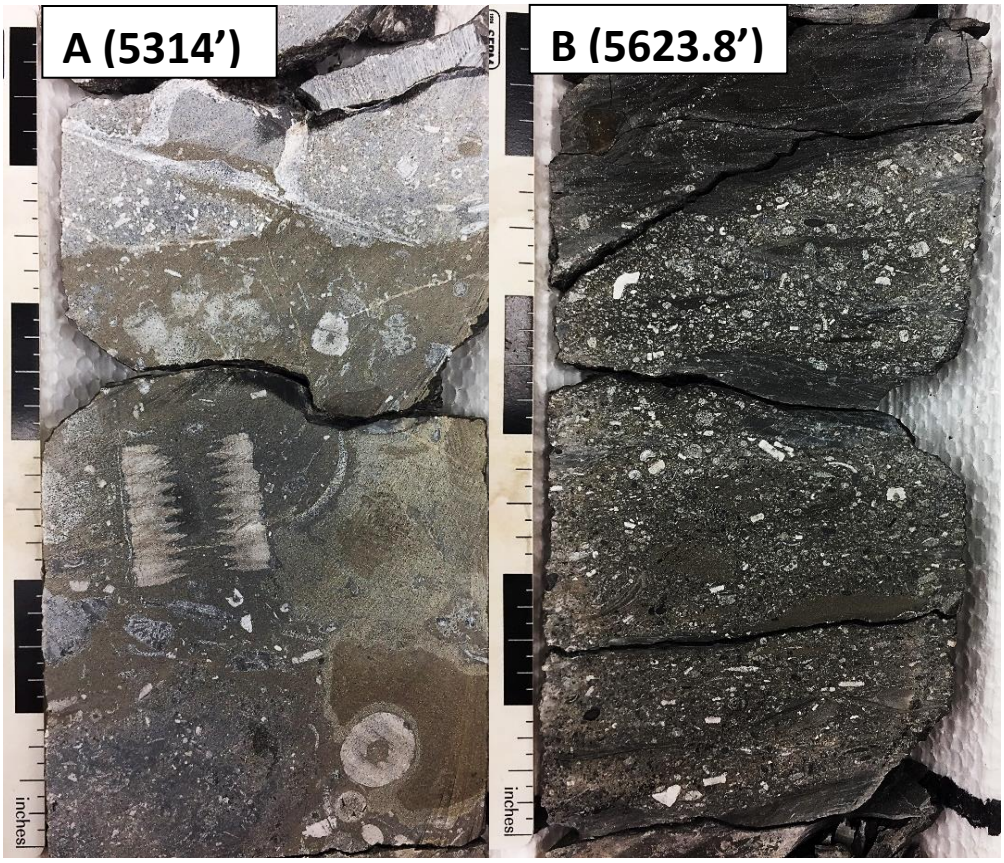

Figure 25: Core photographs of the bioclast-lithoclast wackestones-floatstone lithofacies. Scale is in inches. (A) Bioclast-lithoclast wackestones-floatstone comprised of skeletal fragments (crinoid ossicles) (5314.5'). (B) Bioclast-lithoclast wackestone-floatstone composed of poorly-sorted, ungraded, skeletal debris of crinoids and unidentifiable skeletal fragments and elongate mud lithoclasts (5623.8').

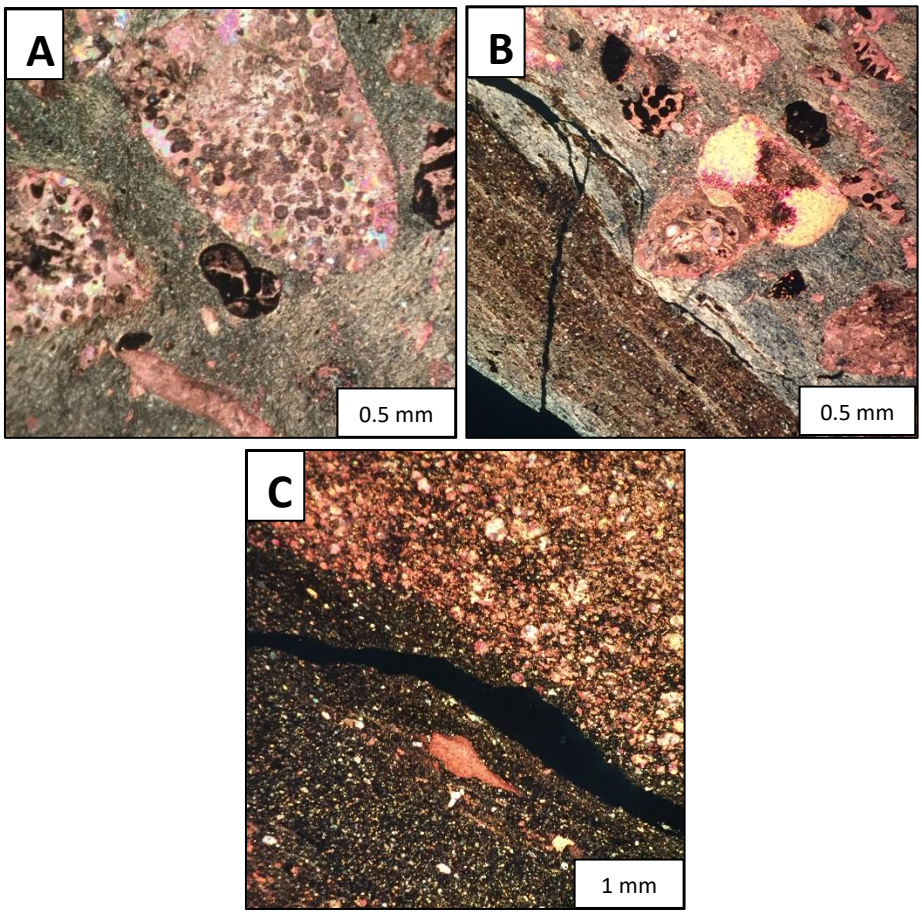

Figure 26: Thin section photomicrographs of the bioclast-lithoclast wackestone-floatstone lithofacies. (A) Poorly sorted skeletal fragments in a micritic matrix. (B) Mud lithoclast and skeletal allochems in a micritic matrix. (C) Packstone and unidentifiable carbonate fragments in a silty clay matrix.

CHAPTER 5: LITHOFACIES ASSOCIATIONS

Based on the lithofacies identified in the Strain core, their vertical distribution, and thicknesses, seven distinct lithofacies associations (LAs) are recognized within the study section (Fig. 27). These lithofacies associations are characterized by the dominant lithofacies and subordinate lithofacies within a given interval. Attention is also paid to lithofacies bed thicknesses. The lithofacies associations, in ascending order, are: 1) interbedded sandstone and siltstone lithofacies association (LA-A), 2) mudstone with rare siltstone, calcarenite, and bioclast-lithoclast wackestone-floatstone lithofacies association (LA-B), 3) calcarenites with interbedded bioclast-lithoclast wackestones-floatstone and mudstone lithofacies association (LA-C), 4) calcarenite and calcareous siltstone with interbedded calcareous mudstone lithofacies association (LA-D), 5) siliceous mudstone lithofacies association (LA-E), 6) massive calcarenite and rare mudstone lithofacies association (LA-F), and 7) mudstone with thin-bedded calcarenite and bioclast-lithoclast wackestones-floatstone lithofacies association (LA-G). Each of these lithofacies associations and their inferred depositional environments are summarized below.

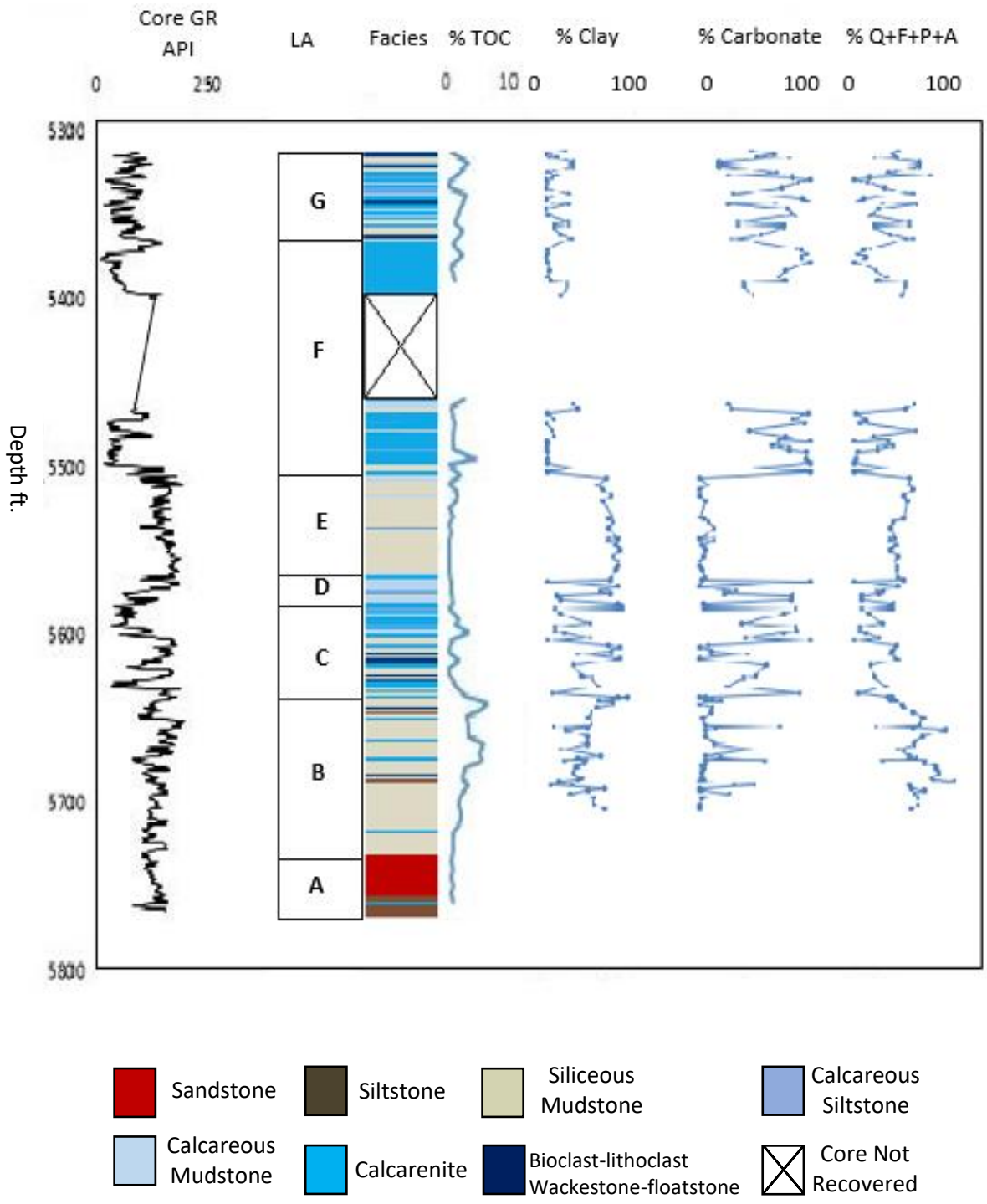

Figure 27: Core gamma, lithofacies associations, facies log, TOC, and XRD mineralogy of the Strain core.

5.1 Interbedded Sandstone and Siltstone (LA-A)

The LA-A characterizes the base of the study section (core interval 5728.4'-5766.5'). The facies association is dominated by siliciclastic facies (i.e. sandstone, siltstone) and characterized by a single coarsening-upward cycle from non-calcareous siltstones near the base of the section to sandstones towards the top (Fig. 28). The calcarenite facies is subordinate in this interval; represented by a single calcarenite bed 60-cm-thick and interbedded with basal silts. The coarsening-upward siltstone-sandstone package of this LA suggests that this interval may reflect sedimentation along the middle or lower slope in a transgressive-highstand systems tract.

5.2 Mudstone with Calcarenite and Bioclast-Lithoclast Wackestone-Floatstones (LA-B)

LA-B (core interval 5632'-5728.4') is composed of dark siliceous mudstones, light grey calcareous mudstones, and rare, thin-bedded silty calcarenites, and bioclast-lithoclast wackestones-floatstones (Fig. 29). The lower part of this association is dominated by mudstone beds over 10-m-thick, whereas the upper portions contain gravity flow deposits typically less than 15-cm-thick. Based on the sharp contact with the underlying LA-A, the dominance of dark-colored mudstones, and the thin-bedded character of gravity flow deposits, LA-B is interpreted to represent deposition in a lower slope environment.

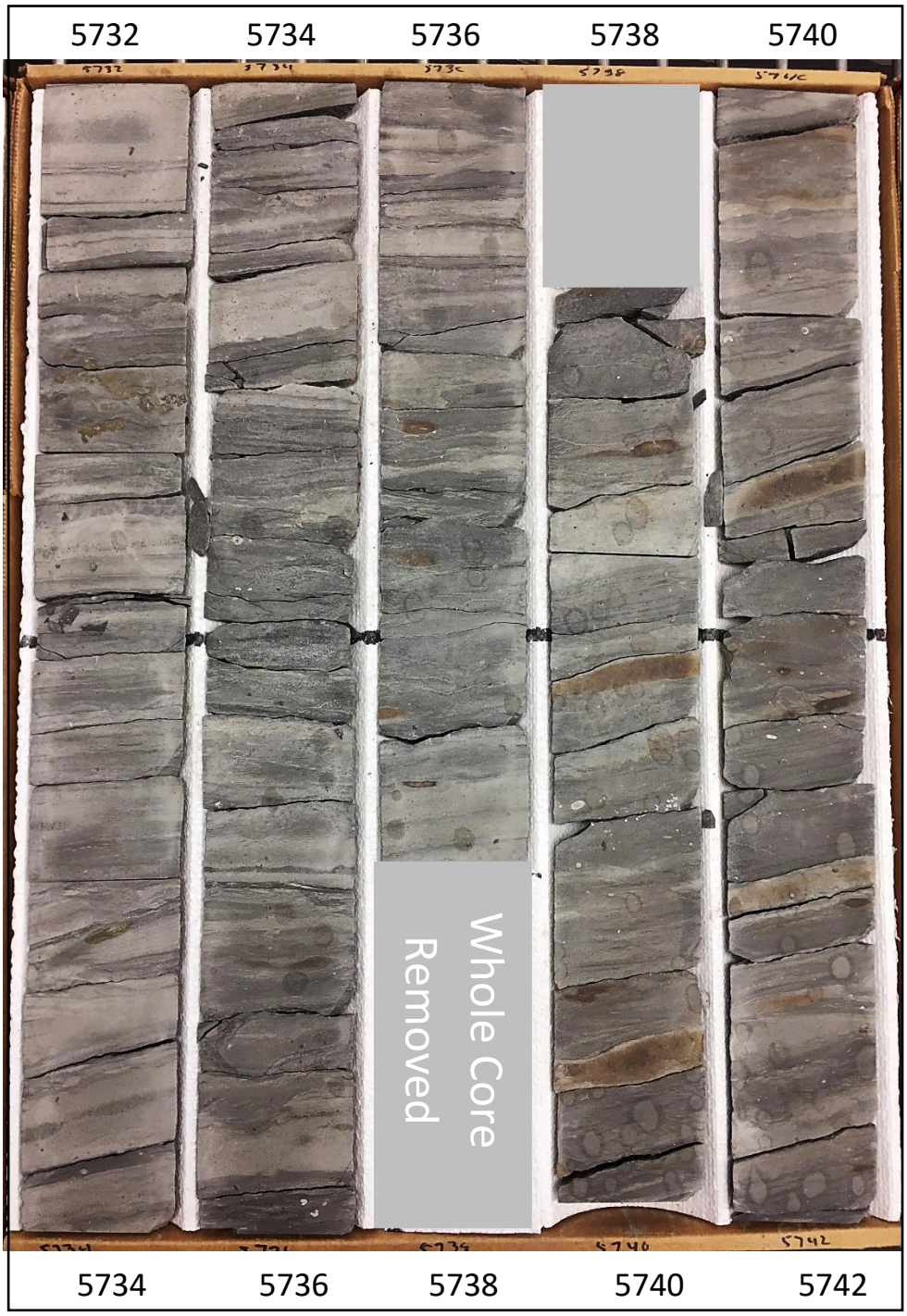

Figure 28: Photograph of core interval 5732'-5742' exemplifying LA-A.

Figure 29: Photograph of core interval 5672'-5682' exemplifying LA-B.

5.3 Calcarenite, Bioclast-Lithoclast Wackestone-Floatstone, and Mudstone (LA-C)

LA-C lies in sharp contact above LA-B extending from 5602.5'to 5632' in the core. LA-C is characterized by 3-m-thick fining-upward sequences of interbedded calcarenites, bioclast-lithoclast wackestones-floatstones, and siliceous mudstones (Fig. 30). Basal contacts of the calcarenites with bioclast-lithoclast wackestone-floatstones and mudstones are generally sharp. The presence of turbidites and debris flows indicate deposition in a proximal environment to the shelf margin. These deposits likely reflect sedimentation along the lower slope.

5.4 Calcarenite and Calcareous Siltstone with Interbedded Calcareous Mudstone (LA-D)

LA-D overlies LA-C at core depths 5573.2'-5602'. This association is characterized by the presence of high-frequency carbonate sediment gravity flows typically 15-cm-thick, represented by calcareous siltstones and calcarenites separated by calcareous mudstones (Fig. 31). This association generally fines upward with calcarenites and calcareous siltstones dominating lower and upper parts, respectively. Debris flows also are present but are typically less than a few cm thick. The high-frequency of carbonate gravity flows in this interval suggests that deposition occurred in a lower slope environment.

Figure 30: Photograph of core interval 5621'-5631' exemplifying LA-C.

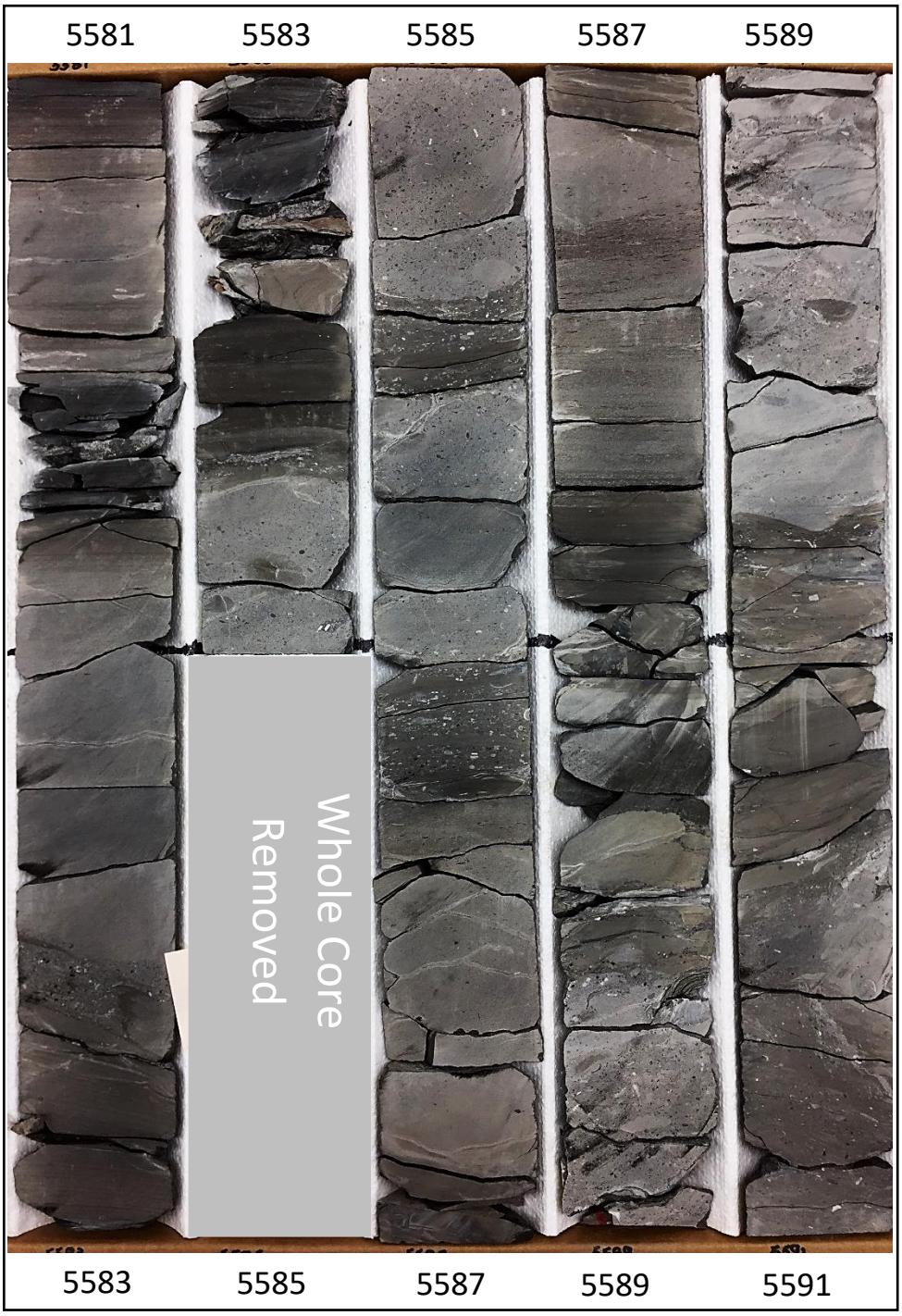

Figure 31: Photograph of core interval 5581'-5591' exemplifying LA-D.

5.5 Siliceous Mudstone (LA-E)

LA-E unconformably overlies LA-D and comprises the core interval 5501.3'-5573.2'. This lithofacies association is almost completely dominated by siliceous mudstones which are generally light grey in color with mm-thick laminae of silt and very fine sand (Fig. 32). The unconformable contact with the underlying LA-D suggests that this interval records a sea-level transgression over the Wolfcamp Shale Marker Unconformity. The environment of deposition was likely a sediment starved shelf. The presence of a significant unconformity in the Midland Basin during the Lower Permian has been explained in previous studies of the Wolfcamp Formation (Mazzullo and Reid, 1989; Flamm, 2008; Baumgardner et al., 2016).

5.6 Massive Calcarenite and Rare Mudstone (LA-F)

LA-F overlies LA-E and comprises the core interval from 5371.2'-5501.3'. LA-F is represented by abundant calcarenites with thin mudstone interbeds (Fig. 33). The calcarenite beds are typically massive, although some cross-stratification is observed. The thin, intervening mudstone beds are typically non-calcareous. The frequency of calcarenite deposits suggests deposition in a lower slope environment, possibly as channel fill deposits based on the thick-bedded nature of these deposits.

Figure 32: Photograph of core interval 5561'-5571' exemplifying LA-E.

Figure 33: Photograph of core interval 5485'-5495' exemplifying LA- F.

5.7 Mudstone, Thin Calcarenites, and Bioclast-Lithoclast Wackestone-Floatstones (LA-G)

LA-G represents the uppermost interval of the Strain core analyzed in this study (core interval 5312'-5371.2'). It is characterized by high proportions of mudstone relative to calcarenites and bioclast-lithoclast wackestones-floatstones (Fig. 34). Calcarenite beds are generally less than 30-cm-thick, although some thicker-bedded calcarenites are present. Bioclast-lithoclast wackestones-floatstone beds occur infrequently and are often 30-cm-thick, although some beds are less than a couple cm thick. Thin-bedded HEBs are also observed in this interval. The generally thin-bedded nature of sediment gravity flows in this interval likely reflect lower slope deposition during short-term sea-level cycles within longer-term late highstand conditions.

5.8 Sequence Stratigraphy and Sea-level Implications

Using the lithofacies associations presented in this chapter, this study, subjectively, interprets depositional environments, sea-level change, and sequence stratigraphy within the Strain core. Sedimentation during the deposition of the Wolfcamp Formation, previously, has been explained using a highstand shedding depositional model (Schlager et al., 1994; Montgomery, 1996; Mazzullo, 1998). In this model, adjacent carbonate platforms are exposed during sea-level lowstands. Under these conditions, dominant facies deposited in the basin were mudstones, siltstones, and sandstones. During sea-level transgressions, the platforms were progressively flooded, resulting in the transport of carbonate debris off of the platform by sediment gravity flows into the basin. During sea-level highstands, increased carbonate production along the platforms continued to supply carbonate debris into the basin with increased platform progradation and aggradation (Moore and Wade, 2013). The concepts presented in this model were used to interpret sea-level change and, ultimately, sequence stratigraphy of the Strain strata (Fig. 35).

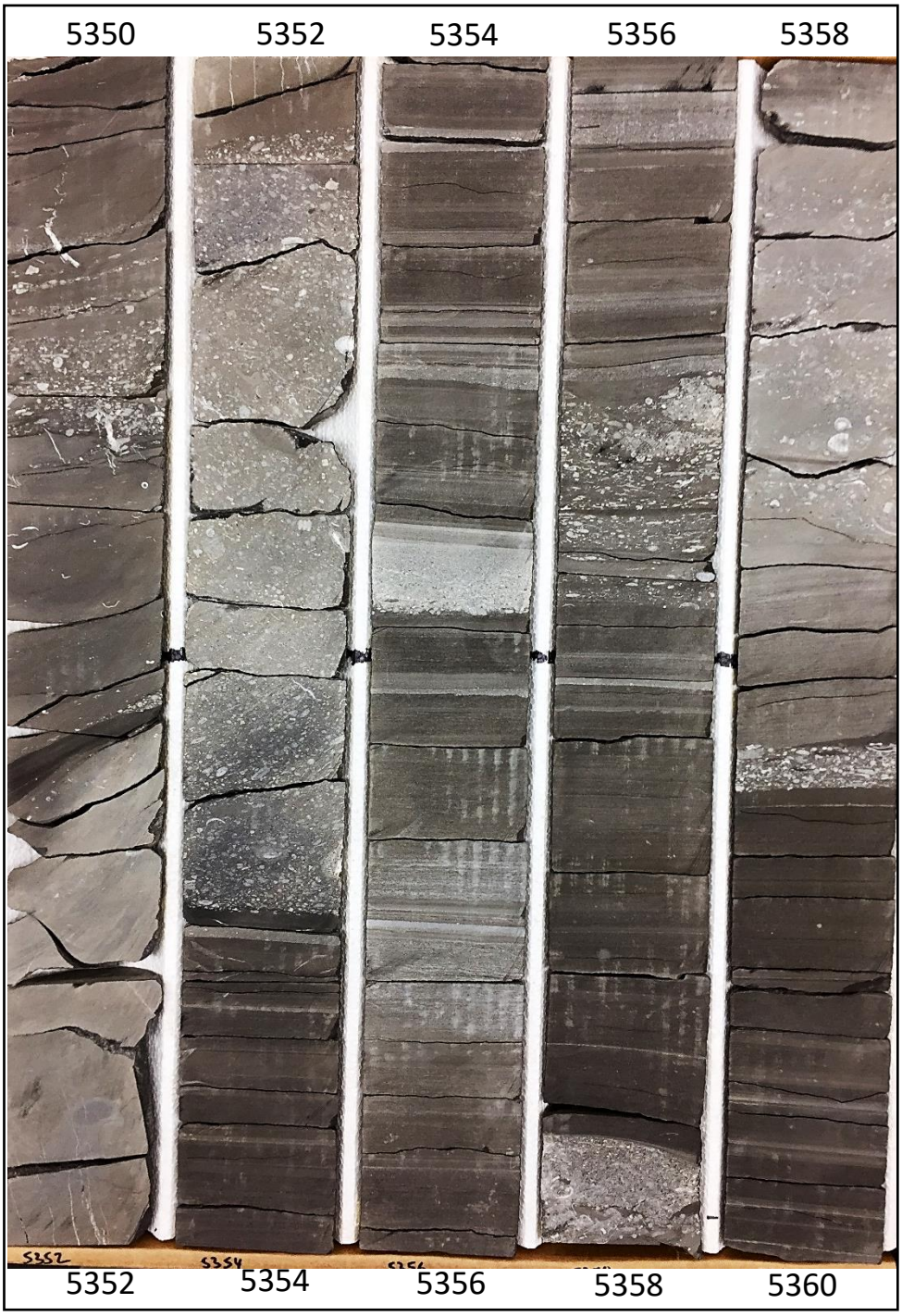

Figure 34: Photograph of core interval 5350’-5360’ exemplifying LA-G.

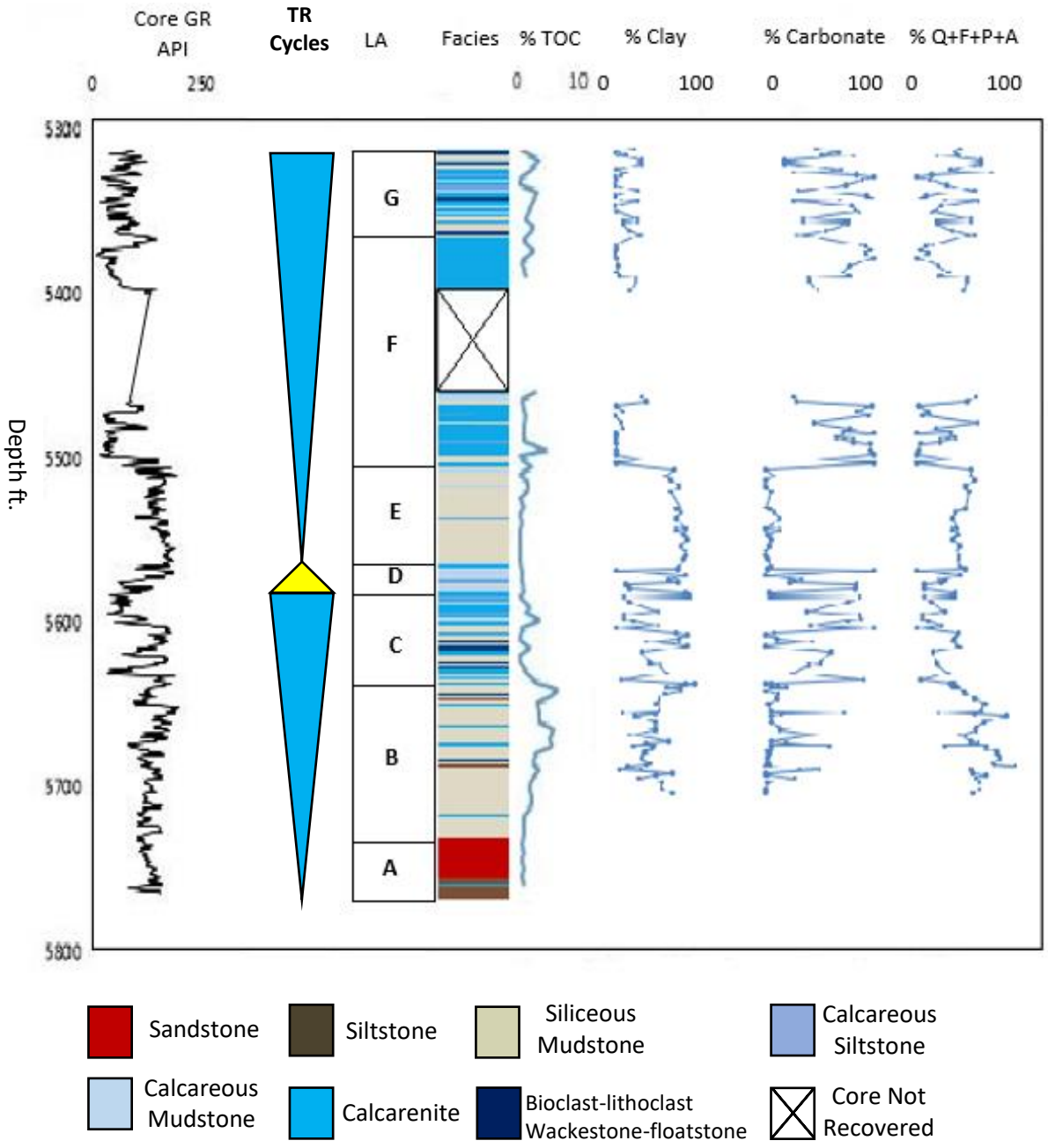

Figure 35: Core gamma, TR cycles, lithofacies associations, facies log, TOC, and XRD mineralogy of the Strain core.

Given the dominance of siliciclastics and the rare presence of carbonate within LA-A, this LA is interpreted to represent a sea-level lowstand deposit. Low sea-levels would have allowed terrigenous material to bypass the shelf and deposit directly into the Midland Basin. The overlying mudstone-rich successions of LA-B are interpreted to represent a transgressive systems tract. In Lithofacies Association C, the dominance of coarse carbonate detritus as high-frequency carbonate sediment gravity flows suggests that this lithofacies association represents a highstand systems tract. High sea-levels would have allowed for the carbonate factories of the adjacent shelves to continue producing carbonate material, which would deposit within the basin as sediment gravity flows. In LA-D, high-frequency carbonate gravity flows are present. However, the gravity flows fine towards the top of the succession from sand-sized carbonate debris to carbonate silt reflecting either a distal source or falling sea-levels. These conditions suggest that this LA represents a late highstand/falling stage systems tract. LA-E, which is dominated by mudstones and nearly devoid of carbonate beds likely represents a major sea-level transgression. The return to the deposition of carbonate debris in the overlying LAs suggests that another period of sea-level rise must have occurred in the Midland Basin. This interpretation fits the highstand-shedding model used to characterize the Permian Basin (Schlager et al., 1994). Based on this interpretation, the deposits of LA-F and LA-G are interpreted to represent a transgressive systems tracts and highstand systems tracts, respectively.

CHAPTER 6: LITHOFACIES HYDROCARBON RESOURCE POTENTIAL

Petrophysical, rock-eval, XRD, and XRF data were used to assess the hydrocarbon resource potential of the lithofacies identified in the Strain 2V core. Specifically, the hydrocarbon-source rock and hydrocarbon-reservoir rock potential of each lithofacies are evaluated based on cross-plots of petrophysical parameters and rock-eval pyrolysis data. To further understand the controls on source/reservoir rock quality, the relationships between lithofacies mineralogy, organic richness, and reservoir quality (e.g. permeability, porosity) were observed and are discussed in this section.

6.1 Hydrocarbon-Source Rock Potential and Characterization

The hydrocarbon-source rock potential of the lithofacies identified in the Strain core can be determined by using a cross-plot with logarithmic axes of S2 (measure of the remaining hydrocarbon generative potential) and TOC (Fig. 36; modified from Dembicki, 2009). Based on Figure 36, the best source rocks in the Strain are siliceous mudstones and calcareous and non-calcareous siltstones. These presence of anoxia indicators such as phosphatic nodules and limited bioturbation suggests that anoxia was a primary control on source rock quality. The sandstone and calcarenite lithofacies are generally the poorest-quality source rocks although some exceptions in the calcarenite facies are observed. Calcareous mudstones, which are not as calcareous as the calcarenites and bioclast-lithoclast wackestone-floatstone facies, display moderate source-rock potential. Bioclast-lithoclast wackestones-floatstone facies have variable source rock potential, ranging from poor to good source rock potential. The poor source-rock quality of calcareous lithofacies is likely a result of carbonate dilution on organic matter content those lithofacies. The sandstone lithofacies is a poor source rock due to the likely influence of

oxygen-rich water during the time of deposition, which would have greatly limited to amount of organic matter accumulation in the facies.

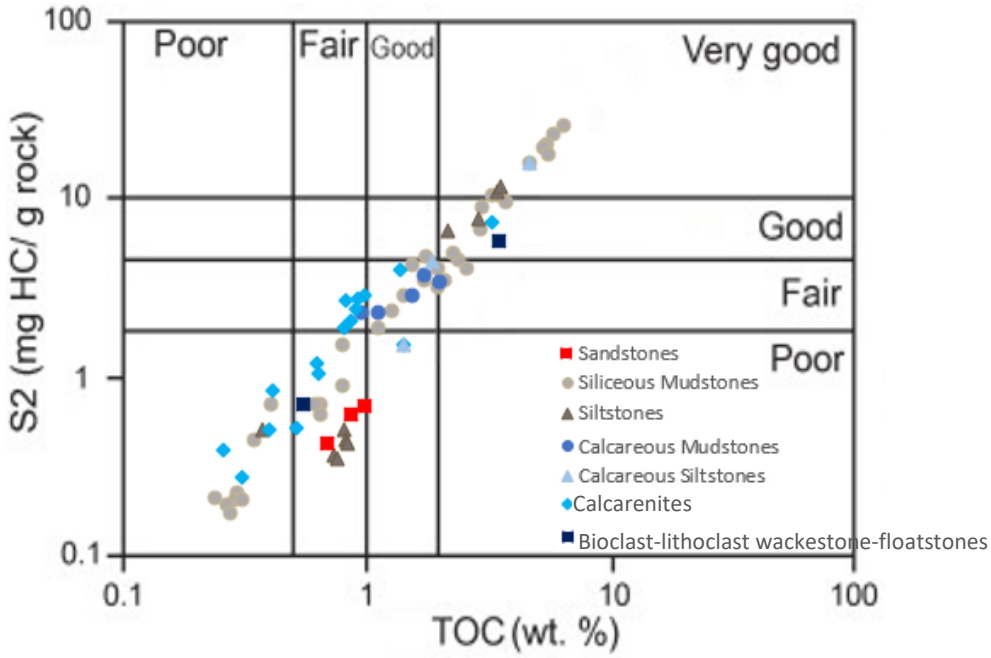

Figure 36: Cross-plot of S2 and TOC (after Dembicki, 2009). The fine-grained siliceous facies display the highest hydrocarbon-source rock potential. Calcareous mudstones display moderate source rock potential; however, more carbonate-rich facies are poorer source rocks.

To determine the relationship of facies lithology and organic richness, %Ca, %Si, and %Al (proxies for carbonate, quartz, and clay minerals, respectively) determined by XRF are plotted against TOC (Fig. 37). The relationships between mineralogy and TOC, shown in Figure 37, suggest that organic richness is directly controlled by lithology. TOC is observed to decrease with increased Ca in the system. Conversely, increases in %Si result in increases in organic-richness. %Al is generally associated with increased TOC, although TOC is observed to decrease at the highest concentrations of Al. These results indicate that siliceous and argillaceous facies are the most organic-rich facies and highest quality hydrocarbon-source rocks in the Wolfcamp.

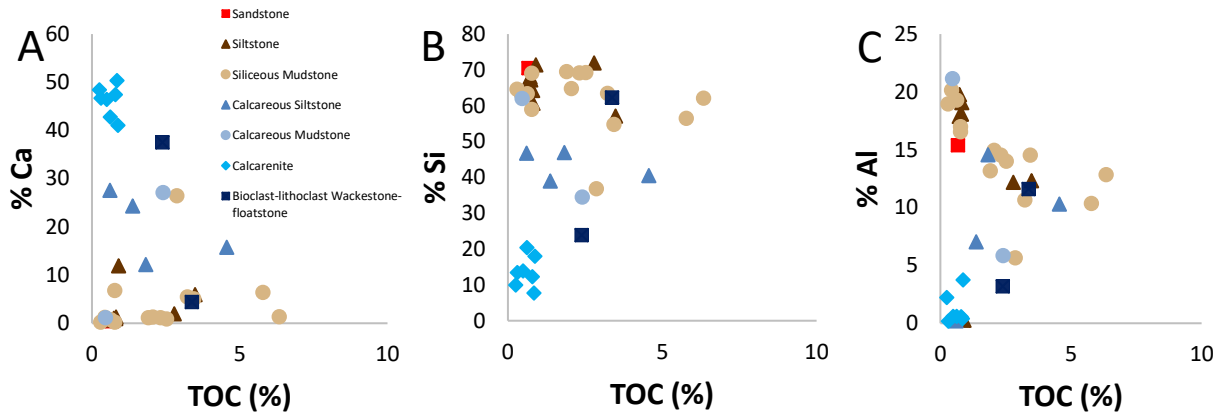

Figure 37: Cross-plots of %Ca (A), %Si (B), %Al (C) versus TOC. Increased Ca has a negative correlation with TOC while Si and Al both exhibit generally positive associations with TOC.

The thermal maturation of organic matter in a source rock can be estimated from Tmax values attained from Rock-eval pyrolysis. The Tmax values for the Wolfcamp Formation range from 423-510°C (average 442°C). These values suggest that the maturity of the Wolfcamp Formation ranges from slightly immature for more calcareous facies to slightly overmature in some siliceous mudstones, with the majority of samples falling within the oil window (435°-465°C) regardless of facies (Fig. 38). The cross-plot of S1 versus TOC can be used to assess whether hydrocarbons in the system were sourced locally (indigenous) or migrated from another source rock (non-indigenous). The data suggests that most hydrocarbons in the Strain core are indigenous to the system, likely from the interbedded mudstones, although hydrocarbons in some calcarenite samples reflect a non-indigenous origin.

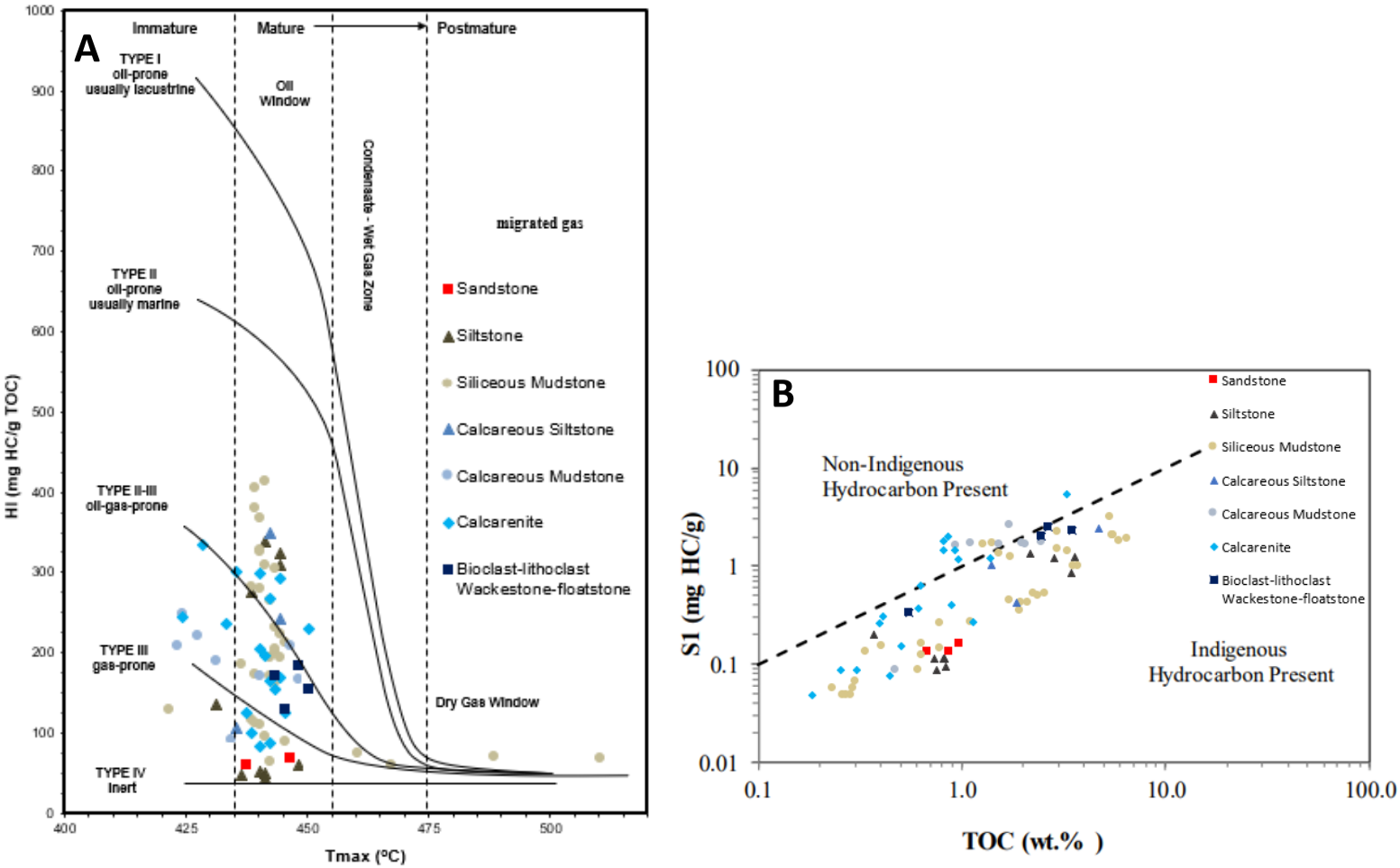

Figure 38: Cross-plots reflecting maturity and nature of hydrocarbons. (A) Cross-plot of hydrogen index versus Tmax. Most samples from the Strain core are within the oil window with a few samples indicating immaturity. Some overmature samples are also observed. (B) Cross-plot of S2 versus TOC distinguishing hydrocarbons indigenous to the source rocks and hydrocarbons that have migrated.

The kerogen type controls whether a source rock will be oil-prone (Type I, II) or gas-prone (Type III, IV). Plots of HI and OI can indicate the kerogen type of a source rock when plotted on a Van Krevelen diagram (Fig. 39A). A Langford and Blanc-Valleron plot of S2 versus TOC can also indicate kerogen type (Fig 39B). Both plots indicate a mixed Type II-Type III kerogen in the Strain core, although a few samples do fall into the category of Type IV kerogen likely due to oxidation or recycling. Sandstone facies consistently plot in the Type III field. Siliceous mudstones show the greatest variability in kerogen type plotting within the fields for Type II, Type III, and mixed Type II-III. Given the abundance of coastal peltasperms in Permian Basin during the Lower Permian, a significant contribution of organic matter in the Wolfcamp Formation likely came from land plants (Baumgardner et al., 2016; Kvale et al., 2017). Evidence for terrestrially-sourced organic matter can be observed by the presence of well-preserved plant fossils along the bedding planes of mudrocks and siltstones in the Strain core.

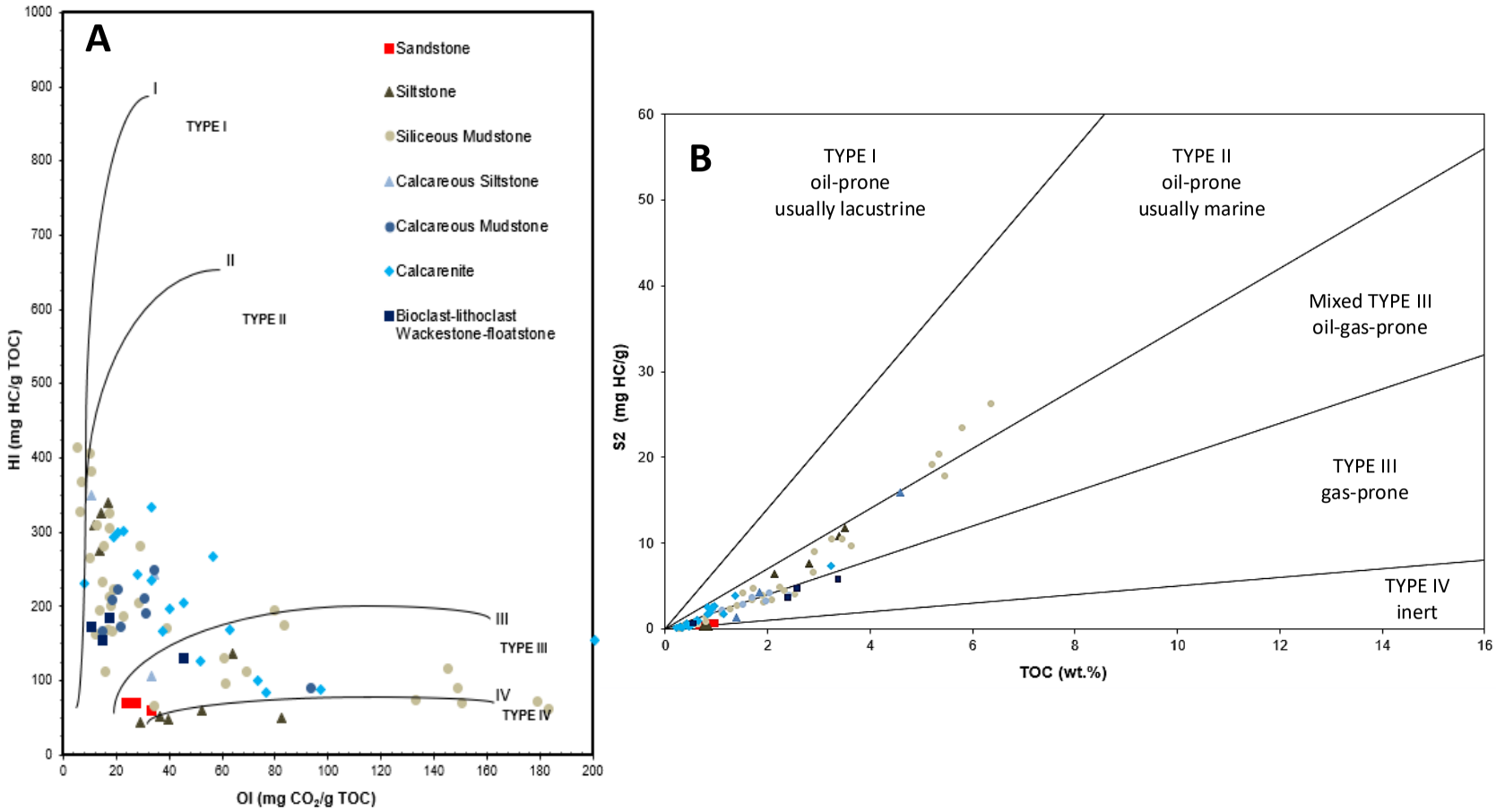

Figure 39: Cross-plots distinguishing kerogen type in the Strain core. (A) Van Krevelen diagram of Strain 2V strata. Most Strain 2V samples consist of a mix of Type II and Type III kerogen. A few samples do fall into the category of Type IV kerogen likely due to oxidation or recycling. (B) Langford and Blanc-Valleron kerogen type diagram.

6.2 Hydrocarbon-Reservoir Rock Potential

To demonstrate the hydrocarbon-reservoir rock potential of the identified lithofacies, permeability (in nd) was plotted versus porosity in Figure 40. Based on Figure 40, there are three distinct clusters of data points. Lithofacies that have between 1 and 4%, 4 and 8%, and 8 and 12% porosity are considered poor, moderate, and high-quality reservoirs, respectively.

Calcarenite and bioclast-lithoclast wackestones-floatstone lithofacies have the poorest reservoir rock potential. This is likely due to carbonate cementation during diagenesis. Moderate reservoir rocks include sandstones, calcareous and non-calcareous siltstones, and calcareous mudstones. The highest quality lithofacies in the Strain core are siliceous mudstones due to the lack of carbonate cementation.

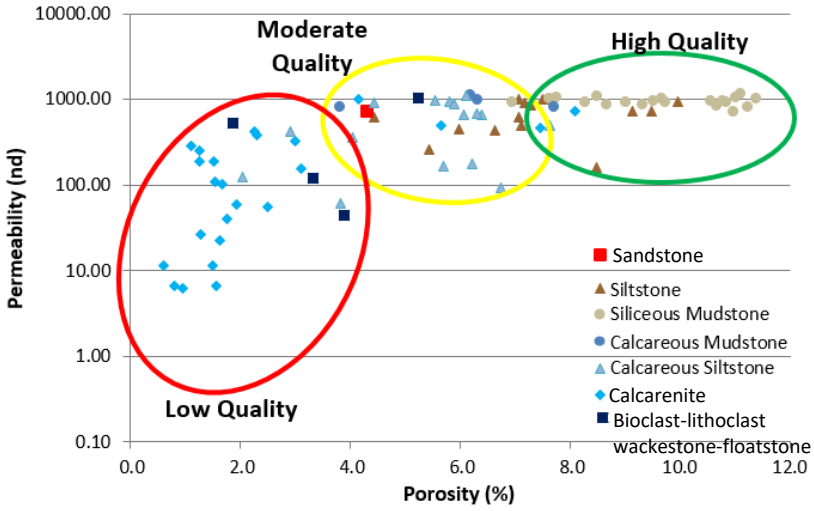

Figure 40: Cross-plot of permeability (in nd) versus porosity. Colored ovals indicate facies with low, moderate, or high reservoir quality based on porosity and permeability.

The relationship between lithofacies petrophysical properties (i.e. porosity, permeability) and lithology (i.e. silica, clay, carbonate content) were analyzed through cross-plots of petrophysical data versus XRD mineralogy in Figures 41-43. Based on these plots, petrophysical properties are strongly dependent on lithology. These data indicate a general negative correlation

between reservoir quality and carbonate (calcite and dolomite) content (Fig. 41), i.e. higher levels of carbonate content correspond to decreased porosity and permeability. However, some samples exhibit both relatively high porosity and permeability despite high carbonate concentrations. Porosity and permeability generally increases with increasing quartz content (Fig. 42). Clay is strongly correlated to enhanced porosity and permeability (Fig. 43).

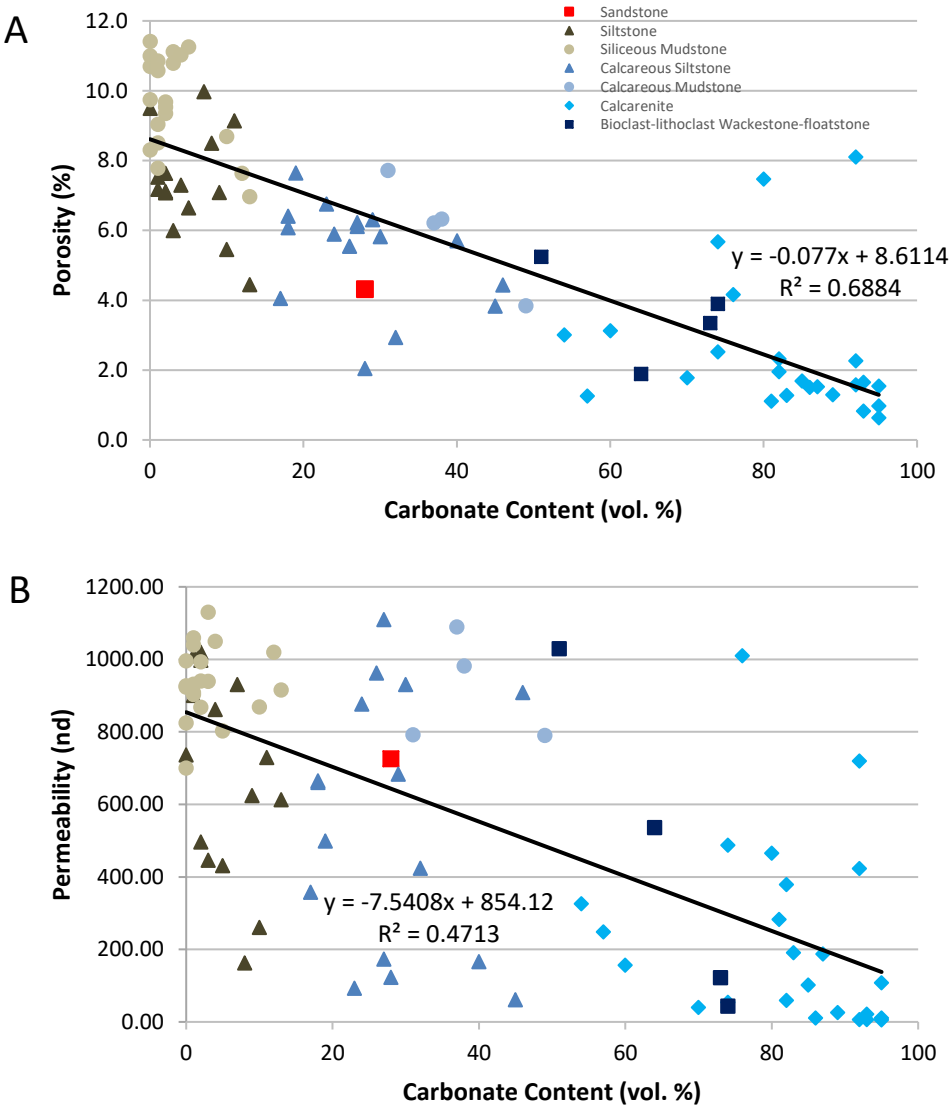

Figure 41: Cross-plots of carbonate content versus porosity (A) and permeability (B). Carbonate is generally negatively associated with reservoir quality.

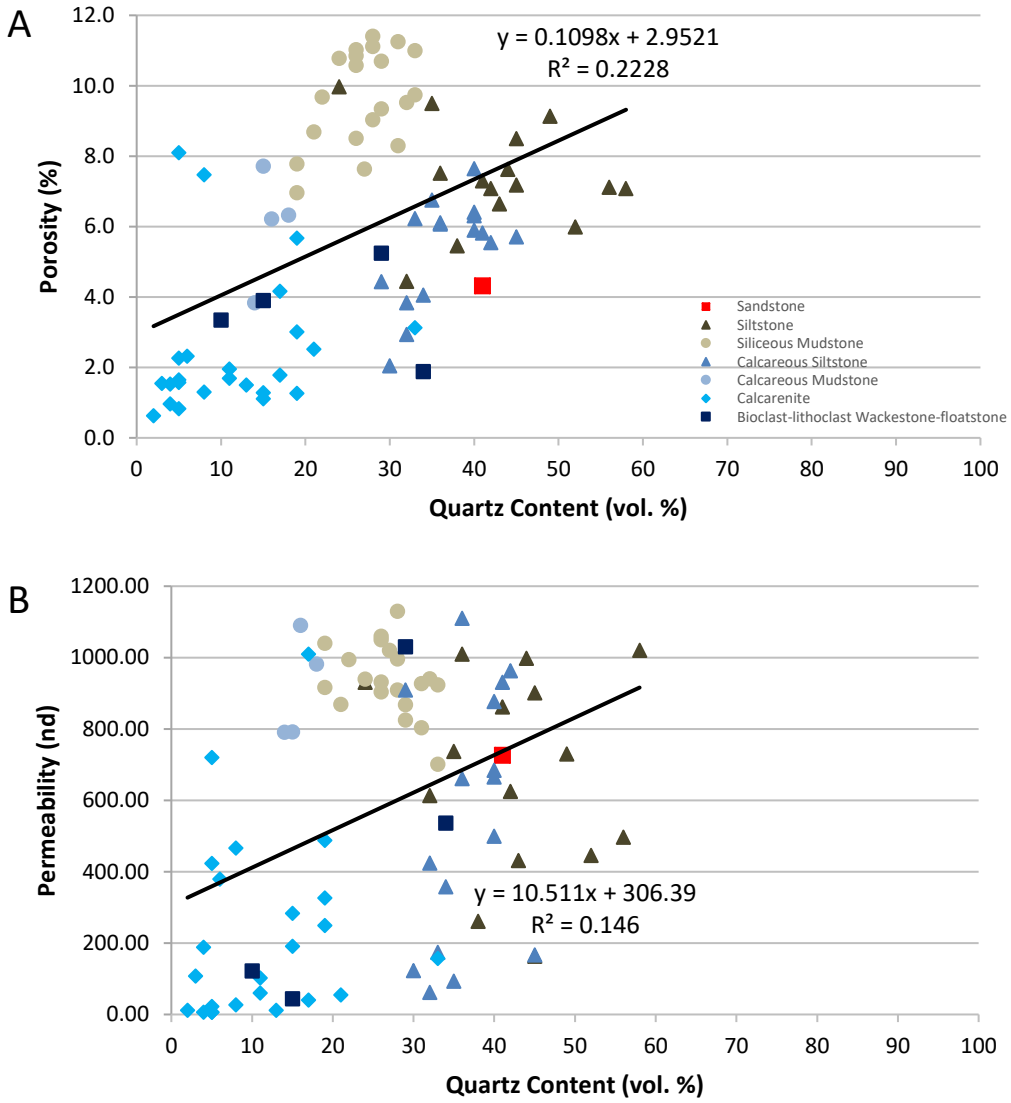

Figure 42: Cross-plots of quartz content versus porosity (A) and permeability (B). Quartz is positively associated with reservoir quality.

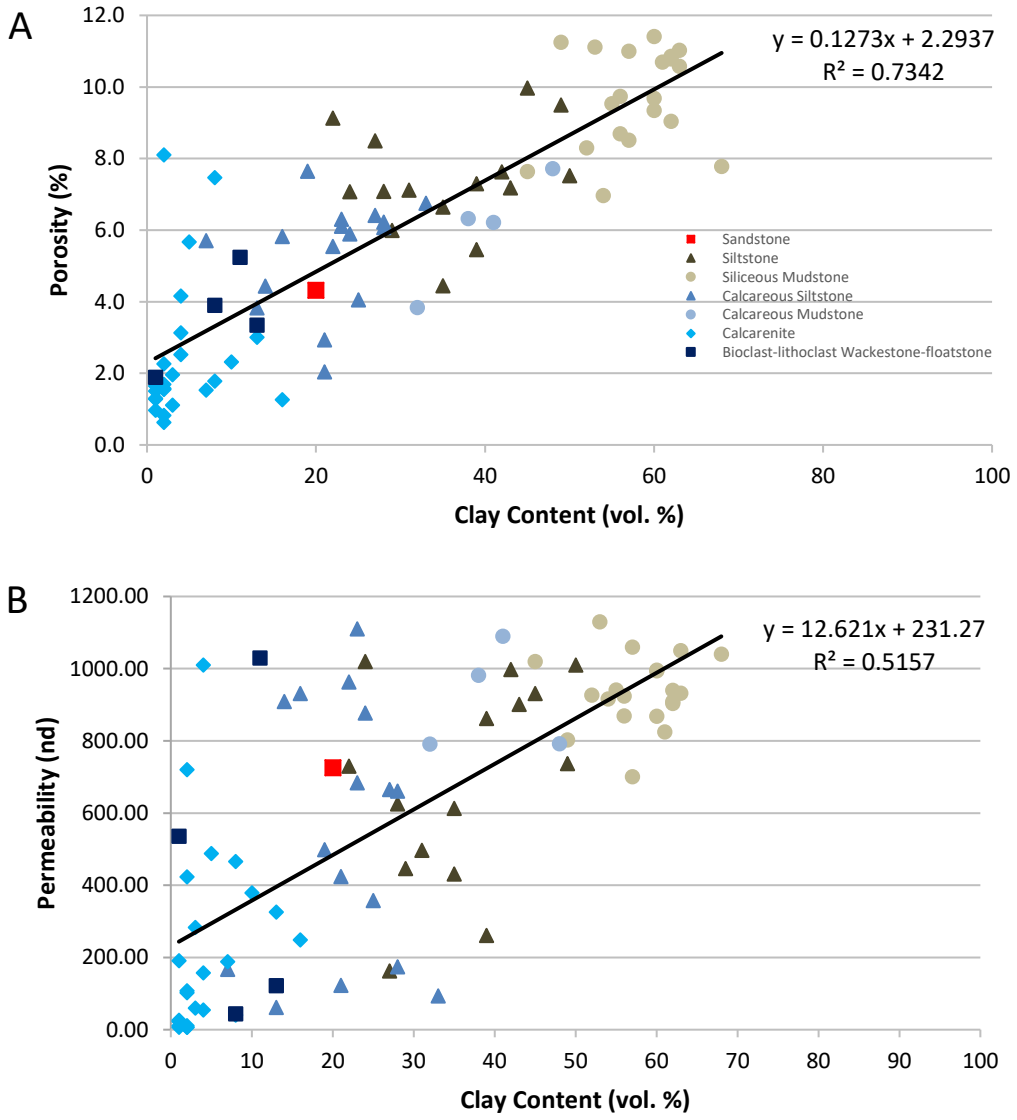

Figure 43: Cross-plots of clay content versus porosity (A) and permeability (B) versus clay content. Clay is positively correlated to enhanced reservoir quality.

CHAPTER 7: INORGANIC GEOCHEMISTRY

In this study, XRF was used to determine the elemental composition of 36 samples from the Strain 2V core. For this study, fourteen elements were addressed based on their uses in characterizing sedimentary deposits as reported in published literature (Wedepohl, 1971; Brumsack, 1989; Sageman and Lyons, 2003; Tribovillard et al., 2006): silicon (Si), aluminum (Al), potassium (K), titanium (Ti), zirconium (Zr), calcium (Ca), magnesium (Mg), strontium (Sr), molybdenum (Mo), vanadium (V), uranium (U), nickel (Ni), copper (Cu), and zinc (Zn). These elements can be separated into four distinct groupings of elements: 1) detrital elements (Si, Al, K, Ti, and Zr), 2) carbonate elements (Ca, Mg, and Sr), 3) redox-sensitive trace elements (Mo, V, and U), and 4) paleo-productivity proxies (Ni, Cu, and Zn).

7.1 Detrital Elements

Detrital elements are classified based on their common usage in geochemical studies as indicators of terrigenous influx in a system. These sediments are predominantly silicate mineral phases (e.g. quartz, feldspars, clays) which contain silicon (Brumsack, 1989). Si can also be associated with biogenic silica (e.g. radiolaria, sponge spicules; Brumsack, 1989; Sageman and Lyons, 2003). Due to this diversity of phases, Si is useful when reported as two distinct ratios; a silicon to aluminum ratio (Si/Al) to normalize Si to clay minerals and feldspars, and a silicon to titanium ratio (Si/Ti) which separates biogenic silica from detrital silica. Aluminum and potassium are reliable detrital proxies in sedimentary deposits (Brumsack, 1989; Sageman and Lyons, 2003). Al and K are typically held in clay mineral phases as well as in feldspars. Titanium and zirconium are strongly associated with terrestrially-derived sediments and have relatively low abundances in seawater. Additionally, both elements have very high diagenetic stabilities under most environmental conditions (Brumsack, 1989; Sageman and Lyons, 2003).

Observations of detrital proxy concentrations in the identified lithofacies have determined that non-calcareous lithofacies are significantly enriched in Si, Al, K, Ti, and Zr compared to calcareous lithofacies (Fig. 44). Conversely, ratios of Si to Al and Ti demonstrate high values in calcareous siltstones and calcarenites and low values for non-calcareous lithofacies and bioclast-lithoclast wackestones-floatstones. This suggests that silica in non-calcareous lithofacies and bioclast-lithoclast wackestones-floatstones is present as detrital quartz, whereas calcareous siltstones and calcarenites contain higher concentrations of biogenic silica.

Cross-plots of Si, Ti, K, and Zr versus Al exhibit strong linear trends and positive slopes, which suggests that these elements are strongly associated with detrital sediments and/or clay mineral phases (Fig. 45). The cross-plot of K versus Ti demonstrates a strong positive association with the detrital fraction. Cross-plots of Si versus Al and Ti, while exhibiting linear trends, do suggest an excess of silica, as evidenced by the data points near the upper left of the graphs. This excess silica likely reflects biogenic silica within the system. Additionally, general trends related to lithofacies are observe in these cross-plots. Calcareous lithofacies typically plot near the lower left of the graphs and non-calcareous lithofacies plot towards the upper right of the graphs. These trends reflect the low concentrations of detrital sediment in calcareous lithofacies relative to the non-calcareous lithofacies.

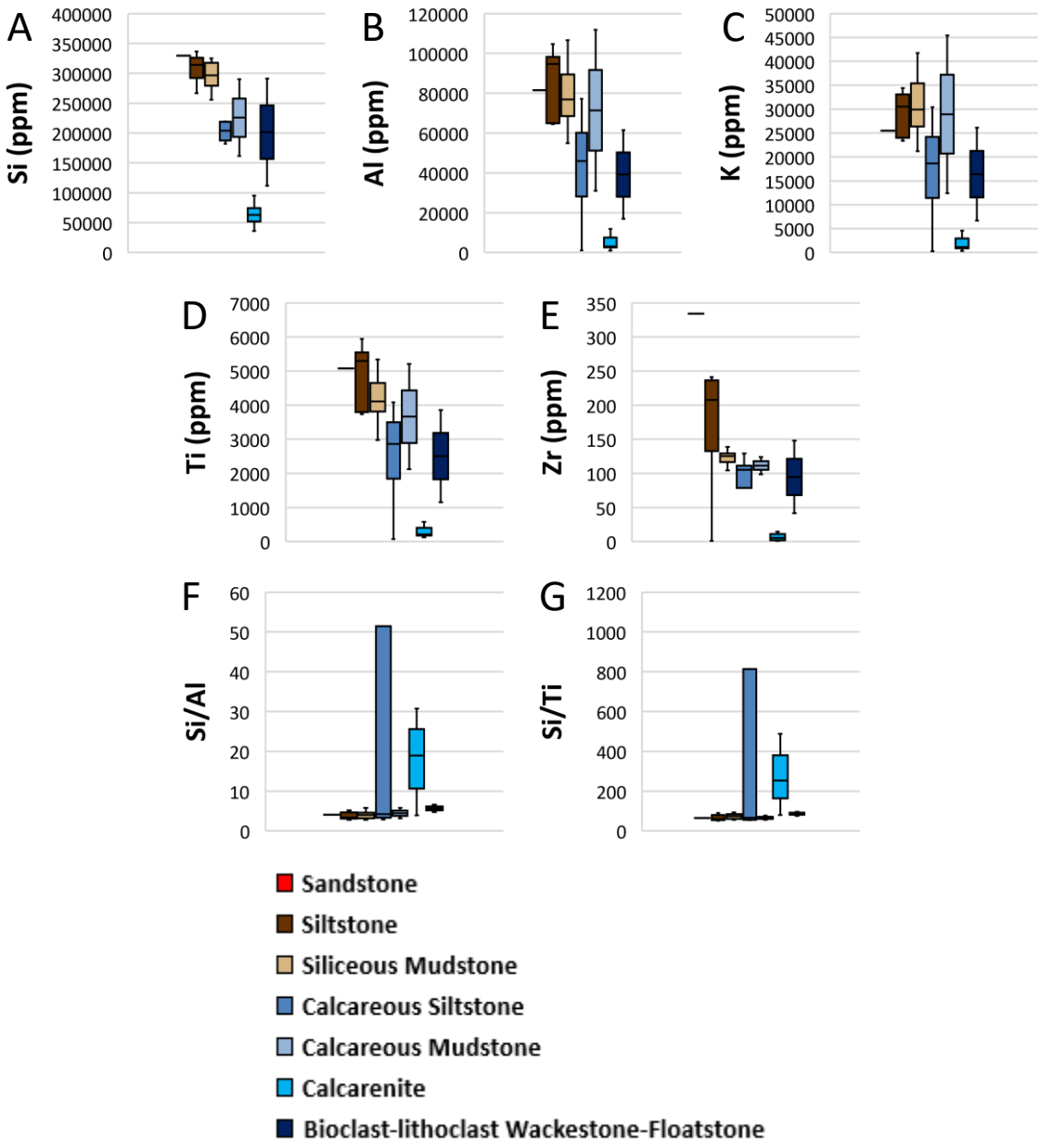

Figure 44: Box plots of detrital elements Si (A), Al (B), K (C), Ti (D), and Zr (E) as well as Si versus Al (F) and Ti (G) by lithofacies. Most detrital elements are significantly enriched in the non-calcareous lithofacies.

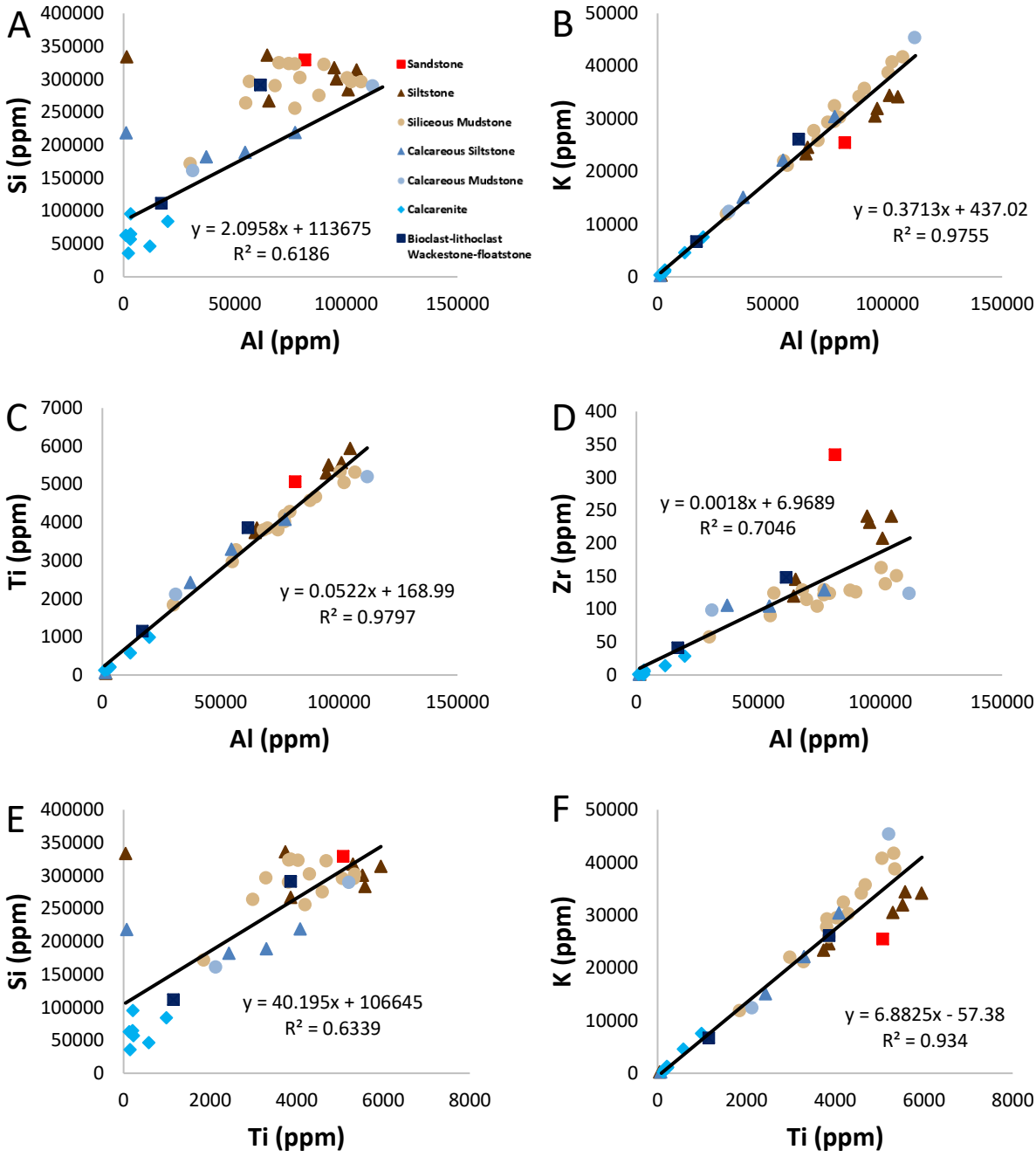

Figure 45: Cross-plots of Si (A), K (B), Ti (C), and Zr (D) versus Al as well as Si (E) and K (F) versus Ti differentiated by lithofacies.

7.2 Carbonate Elements

Carbonate elements are elements used to indicate the present of carbonate within a system. These elements include calcium, magnesium and strontium, which are all strongly associated with carbonates minerals (e.g. calcite, dolomite). However, it is important to note that these elements are capable of being held in feldspar, sulphate, and phosphate phases (Wedepohl, 1971; Brumsack, 1989).

Generally, concentrations of calcium are more enriched in calcareous lithofacies than in the non-calcareous lithofacies (Fig. 46). However, both Mg and Sr demonstrate generally similar concentrations regardless of lithofacies. This likely reflects the significance of dolomite phases in the Strain lithofacies. These observations can be supported by petrographic analyses and XRD analyses where ferroan dolomite can be observed throughout several lithofacies (see Chapter 5).

The cross-plot of Mg versus Ca demonstrates an overall negative linear trend. However, two distinct trends can be observed in relation to lithofacies. The first trend is a positive linear trend with non-calcareous lithofacies suggesting the presence of dolomite phases in those lithofacies. The second trend is a negative linear trend in calcareous lithofacies, suggesting the limited association of dolomite in lithofacies with high calcite concentrations. The cross-plot of Sr versus Ca exhibits a flat linear trend, suggesting that strontium is not associated with carbonate phases. Cross-plots of Al and Si both show a negative linear relationship with Ca. However, a trend in lithofacies can be observed in both plots, with non-calcareous lithofacies plotting in the upper left of the graphs and calcareous lithofacies plotting in the lower right of the graphs (Fig. 47).

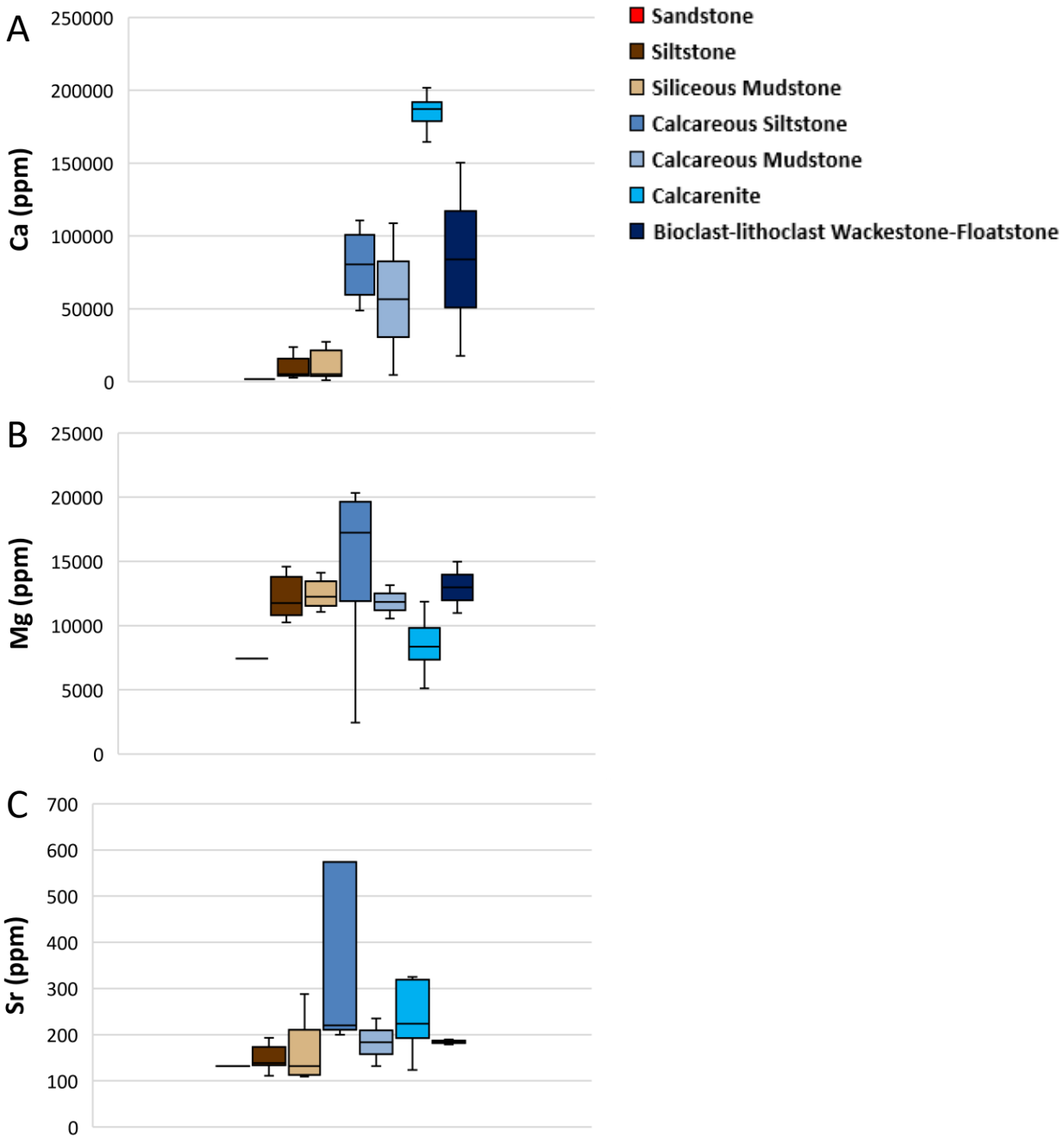

Figure 46: Box plots of carbonate elements Ca (A), Mg (B), and Sr (C) by lithofacies. Most carbonate elements exhibit strong enrichment in calcareous lithofacies.

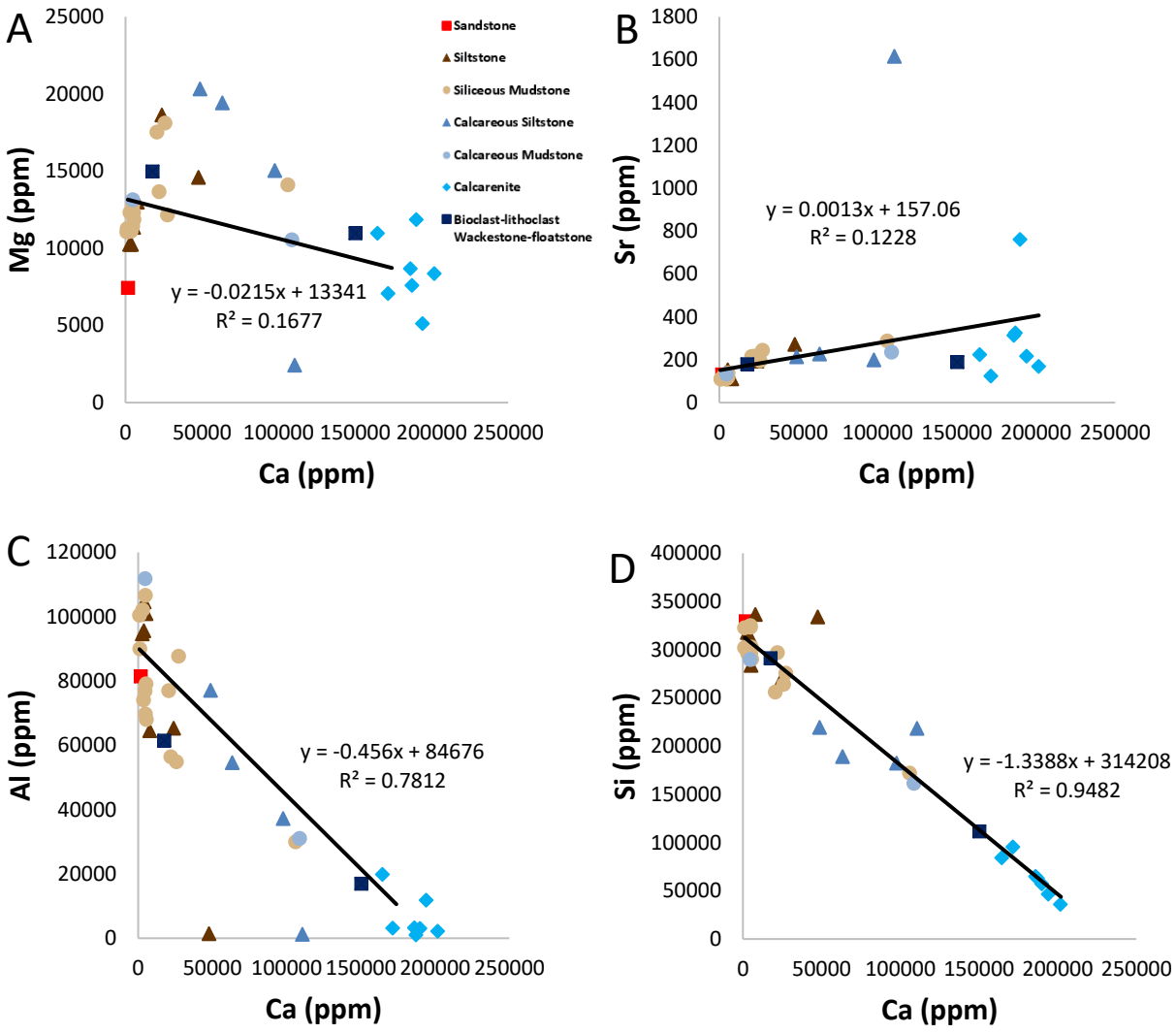

Figure 47: Cross-plots of Mg (A), Sr (B), Al (C), and Si (D) versus Ca differentiated by lithofacies.

7.3 Redox-sensitive Trace Elements

Redox-sensitive trace elements (RSTEs) are commonly used to assess the redox conditions of marine settings both ancient and recent. Specifically, these elements can indicate whether paleo-redox conditions were oxidizing or reducing. In oxic conditions, dissolved O_2 is present in waters overlying and underlying the sediment-water interface. As the supply of available oxygen decreases, oxygen-stressed (anoxic) conditions become increasingly prevalent. These anoxic conditions can be nonsulfidic or sulfidic, the latter of which is termed euxinic and is characterized by free H_2S present in the water column. Mo is highly abundant in oxic waters as the molybdate (MoO_4^{2-}) anion. However, under oxygen-depleted conditions it is highly reactive, leading to enrichments of Mo in organic-rich black shales. Mo is strongly associated with organic matter and sulfides phases, indicating its utility as an indicator of euxinia. Vanadium has a redox chemistry similar to Mo, however, unlike Mo, V is not associated with sulfides, suggesting it is a useful indicator of anoxia but not euxinic conditions. U is known for having a constant concentration in sea water and a strong affinity for organic matter. However, U is highly sensitive to remobilization by oxygen penetration which can result in erroneous U concentrations (Tribovillard et al., 2006).

In this study, concentrations of RSTEs are not strongly related to lithofacies. Siliceous and argillaceous facies are concentrated in RSTE. Conversely, a notable depletion of RSTEs is observed in the calcarenite lithofacies, suggesting a strongly negative association with carbonate content (Fig. 48). These observations suggest anoxia was prevalent during the deposition of siliciclastic facies whereas redox conditions were less reducing in carbonates, resulting in less TOC in carbonate facies.

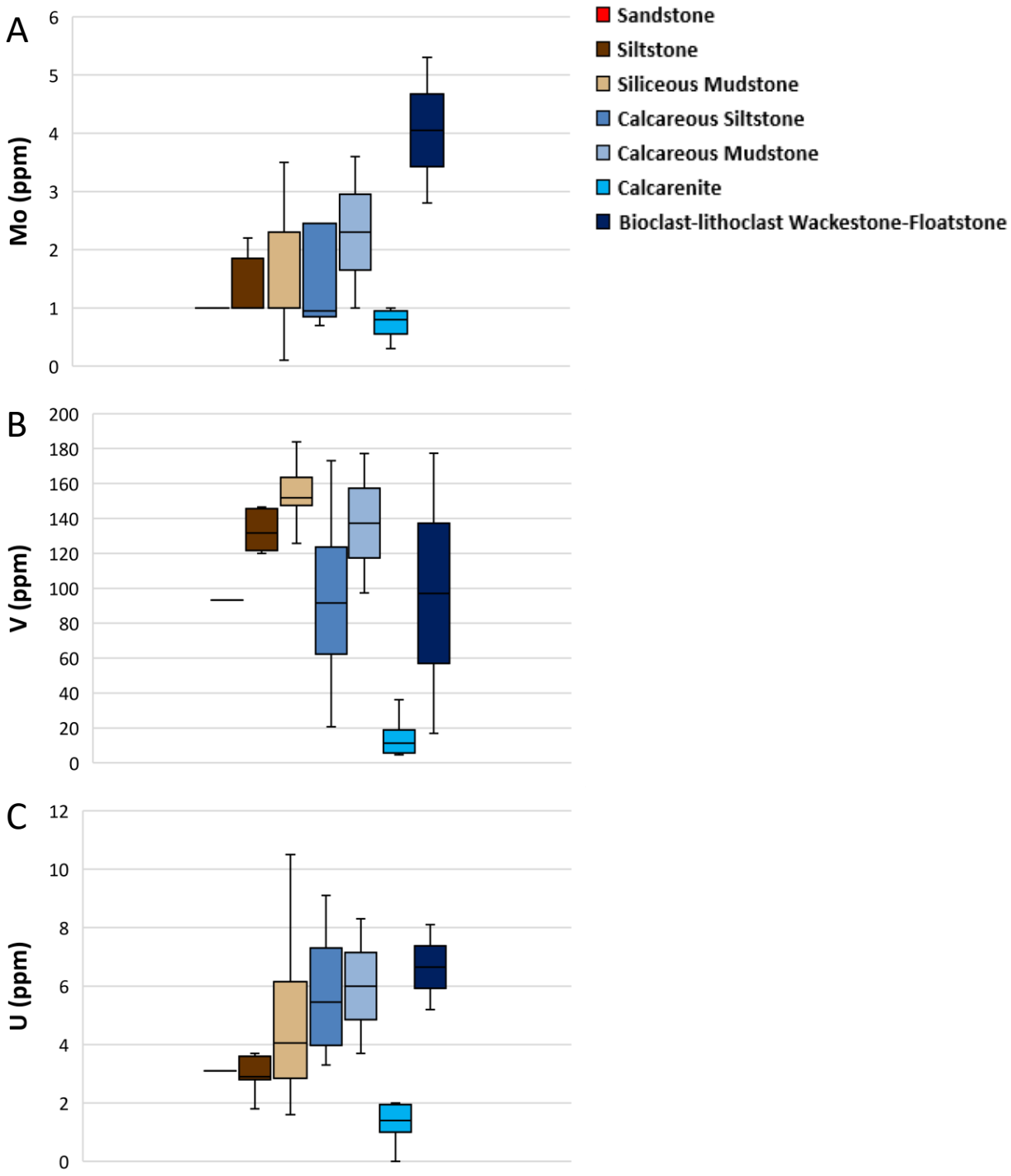

Figure 48: Box plots of redox-sensitive trace elements Mo (A), V (B), and U (C) by lithofacies. Concentrations of RSTEs are generally unrelated to lithofacies.

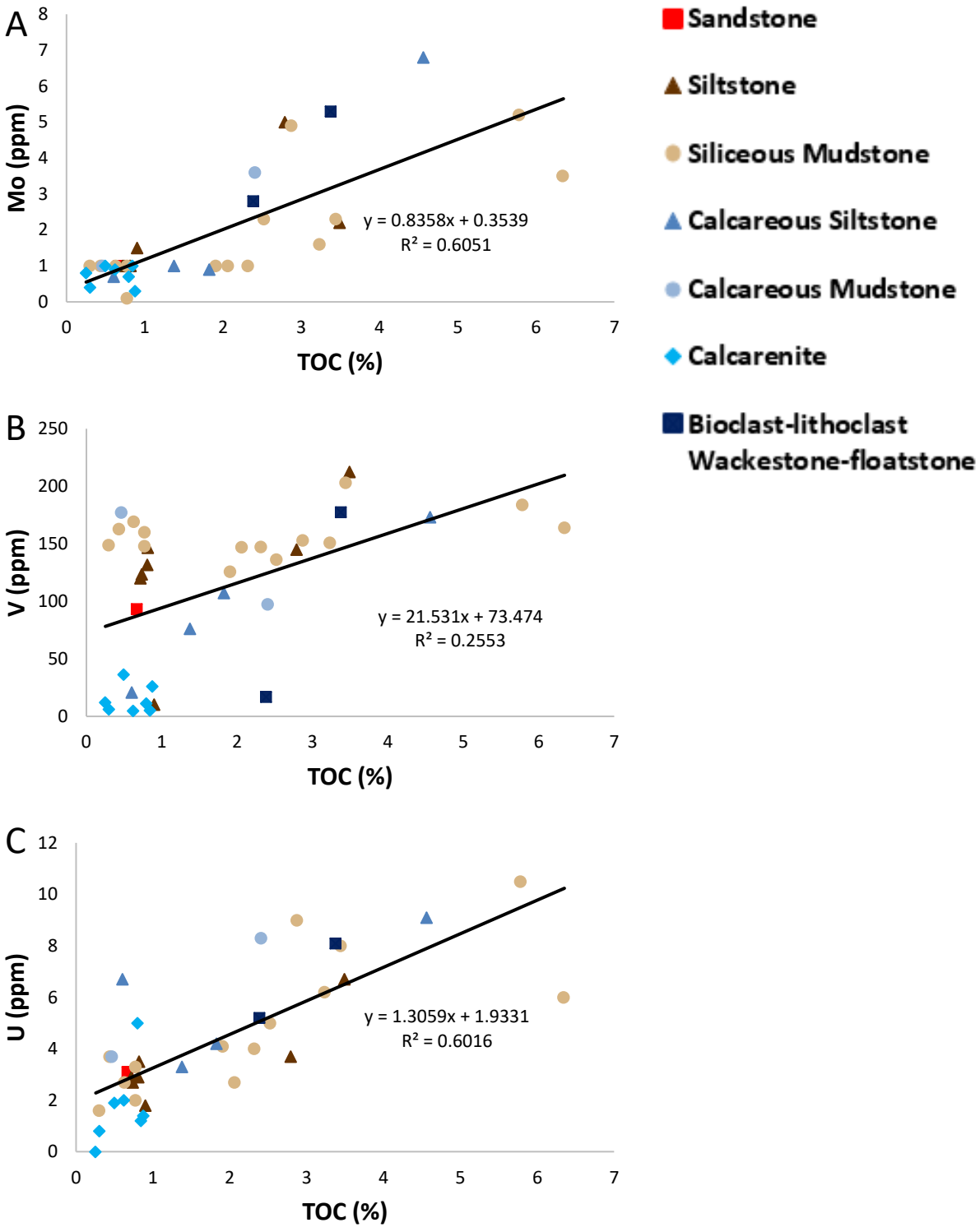

Figure 49: Cross-plots of RSTEs Mo (A), V (B), U (C) versus TOC with samples differentiated by lithofacies. Mo, V, and U all show generally positive linear covariance with TOC. V and U are both significantly enriched in non-calcareous lithofacies.

Cross-plots of RSTEs versus TOC show a strong positive covariance between Mo and TOC and weak positive relationships between V and U and TOC. As discussed above, clay-rich lithofacies are notably enriched in RSTEs and carbonate- and silica-rich facies are depleted (Fig. 49).

7.4 Paleo-productivity Proxies

Paleo-productivity proxies are elements that typically behave as micronutrients in oxic marine conditions and are strongly associated with organic matter and pyrite phases. Ni is present commonly as soluble Ni^{2+} cations, $NiCl^{+}$ ions, or $NiCO_3$ under oxic conditions. Under anoxic/euxinic conditions, Ni is incorporated in OM as tetrapyrrole complexes. Cu, in oxic conditions, is present mainly as organometallic ligands or $CuCl^{+}$ ions to a lesser degree. Under reducing conditions, Cu may be incorporated as a solid solution phase in pyrite or other sulfide phases. Zn behaves as a micronutrient and under oxic conditions, is present as Zn^{2+} cations, $ZnCl^{+}$ ions, or complexes in humic/fulvic acids. Under reducing conditions, Zn may be incorporated as ZnS as a solid solution phase in pyrite or form its own sulfide phases (Tirbovillard et al., 2006).

Observations of paleo-productivity proxy concentrations show that increased concentrations of Ni and Cu are related to non-calcareous lithofacies and increased concentrations of Zn are related to calcareous lithofacies, except in the calcarenite samples (Fig. 50). These observations suggest that Zn is not present in organic matter but rather pyrite or other mineral phases.

Cross-plots of Ni, Cu, and Zn versus organic matter exhibit positive linear trends. Ni and Cu show the strongest trends when plotted against TOC. On the other hand, Zn shows limited association with organic richness below 3% TOC. In facies with greater than 3% TOC, increased

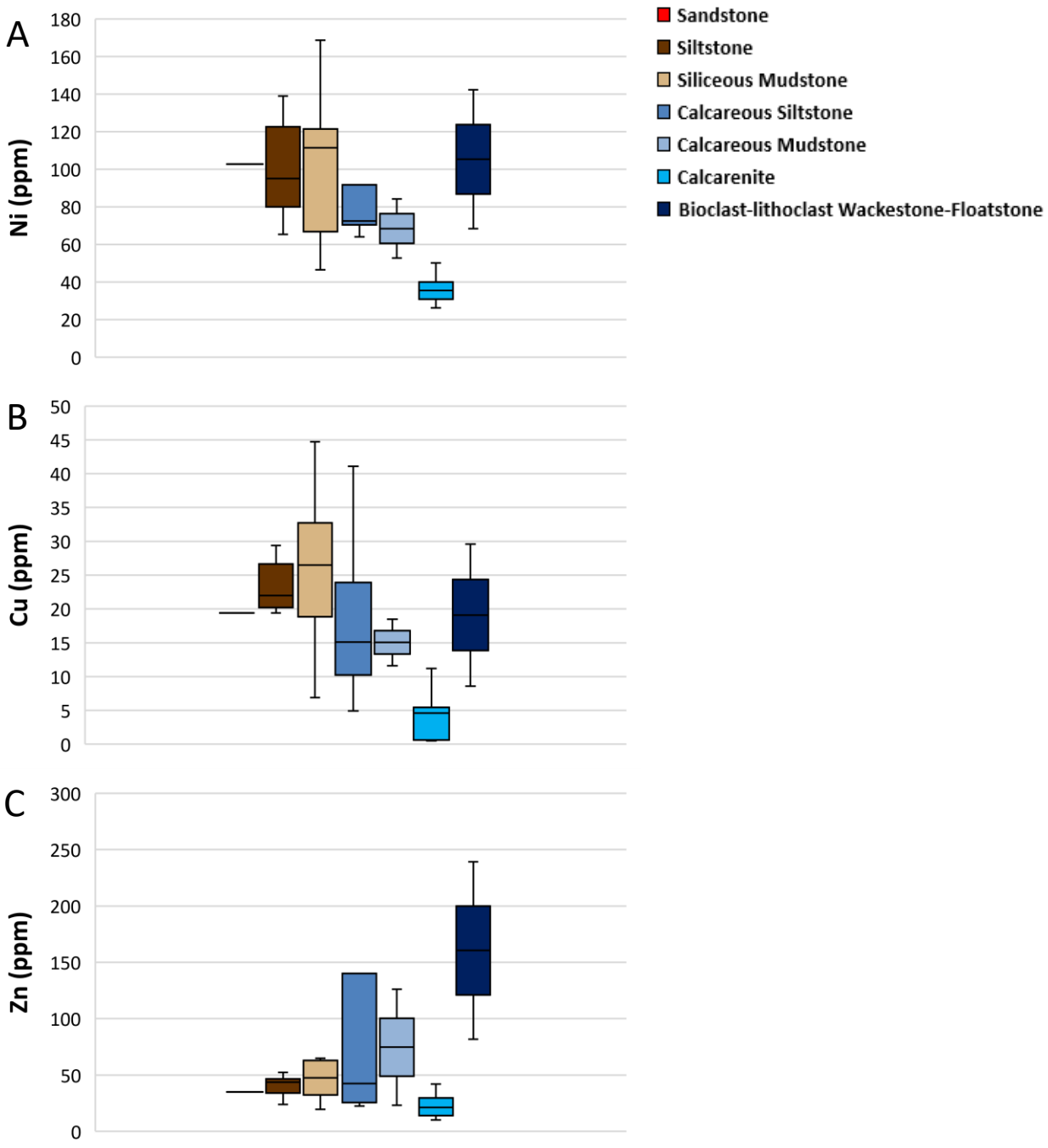

Figure 50: Box plots of paleo-productivity proxies Ni (A), Cu (B), and Zn (C) by lithofacies. Concentrations of paleo-productivity proxies vary with lithofacies. Ni and Cu exhibit higher concentrations in non-calcareous lithofaces while Zn is more strongly enriched in calcareous lithofacies.

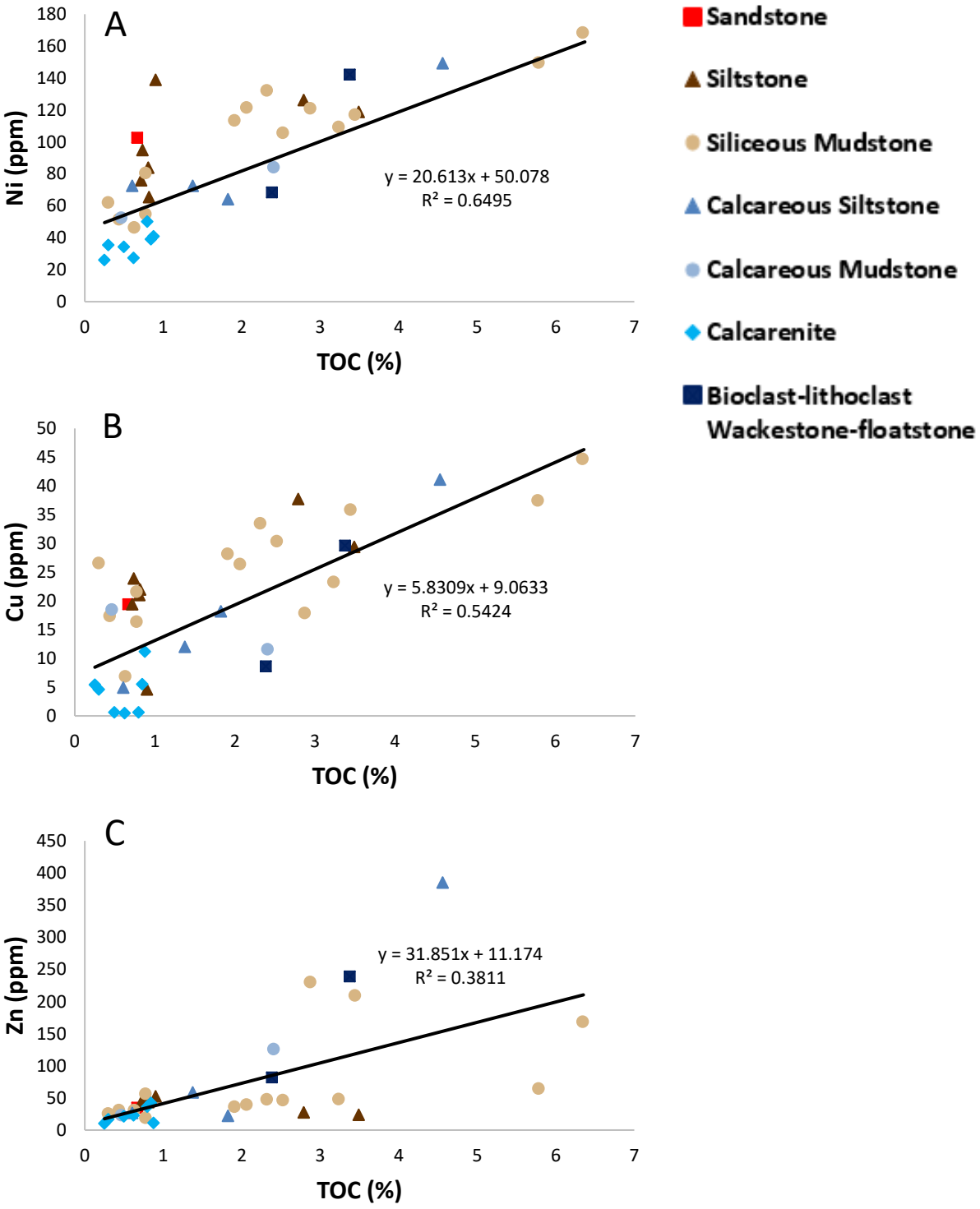

Figure 51: Cross-plots of paleo-productivity proxies Ni (A), Cu (B), and Zn (C) versus TOC with samples differentiated by lithofacies. Linear relationships are observed with most proxies, although, Zn displays little covariance with TOC below 3% TOC.

concentrations of Zn are observed. Of the identified lithofacies, siliceous mudstones exhibit the highest concentrations of paleo-productivity proxies and TOC (Fig. 51).

7.5 Elemental Variations with Depth

This study qualitatively describes elemental variation throughout the Strain core by plotting the vertical profiles of the 14 elemental proxies, TOC, and core gamma in an attempt to develop a chemostratigraphic framework for the Strain core deposits (Fig. 52).

The profiles of detrital elements are generally in phase with one another. The only notable exception is at 5465', silicon has a marked increase while Al, K, Ti, and Zr all decrease sharply. Towards the top of the core, detrital elements are significantly less abundant relative to the lower part of the core.

Carbonate element profiles exhibit more varied behavior between the different carbonate proxies. Ca is typically constant throughout the core with significant spikes associated with sharp decreases in the abundances of detrital proxies. On the other hand, Mg is in phase with detrital proxies, exhibiting higher concentrations in intervals enriched with detrital elements and lower concentrations in intervals enriched in Ca. Sr exhibits consistently low concentrations throughout the core except in the zone of Si enrichment at 5464'. Here, Sr increases substantially before returning to background concentrations.

RSTEs are in phase with detrital elements. However, the covariance between detrital proxies and Mo is weaker in the lower part of the Strain core. Profiles of both V and U show strong covariance in relation to detrital elements.

Paleo-productivity proxies, similar to the RSTEs, are in phase with detrital elements, although Zn is generally in lower concentrations throughout the Strain core.

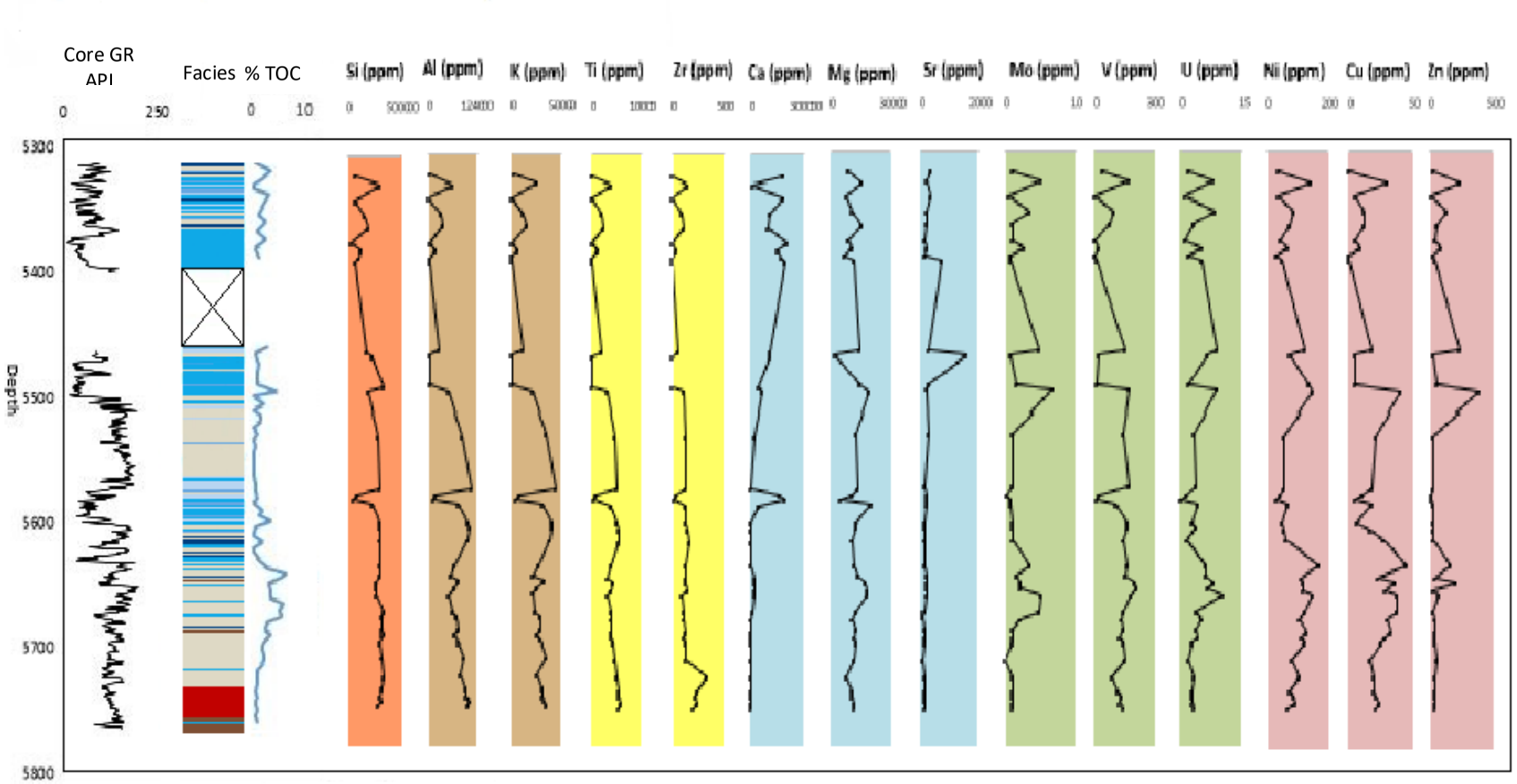

Figure 52: Core gamma, facies log, TOC, and elemental profiles for the fourteen elements observed in this study.

7.6 Chemostratigraphic Sea-Level Implications

By utilizing the vertical geochemical variation presented in Figure 52 and the sea-level interpretations discussed in Chapter 5, paleo-redox state of the Midland Basin during the Permian can be related to sea-level change. Geochemical proxies for detrital influx are enriched in the lowstand deposit LA-A while RSTEs, paleo-productivity proxies, and TOC are depleted. This suggests that LA-A was deposited under oxygenated waters resulting in reduced accumulation of organic matter, RSTEs, and paleo-productivity proxies (Algeo and Tribovillard, 2009). In contrast, TOC, paleo-productivity proxies, and RSTEs increase in overlying lithofacies associations, reaching their maxima in LA-C. These trends suggest that during marine transgression and highstand, an oxygen minimum zone had been established in the Midland Basin due to increased productivity. As sea-level in the basin transgressed, the oxygen minimum zone transgressed landward, resulting in an anoxic environment under which LA-B and LA-C were deposited. In the late highstand and lowstand deposits of LA-D and LA-E, respectively, TOC, paleo-productivity proxies, and redox proxies generally decrease and remain relatively depleted until the uppermost LA-E. These trends suggest that, with marine regression, the oxygen minimum zone regressed below the site of deposition for the Strain core. LA-F and LA-G exhibit higher-frequency oscillations in TOC, paleo-productivity, and RSTEs. These trends suggest that the later transgression and highstand of LA-F and LA-G, again, established an oxygen minimum zone that transgressed landward. However, the oscillatory nature of the geochemical trends implies that during a longer-term transgression-regression cycle, there were shorter-term sea-level changes occurring in the Midland Basin (Haq and Schutter, 2008).

CHAPTER 8: CONCLUSIONS

The understanding of depositional environments and processes in deep marine, carbonate-dominated settings is lacking compared to siliciclastic settings. The current study focused on a 400-ft-thick drill core section of the Wolfcamp Formation in Mitchell County, Texas, with particular emphasis on the Lower Permian section (operational benches Wolfcamp A and B) of the core. The core sourced from wildcat well Strain 2V (API 42-335-53586) was made available along with thin sections, mineralogical, and petrophysical data by Devon Energy. Lithologic, petrologic, and geochemical analyses were performed in order to (1) characterize the lithofacies in the Wolfcamp Formation, (2) interpret the environments and depositional conditions and processes that influenced deposition of the Wolfcamp Formation, and (3) assess the hydrocarbon-source rock and hydrocarbon-reservoir rock potential of the Wolfcamp Formation lithofacies. The principle findings of this study are summarized below.

(1) Seven lithofacies are recognized in the Strain 2V core interval of the Wolfcamp Formation: sandstones; siltstones; siliceous mudstones; calcareous siltstones; calcareous mudstones; calcarenites; bioclast-lithoclast wackestone-floatstones.

(2) A variety of depositional processes were responsible for the deposition of the Wolfcamp Formation. Turbidity currents and debris flows dominate the Strain core. Thick-bedded and thin-bedded calcarenite beds are attributed to proximal and distal turbidity currents, respectively. Debris flows are represented by bioclast-lithoclast floatstones. Coarsening-fining upward hyperpycnites are also observed in the Strain core. Mudstones were likely deposited by pelagic and hemipelagic processes under anoxic conditions. The vertical distribution of lithofacies reflects changes of siliciclastics and carbonates due to sea-level fluctuations influenced by the

Late Paleozoic Ice Age. Thin, calcareous HEBs are also observed in the upper portions of the Strain core.

(3) Lithofacies were grouped into distinct stratigraphic associations. These lithofacies associations, in ascending order, are: 1) interbedded sandstone and siltstone lithofacies association (LA-A), 2) mudstone with calcarenite, and bioclast-lithoclast wackestone-floatstone lithofacies association (LA-B), 3) calcarenites, bioclast-lithoclast wackestones-floatstone, and mudstone lithofacies association (LA-C), 4) calcarenite and calcareous siltstone with interbedded calcareous mudstone lithofacies association (LA-D), 5) siliceous mudstone lithofacies association (LA-E), 6) massive calcarenite and rare mudstone lithofacies association (LA-F), and 7) mudstone, thin calcarenite and bioclast-lithoclast wackestones-floatstone lithofacies association (LA-G). These lithofacies associations are related to sea-level cycles. LA-A represents a sea-level lowstand. LAs B, C, and D correspond to transgressive and highstand sea-level conditions. LA-E, representing the Wolfcamp Shale Marker unconformity, was deposited during lowstand conditions. LAs F and G correspond to sea-level transgressions and highstands, respectively.

(4) Organic matter contents of the Wolfcamp Formation are sufficient for this unit to serve as a hydrocarbon-source rock. Kerogen within the Wolfcamp Formation is a mix of Type II and Type III, indicating marine and terrestrial contributions of organic material. The contribution from terrestrial sources is supported by the presence of relatively well-preserved plant fossils along the bedding planes of mudrocks in the Strain core. Rock-eval pyrolysis indicates that the Wolfcamp Formation is a mature source rock, with few samples displaying immature and overmature values. Mineralogy versus TOC cross-plots demonstrate a positive correlation between TOC and

siliceous and argillaceous facies making these facies the highest quality hydrocarbon-source rocks. Carbonate facies are negatively associated with TOC.

(5) Petrophysical and mineralogical data suggests that clay-rich and quartz-rich facies in the Strain core are the best unconventional hydrocarbon-reservoir rocks. Carbonate facies are generally poor unconventional hydrocarbon-reservoirs due to carbonate cementation.

(6) Geochemical analyses of the Wolfcamp Formation lithofacies were performed using 14 geochemical proxies for detrital sediment, carbonate detritus, redox-sensitive trace metals, and paleo-productivity proxies. Detrital proxies are typically associated with non-calcareous lithofacies, along with magnesium, redox proxies, and paleo-productivity indicators, suggestion deposition of lithofacies under anoxic conditions. Calcareous facies are typically only enriched in biogenic silica proxies (i.e. Si/Al, Si/Ti) and calcium. The depletion of RSTEs in calcareous facies suggests deposition under less reducing conditions, resulting in reduced TOC and source-rock potential.

References

Adams, J. A. S., and Weaver, C. E., 1958, Thorium-to-uranium ratios as indicators of sedimentary processes: example of concept of geochemical facies: American Association of Petroleum Geologists Bulletin: vol. 42, p. 387-430.

Algeo, T. J., and Tribovillard, N., 2009, Environmental analysis of paleoceanographic systems based on molybdenum-uranium covariation: Chemical Geology, vol. 268, p. 211-225.

Bagnold, R. A., 1954, Experiments on a gravity-free dispersion of large solid spheres in a Newtonian fluid under shear. in proceedings, Royal Society of London A: Mathematical, Physical and Engineering Sciences, vol. 225, no. 1160, p. 49-63.

Baumgardner, R. W., DiMichele, W. A. and de Siqueira Vieira, N., 2016, An early Permian coastal flora dominated by Germaropteris martinsii from basinal sediments in the Midland Basin, West Texas: Palaeogeography, Palaeoclimatology, Palaeoecology, vol. 459, p. 409-422.

Baumgardner, R. W., and Hamlin H. S., 2014, Core-based Geochemical Study of Mudrocks in Basinal Lithofacies in the Wolfberry Play, Midland Basin, Texas, Part II, Search and Discovery Article #105572.

Berner, R. A., and Raiswell, R., 1983, Burial of organic carbon and pyrite sulfur in sediments over Phanerozoic time: A new theory: Geochimica et Cosmochimica Acta, vol. 47, p. 855-862.

Blakey, R., 2011, Global Paleogeography: Web accessed 10 August 2017.

Bostwick, D. A., 1962, Fusulinid stratigraphy of beds near the Gaptank-Wolfcamp boundary, Glass Mountains, Texas: Journal of Paleontology, vol. 36, no. 6, p. 1189-1200.

Bouma, A. H., Kuenen, P. H. and Shepard, F. P., 1962, Sedimentology of some Flysch deposits: A graphic approach to facies interpretation: Elsevier. p. 168.

Brumsack, H. J., 1989, Geochemistry of recent TOC-rich sediments from the Gulf of California and the Black Sea: International Journal of Earth Sciences, vol. 78, p. 851-882.

Cortez, M., III, 2012, Chemostratigraphy, paleoceanography, and sequence stratigraphy of the Pennsylvanian-Permian section in the Midland Basin of West Texas, with focus on the Wolfcamp Formation [Master's Thesis]: Austin, University of Texas at Austin, 121 p.

Crusius, J., Calvert, S. E., Pedersen, T., Sage, D., 1996, Rhenium and molybdenum enrichments in sediments as indicators of oxic, suboxic, and sulfidic conditions of deposition: Earth and Planetary Science Letters, vol. 145, p. 65-78.

David, Z. P., 1994, Seawater as the source of minor elements in black shales, phosphorites, and other sedimentary rocks: Chemical Geology, vol. 114, p. 95-114.

Dembicki, H., Jr., 2009, Three common source rock evaluation errors made by geologists during prospect or play appraisals: American Association of Petroleum Geologists Bulletin, vol. 93, no. 3, p. 341-356.

Dunham, R. J., 1962, Classification of carbonate rocks according to depositional texture: American Association of Petroleum Geologists Memoir, vol. 1, p. 108-121.

Engle, M. A., Reyes, F.R., Varonka, M.S., Orem, W.H., Ma, L., Ianno, A.J., Schell, T.M., Xu, P. and Carroll, K.C., 2016, Geochemistry of formation waters from the Wolfcamp and "Cline" shales: Insights into brine origin, reservoir connectivity, and fluid flow in the Permian Basin, USA: Chemical Geology, vol. 425, p.76-92.

Fielding, C. R., Frank, T.D., and Isbell, J.L., 2008. The late Paleozoic ice age—A review of current understanding and synthesis of global climate patterns: Resolving the Late Paleozoic Ice Age in Time and Space: Geological Society of America, Special Papers, vol. 441, p. 343-354.

Fischer, A. G., and Samthein, M., 1988, Airborne silts and dune-derived sands in the Permian of the Delaware Basin: Journal of Sedimentary Research, vol. 58, no. 4.

Flamm, D. S., 2008, Wolfcampian Development of the Nose of the Eastern Shelf of the Midland Basin, Glasscock, Sterling, and Reagan Counties, Texas [Master's Thesis]: Provo, Brigham Young University. 54 p.

Frenzel, H. N., et al., 1988, The Permian basin region, in L. L. Sloss, ed., Sedimentary cover—North American craton; U.S.: Boulder, Colorado, Geological Society of America, The Geology of North America, vol. D-2, p. 261–306.

Gastaldo, R. A., DiMichele, W. A., and Pfefferkorn, H.W., 1994, Out of the Icehouse into the Greenhouse: A Late Paleozoic Analogue for Modern Global Vegetational Change: GSA Today, vol. 10, p. 1-7.

Gaswirth, S. B., Marra, K. R., Lillis, P. G., Mercier, T. J., Leathers-Miller, H. M.,Schenk, C. J., Klett, T. R., Le, P. A., Tennyson, M. E., Hawkins, S. J., Brownfield, M. E., Pitman, J. K., and Finn, T. M., 2016, Assessment of undiscovered continuous oil resources in the Wolfcamp shale of the Midland Basin, Permian Basin Province, Texas, 2016: U.S. Geological Survey Fact Sheet 2016–3092, 4 p., DOI:10.3133/fs20163092.

Hamlin, H. S., and Baumgardner R. W., 2012, Wolfberry (Wolfcampian-Leonardian) deep-water depositional systems in the Midland Basin: stratigraphy, lithofacies, reservoirs, and source rocks: The University of Texas at Austin, Bureau of Economic Geology Report of Investigations, no. 277, p. 62.

Haq, B. U., and Schutter, S. R., 2008, A chronology of Paleozoic sea-level changes: Science, vol. 322, p. 64-68.

Haughton, P. D. W., Davis, C., McCaffrey, W. and Barker, S., 2009, Hybrid sediment gravity flow deposits–classification, origin and significance: Marine and Petroleum Geology, vol. 26, no. 10, p. 1900-1918.

Hills, J. M., 1985, Structural evolution of the Permian Basin of West Texas and New Mexico. In: Dickerson, P. W., Muehlberger, W. R., eds., Structure and Tectonics of Trans-Pecos Texas: West Texas Geological Society, pub. 85-81, p. 89-99.

Jones, B., and Manning, A. C., 1994, Comparisons of geochemical indices used for the interpretation of paleoredox conditions in ancient mudstones: Chemical Geology, v. 111, p. 111-129.

Kocurek, G., and Kirkland, B. L., 1998, Getting to the source: aeolian influx to the Permian Delaware basin region: Sedimentary Geology, vol. 117, no. 3, p. 143-149.

Kvale, E. P., Flenthrope, C. and Mace, C., 2017, Carbonate-Dominated Hybrid Sediment Gravity Flows Within the Upper Wolfcamp, Delaware Basin, USA: Vectors for Transmitting Terrestrial Organics Into a Deep Marine Basin, in Proceedings, American Association of Petroleum Geologist Annual Convention and Exhibition.

Lowe, D. R., 1982, Sediment gravity flows: II Depositional models with special reference to the deposits of high-density turbidity currents: Journal of Sedimentary Research, vol. 52, no.1.

Mackenzie, F. T., 2005, Sediments, Diagenesis, and Sedimentary Rocks: Elsevier Science.

Matchus, E. J. and Jones, T. S., 1984, East-west cross section through Permian Basin of West Texas: prepared by Stratigraphic Problems Committee of the West Texas Geological Society, 1 sheet.

Mazzullo, S. J., 1998, Lithology, depositional facies, and diagenesis of a Lower Leonardian periplatform limestone: Indian Wells# 17-4 Schlinke, Irion County, Texas: West Texas Geological Society Publications, p. 2-2.

McManus, J., Berelson, W. M., Severmann, S., Poulson, R. L., Hammond, D. E., Klinkhammer, G. P., Holm, C., 2006, Molybdenum and uranium geochemistry in continental margin sediments: Paleoproxy potential: Geochimica et Cosmochimica Acta, vol. 70, p. 4643-4662.

Miall, A. D., 2008, The southern midcontinent, Permian basin, and Ouachitas: Sedimentary Basins of the World, vol. 5, p. 297-327.

Middleton, G. V., and Hampton, M. A., 1973, Part I. Sediment gravity flows: mechanics of flow and deposition, p. 1-38.

Moore, C. H., and Wade, W. J., 2013, Carbonate reservoirs: porosity and diagenesis in a sequence stratigraphic framework, 2nd edition, Amsterdam, Netherlands: Elsevier, 1-392.

Morford, J. L., and Emerson, S., 1999, The geochemistry of redox sensitive trace metals in sediments: Geochima et Cosmochimica Acta , vol. 63, no. 11/12, p. 1735-1750.

Mulder, T., and Alexander, J., 2001, The physical character of subaqueous sedimentary density flows and their deposits. Sedimentology, vol 48, no. 2, p. 269-299.

Mutti, E. and Ricci Lucci, F., 1975, Turbidite facies and facies associations. In: Examples of turbidite facies and associations from selected formations of the northern Apennines. IX Int. Congress of Sedimentology, Field Trip A-11, p. 21-36.

Payros, A., and Pujalte, V., 2008, Calciclastic submarine fans: An integral overview: Earth-Science Reviews, vol. 86, p. 203-246.

Piper, D. Z., and Calvert, S. E., 2009, A marine biogeochemical perspective on black shale deposition: Earth-Science Review, vol. 95, p. 63-96.

Plink-Björklund, P., and Steel, R. J., 2004, Initiation of turbidity currents: outcrop evidence for Eocene hyperpycnal flow turbidites: Sedimentary Geology, vol. 165, p. 29–52.

Posamentier, H. W., and R. G. Walker, 2006, Deep-water turbidites and submarine fans: SEPM (Society of Sedimentary Geology) Special Publication, no. 84, p. 399–511.

Raiswell, R., and Berner, R. A., 1986, Prite and organic matter in Phanerozoic normal marine shales: Geochimica et Cosmochimica Acta, vol. 50, p. 1967-1976.

Rimmer, S. M., 2004, Geochemical paleoredox indicators in Devonian-Mississippian black shales, central Appalachian Basin, USA,: Chemical Geology, vol. 206, p. 373-391.

Rowe, H. D., Hughes, N., Robinson, K., 2012, The quantification and application of handheld energy-dispersive x-ray fluorescence (ED-XRF) in mudrock chemostratigraphy and geochemistry: Chemical Geology, vol. 324-325, p. 122-131.

Rowe, H. D., Loucks, R. G., Rupple, S. C., Rimmer, S. M., 2008, Mississippian Barnett Formation, Fort Worth Basin, Texas: Bulk geochemical inferences and Mo-TOC constraints on the severity of hydrographic restriction: Chemical Geology, vol. 257, p. 16-25.

Rowe, H. D., Rupple, S. C., Rimmer, S. M., Loucks, R. G., 2009, Core-based chemostratigraphy of the Barnett Shale, Permian Basin, Texas: Gulf Coast Association of Geological Societies Transactions, vol. 59, p. 675-686.

Sageman, B. B., and Lyons, T. W., 2003, Geochemistry of fine-grained sediments and sedimentary rocks, in: Mackenzie, F. T., ed., Sediments, Diagenesis, and Sedimentary Rock. Treatise on Geochemistry, vol. 7, p. 115-158.

Selley, R. C., and Sonnenberg, S. A., 2015, Elements of Petroleum Geology, 3rd ed., California: Academic Press. 536 p.

Silver, B. A., and Todd, R. G., 1969, Permian cyclic strata, northern Midland and Delaware Basins, West Texas and southeastern New Mexico: American Association of Petroleum Geologists Bulletin, vol. 53, p. 2223–2251.

Stow, D. A. and Mayall, M., 2000. Deep-water sedimentary systems: New models for the 21st century: Marine and Petroleum Geology, vol. 17, no. 2, p.125-135.

Stow, D. A. and Shanmugam, G., 1980, Sequence of structures in fine-grained turbidites: comparison of recent deep-sea and ancient flysch sediments: Sedimentary Geology, vol. 25 no.1-2, p.23-42.

Sutton, L., 2015, Permian Basin production-Midland vs Delaware Basins: http://info.drillinginfo.com/Permian-basin-production/ accessed May 2017.

Talling, P. J., Masson, D. G., Sumner, E. J., & Malgesini, G., 2012, Subaqueous sediment density flows: Depositional processes and deposit types: Sedimentology, vol. 59, no. 7, p. 1937-2003.

Tribovillard, N., Algeo, T., Lyons, T. W., and Riboulleau, A., 2006, Trace metals as paleoredox and paleoproductivity proxies: an update: Chemical Geology, vol. 232, no. 1-2, p. 12-32.

Udden, J. A., and Baker, C. L., Böse, E., 1916, Review of the geology of Texas: University of Texas Bulletin, vol. 44, 164 p.

Vidas, H., and Hughman, B., 2008, Availability, economics, and production potential of North American unconventional natural gas supplies: INGAA Foundation, Inc., p. 1-167.

Wahlman, G. P., and Tasker, D. R., 2013, Lower Permian (Wolfcampian) carbonate shelf-margin and slope facies, Central Basin Platform and Hueco Mountains, Permian Basin, West Texas, USA: SEPM (Society of Sedimentary Geology) Special Publication, no. 105, p. 305- 333.

Wedepohl, K. H., 1971, Environmental influences on the chemical composition of shales and clays, in: Ahrens, L. H., Press, F., Runcom, S. K., Urey, H. C., eds., physics and Chemistry of the Earth, vol. 8, Pergamon, Oxford, 1971, p. 305-333.

Wedepohl, K. H., 1991, The composition of the upper earth's crust and the natural cycles of selected metals, Metals in natural raw materials, Natural Resources, in Merian, E., ed., Metals and Ther Compounds in the Environment, VCH, Weinheim, p. 3-17.

Wignall, P. B., and Myers, K. J., 1988, Interpreting benthic oxygen levels in mudrocks: a new approach: Geology, vol. 16, p. 452.

Yang, k. and Dorobek, S. L., 1995, The Permian Basin of West Texas and New Mexico: tectonic history of a "composite" foreland basin and its effects on stratigraphic development, in Dorobek, S. L. and Ross, G. M., eds., Stratigraphic evolution of foreland basins: SEPM (society of Sedimentary Geology) Special Publication, no. 52, p. 149-174.